Detectability of Biosignature Gases in the Atmospheres of Terrestrial Exoplanets

by

Stephen Joseph Messenger

B.S. in Physics, University of Missouri (2010)

Submitted to the Department of Earth, Atmospheric, and Planetary Sciences
in partial fulfillment of the requirements for the degree of

Master of Science in Earth and Planetary Sciences

at the

MASSACHUSETTS INSTITUTE OF TECHNOLOGY

February 2013

Author .....
Department of Earth, Atmospheric, and Planetary Sciences
December 3, 2012

Certified by .....
Sara Seager
Class of 1941 Professor, Department of Earth, Atmospheric, and Planetary Sciences and Department of Physics
Thesis Supervisor

Accepted by .....
Robert D. van der Hilst
Schlumberger Professor of Earth Sciences
Head, Department of Earth, Atmospheric, and Planetary Sciences

Detectability of Biosignature Gases in the Atmospheres of Terrestrial Exoplanets

by

Stephen Joseph Messenger

Submitted to the Department of Earth, Atmospheric, and Planetary Sciences
on December 3, 2012, in partial fulfillment of the
requirements for the degree of
Master of Science in Earth and Planetary Sciences

Abstract

Biosignature gases in the atmosphere of an exoplanet provide a means by which we can deduce the possible existence of life on that planet. As the list of possible biosignature gases is ever growing, the need to determine which molecules provide the best opportunities for detection grows as well. One way to explore these systems is through modeling radiative transfer via transmissivity as light travels from the parent star, through the atmosphere of the planet, and then impacts a detector located at Earth. As the light travels through the planetary atmosphere, it acquires molecular features from the planet due to the composition, temperature, and pressure structure of the atmosphere. By adding synthetic noise to the modeled transmissivity spectra, I determine the detectability of a range of atmospheric mixing ratios for ten biosignature gases from the HIgh-resolution TRANsmission molecular absorption (HITRAN) database: oxygen, ozone, methane, nitrous oxide, methyl bromide, methyl chloride, hydrogen sulfide, carbonyl sulfide, phosphine, and sulfur dioxide. The deep investigation of the HITRAN biosignature gases in this study is possible due to the ability to properly map their absorption cross sections to varying temperatures and pressures. For each of the above HITRAN molecules, I analyze alternative spectral features for detection in order to emphasize the importance of and determine the ability for multiple band detection of biosignature gases. Water vapor (though not a biosignature gas) is included in order to study its potential for spectral masking. Though I find that each of the above HITRAN gases could be detected in exoplanet atmospheres if that molecule has a large enough atmospheric mixing ratio, an Earth-size planet with an Earth-like atmosphere located at 35.45 parsecs would only allow for discernible biosignature features from ozone, nitrous oxide, and methane in the infrared wavelength region.

Sixteen additional (and non-standard) biosignature gases included in this study do not have absorption cross sections that are currently mapable to alternative temperatures and pressures. These sixteen biosignature gases are acetaldehyde, acetone, benzene, carbon disulfide, dimethyl disulfide, dimethyl sulfide, dimethyl sulfoxide, ethanol, ethyl mercaptan, fluoroacetone, isoprene, methyl ethyl ketone, methyl

mercaptan, methyl vinyl ketone, thioglycol, and toluene. To circumvent the non-mapability of the absorption cross sections to different temperatures and pressures, I use the detectivity calculations and the absorption cross sections from ozone, methane, and nitrous oxide to estimate the threshold atmospheric mixing ratios for the detection of the sixteen non-standard biosignature gases with a 35 m telescope, 100 hours of observation, and a target distance of 35.45 parsecs. The combination of the threshold atmospheric mixing ratios calculated for these sixteen non-standard biosignature gases with the results from the HITRAN biosignature gases investigated in this study demonstrate that an atmospheric gas will require a mixing ratio in the tens to hundreds of ppm to be detectable above a 5σ level with a 35 m telescope, an observation time of 100 hours, and a target distance of 35.45 parsecs. Keeping with the theme of multi-wavelength detection, I end the analysis of the sixteen non-standard biosignature gases by proposing potential spectral feature wavelengths for each gas based on their molecular absorption cross section spectral profiles.

As many biosignature gases have molecular features at longer wavelengths than the traditional IR region, I investigated the technological requirements for detecting biosignature gas spectral features in one of the low-signal long-wavelength regions, the millimeter. Though the investigation into the millimeter region reveals unrealistic technological demands for the successful detection of the case study, oxygen, I use the analysis as a platform to introduce the theoretical concept of observing future targets with multiple next-generation telescopes stationed in a matrix in order to produce the same observational ability of a larger (and more distant future) telescope. While interferometric investigations into millimeter spectral features are improbable in the near future, the use of interferometry with next generation instruments may allow for investigations in the $10 - 30$ μm region, thereby opening alternative wavelengths for biosignature gas detection. Since this theoretical interferometry idea relies on the ability to increase the signal-to-noise ratio (SNR) of the observations, I investigated the interaction between telescope aperture size and observation duration on the detectability (i.e. SNR) of biosignature gases in reference to finding a middle ground between these two system parameters for both a 6 m and 35 m telescope. Unfortunately, a 6 m telescope does not provide a large enough collecting area to increase the SNR sufficiently enough to detect atmospheric gases. For futuristic telescope designs, though a 20 m telescope (or nine *JWST*s working together to achieve the same collecting area) would begin to discern some biosignature gas features from the continuum (for high biosignature gas atmospheric abundances), a 35 m class telescope (or equivalent interferometric telescope array) should be the minimum aperture size considered for biosignature gas detection in transmissivity spectroscopy.

Thesis Supervisor: Sara Seager
Title: Class of 1941 Professor, Department of Earth, Atmospheric, and Planetary Sciences and Department of Physics

Acknowledgments

I deeply appreciate and thank all of the scientists who have contributed to the HITRAN and PNNL/NIST databases. Without their diligence and hard work in providing molecular spectral data, this study would not be possible. I thank Thomas Blake from the Pacific Northwest National Laboratory (PNNL) for providing molecular absorbance data from the PNNL database. I thank my adviser, Sara Seager, for helping me grow in my research career and providing me the opportunity to learn directly from the leading biosignature gas expert. I thank her also for the opportunity to study at MIT and, with that, the opportunity to be surrounded by amazing colleagues from which insightful discussions occur on a daily basis. I thank each member of my research group for helping me throughout the duration of this project. I specifically thank Julien de Wit for helping to properly connect the theory of the transmission spectrum, the transmissivity spectrum, and the effective height of absorption spectrum. I thank all of my friends for their encouragement and support throughout my graduate studies. I finish by thanking my family for their understanding and support as I work towards achieving my career goals.

Contents

List of Figures

List of Tables

Chapter 1

Introduction

1.1 Exoplanets

An exploding research area located at the intersection of the fields of Astrophysics and Planetary Sciences is the study of extrasolar planets. Also termed "exoplanets", these planets revolve around other stars than our Sun. While the first exoplanet orbiting a main sequence star was discovered in 1995 (Mayor and Queloz 1995), over 850 exoplanets have since been identified (see http://exoplanet.eu for up-to-date exoplanet discoveries). One major advancement in the discovery of exoplanets is the *Kepler Space Telescope* which, in only three years of observations, has already identified over 2000 additional planetary candidates.[1] To detect planetary candidates, the *Kepler Space Telescope* is using the transit technique and searching over 150,000 stars in a 115 deg^2 area within the constellation Cygnus with the overall goal of discovering Earth-size planets at Earth-like distances from Sun-like stars (Borucki et al. 2010). The transit technique involves observing the reduction in stellar brightness that occurs when a planet crosses in front of its star from the viewpoint of Earth. One reason for using indirect detection techniques like the transit technique is due to the emission of the planet being swallowed by the enormous flux of stellar radiation. A solar system analog demonstrating how stellar emission overwhelms planetary emis-

[1]Many of these candidates are awaiting follow up confirmation observations by other researchers (e.g., Endl et al. 2011; Cochran et al. 2011).

sion is shown in Figure 1 of Des Marais et al. (2002) where they compare the spectra of the Sun, Jupiter, and some of our terrestrial planets. Conceptually, the difficulty for detecting an exoplanet is similar to trying to detect the light of a firefly located next to a bright search light from a distance of 3000 miles away.

By observing the decrease in stellar brightness that occurs when the planet crosses in front of its host star, the transit technique avoids some of the difficulty involved with the low planet/star flux ratio, though the planet must be sufficiently large to block enough light such that the decrease in stellar brightness is detectable with current and/or near-future technology. For high signal observations, one powerful aspect for utilizing the transit technique is that it allows researchers to investigate the atmospheres of exoplanets. As a planet crosses in front of its star, some starlight travels through the planetary atmosphere and picks up spectral signatures indicative of the composition and structure of the atmosphere. Studying the atmospheres of transiting planets is the key to understanding properties of the planets (e.g., atmospheric composition and temperature/pressure structure, outgassing rates, physical state of the planet, potential to host life, etc.). Atmospheric spectral features have been detected on larger exoplanets such as Hot Jupiters (Charbonneau et al. 2002; Vidal-Madjar et al. 2004; Ballester et al. 2007; Redfield et al. 2008; Swain et al. 2008; Madhusudhan and Seager 2009). Hot Jupiter atmospheric observations are much easier than observing the atmospheres of smaller planets because the corresponding larger atmospheres and larger atmospheric scale heights allow for more stellar photons to traverse the atmosphere and carry spectral information to Earth. The larger planets also block more stellar radiation thus increasing the planet to star flux ratio, which makes detections much easier in general.

Similar atmospheric probing of Earth-size planets could determine the potential for individual Earth-size planets to host life. Though observational technology has not yet reached the ability to investigate atmospheres of Earth-size exoplanets through transit studies, we can predict the anticipated atmospheric transmissivity spectra that would result from transit observations of various types of atmospheres by modeling different atmospheric temperature/pressure/compositional structures via transmissiv-

ity radiative transfer (see Chapter 2 for a full description of transmissivity radiative transfer). In order to focus on atmospheric components indicative of life, I specifically target this radiative transfer method to model biosignature gases (see Section 1.2 for an introduction of biosignature gases). The discovery of such gases in exoplanetary atmospheres will help us determine how similar in composition the observed planets are to Earth and may assist our hunt for life on those exoplanets.

1.2 What is a Biosignature Gas?

A biosignature gas is an atmospheric gas indicative of life. The typical (and hence popular) biosignature gases most often included in theoretical remote sensing studies are oxygen (O_2), ozone (O_3), methane (CH_4), and nitrous oxide (N_2O) (e.g., Léger et al. 1999; Schindler and Kasting 2000; Des Marais et al. 2002; Kaltenegger et al. 2002; Segura et al. 2003; Kaltenegger et al. 2007). The reason for their popularity is due to those biosignature gases being indicative of the current composition of Earth's atmosphere and the desire from the cited researchers to characterize the detectability of planets with atmospheric compositions similar to Earth. One item to note is that water vapor (H_2O), which is termed a "habitability indicator", is not considered a biosignature gas; however, it is deemed necessary for life unless an unknown solvent can provide the same functionality as liquid water.[2] Branching farther away from the stronger Earth-like gases (the first set), some studies have included other (more sulfur-bearing) gases: hydrogen sulfide (H_2S), methyl chloride (CH_3Cl), dimethyl sulfide (DMS; CH_3SCH_3), dimethyl disulfide (DMDS; $CH_3S_2CH_3$), and sulfur dioxide (SO_2) (Hu et al. 2012; Segura et al. 2005; Pilcher 2003; Kaltenegger and Sasselov 2010; Domagal-Goldman et al. 2011). The list of other candidates is growing rapidly. Leaving out aforementioned gases, Seager et al. (2012) review the following extensive list of potential biosignature gases: acetaldehyde, acetone, benzene, carbon disulfide, carbonyl sulfide, dimethyl sulfoxide, ethanol, ethyl sulfide

[2]The existence of liquid water on the exoplanet is one requirement for the planet to be deemed "Earth-like".

(also called ethyl mercaptan), fluroacetone, isoprene, methanethiol, methanol, methyl bromide, methyl ethyl ketone, methyl vinyl ketone, phosphine, 2-thioethanol (also called thioglycol), and toluene. The above lists are not necessarily exhaustive as there are likely other compounds that are indicative of life on Earth; however, the lists demonstrate the large range of molecules that can be used to try to deduce the existence of life in observations of exoplanets.

Since there exists a large range of molecules at our disposal, developing telescopes that can observe within molecular band passes of multiple biosignature gases will be required to provide the greatest opportunity for detecting more than a single species. In reference to detecting multiple species and the search for life, Lovelock (1965) suggested that we could narrow the investigation by searching for gases that exist out of thermodynamic equilibrium in a planet's atmosphere. Due to how fast certain species (e.g., CH_4 and O_2) react in these non-equilibrium atmospheric conditions, simultaneous detection of such species is a good indicator of the existence of life because, without a continual source for each gas, they both could not be detected simultaneously unless the planet was going through a transient phase. The immense knowledge that may be gained from the simultaneous detection of multiple biosignature gases — e.g, knowledge of 1) the structure and composition of the atmosphere, 2) the physical state of the planet, 3) the ability of the planet to host Earth-like life, 4) etc. — fuels the desire to investigate many biosignature gases.

1.3 The Effect of Extremophiles on the Concept of Habitability

With all of the choices for biosignature gases to investigate and the large variety of potential atmospheric constructs, one of the challenges in determining the detectability of atmospheric gases and searching for life is the large habitability parameter space to be explored. We clearly only understand how life exists in a very small subset (only having Earth as an example) of an enormous range of possibilities. In fact, we are still

discovering new species on Earth, many of which live in conditions once thought of as toxic or uninhabitable. For example, Kashefi and Lovley (2003) found that a certain microorganism, designated as strain 121, could live and reproduce at temperatures as high as 121 °C. The same strain even survived being heated to a temperature of 130 °C degrees Celsius. Researchers obtained this organism from a hydrothermal vent in the Northeast Pacific Ocean (Kashefi and Lovley 2003). On the other end of the temperature scale, studies conducted in Antarctica showed that a certain type of bacteria can exist and live at temperatures ranging from −12 °C to −17 °C, which is below the STP freezing point of water (Carpenter et al. 2000). These examples describe life surviving in extreme conditions (based on our current understanding of life) and are not the only examples of discovered extremophiles (e.g., Rothschild and Mancinelli 2001 and references therein). Therefore, there are undoubtedly many sets of conditions and chemistries within the habitability parameter space that, while currently unknown to us, may provide thriving ecosystems for other life forms.

A couple questions now come to mind: what factors play into the habitability parameter space and the detectability of the habitability? and how do we (as a research community) go about detecting life within the enormous habitability space?. As we examine the first question, we realize that factors spanning many disciplines (astronomy, atmospheric chemistry and dynamics, geophysics, etc.) affect the habitability of the planet and the detectability of that habitability, and, therefore, we must draw upon expertise from all associated fields in order to fully understand and address the first question. Some example factors affecting habitability and the detectability of the habitability from the different fields listed above include the spectral type of the parent star, degree of stellar activity, processes that influence atmospheric escape, the temperature/pressure structure of the atmosphere of the planet, the circulation and heat transfer of the atmosphere of the planet, the atmospheric chemistry and photochemistry, plate tectonics, outgassing of atmospheric species, etc. Understanding the mechanisms governing each of these properties will allow us to better predict how they influence habitability and the detectability of the surrounding atmosphere. Furthermore, understanding how all of these factors/processes interact with each other

will explain the reasoning behind the composition of each exoplanet atmosphere.

We now reach the second question listed above: how should the research community proceed with detecting life in the enormous habitability parameter space? Many possible pathways involving biosignature gases appear for answering this question. One option is to analyze biosignature gases that appear strong on Earth. We (as a community) can investigate their sources, sinks, and how they survive within the atmosphere. We can use Earth-like conditions around a Sun-like star and thereby closely model Earth-analog exoplanets through theoretical remote sensing studies. For alternative remote sensing studies, we could choose to use the Earth-like conditions but put that planet around a different stellar class (e.g., an M star) than the Sun (a G star).[3] This decision changes the incident stellar flux extant the atmosphere which will influence its temperature, pressure, and compositional structure. The benefit of using Earth-like atmospheric conditions is that observational and experimental data exist. Once the models leave the Earth's construct, many of those quantities become free parameters and narrowing down proper choices becomes increasingly difficult without expertise in the fields and processes listed above.

Since the parameter space is so large, diversifying the research angles may provide the best means by which to tackle biosignature gas research. Conducting studies that are purely Earth-like, modified Earth-like, and, eventually, environments completely different from Earth will all add to our growing knowledge and understanding of the habitability of exoplanets and the detectability of their atmospheres. Each angle shows promise and must be pursued. The approaches that recent studies have taken are detailed below.

[3]As the parent star and planet form from the same stellar nebula, the formation of a different spectral class parent star (than the Sun) may affect the composition and/or structure of the surrounding planets and their corresponding atmospheres (both primordial and possibly steady state atmospheres). As many questions lay unanswered in planet formation theory, it is currently not possible to draw a conclusion of how the initial mass (or other properties) of the stellar nebula and how the particular spectral class of the resulting parent star affect the properties of the planets forming around the star. Therefore, future theoretical research in this area including comparisons to statistical observational studies (e.g., the *Kepler Space Telescope* study) hold much promise since such studies may unveil correlations between the properties of the planets in the exoplanetary system and the mass of the initial stellar nebula, the metallicity of the system, etc.

1.4 Previous Models of Biosignature Gases

Previous theoretical remote sensing studies have investigated the detectability and concentrations of biosignature gases in Earth-like planet atmospheres or modified Earth-like planets' atmospheres through one or more potential radiative transfer techniques that can be used to detect the constituents of an atmosphere (e.g. transmission radiative transfer, thermal emission radiative transfer, and scattering radiative transfer). Though my study focuses solely on transmissivity radiative transfer (a version of transmission radiative transfer), explanations of alternative studies will provide a fuller understanding of the current state of the field along with introducing various case studies of specific exoplanet environments. I will begin by briefly discussing the targeting of the *TPF*/*Darwin*-type missions as these missions, though currently postponed, are the most likely type of missions to characterize the atmospheres of Earth-like exoplanets. I then introduce studies that have investigated slightly different conditions than pure Earth-like conditions (i.e. detectability around M stars and early Earth biosignature gases) in order to describe specific case examples of the large parameter space requiring investigation. I end the previous work section by summarizing studies that focus specifically on transmission radiative transfer and are thus more comparable to this manuscript.

1.4.1 Focusing the *Terrestrial Planet Finder* (*TPF*) and *Darwin*-type Missions

In preparation for developing the *TPF*/*Darwin*-type missions[4], studies have been conducted in order to determine the necessary observational requirements. Using Earth-like conditions for their models, Des Marais et al. (2002) analyze the biosignature gases O_2, O_3, CH_4, and N_2O in reference to setting criteria for the *TPF*/*Darwin*-type missions. For each gas, they deduce the best wavelength regions from which spectral features can be detected by paying particular attention to determining where the

[4]The mission objective for any *TPF*/*Darwin* design is to discover and characterize terrestrial-sized planets with specific emphasis on finding Earth-like planets in the habitable zone of nearby stars. Both the *TPF* and *Darwin* missions are currently shelved.

spectral features will not be swallowed by stronger H_2O or CO_2 absorption. Based on the combination of those preferred wavelengths with the peaks of the stellar reflection spectrum and Earth's thermal emission spectrum, they recommend that the *TPF/Darwin* telescopes should be built such that the telescopes can observe within the the visible to near-IR from $0.5 - 1.1$ μm and the mid-IR from $7 - 25$ μm.

1.4.2 Detectability of Biosignature Gases on Earth-like Planets around M Stars

Seventy-five percent of stars within the Milky Way Galaxy are M stars (Segura et al. 2005), thus it is important to question the possible existence of habitable exoplanets around such stars. Using Earth-like atmospheric conditions on an M star planet, Segura et al. (2005) investigate the possibility of detecting the biosignature gases oxygen, ozone, methane, nitrous oxide, and methyl chloride. They included these particular molecules due to their abundance and importance to Earth's atmosphere. While they admit that other biosignature gases, e.g., ammonia or ethylene, could have been included, they chose to ignore such gases due to their short atmospheric lifetimes (Segura et al. 2005). Methyl chloride has not been included in many biosignature gas studies as compared with the more popularly chosen oxygen; however, they chose to include this species due to its effect on atmospheric chemistry.

Through their models, Segura et al. (2005) predict that mixing ratios (a measure of atmospheric abundance) for CH_4, N_2O, and CH_3Cl are much higher (orders of magnitude in some cases) for M star planets than the case for Earth. The increased abundances may allow for easier detection on M star planets as the spectral features should be more pronounced. The methane case sheds light on the different effect that M star radiation has on a planetary atmosphere as compared to solar type radiation. Segura et al. (2005) state that the main sink for CH_4 is chemical reactions with OH. The production of OH is strongly dependent on the flux of stellar radiation between 200 and 300 nm. M stars emit less emission within this wavelength range as compared to solar type stars thereby leading to decreased OH production

in the atmospheres of M star planets. With a lower OH abundance, methane builds up in the atmosphere.[5] As OH also destroys CH_3Cl, M star planets with less OH could have higher atmospheric abundances of CH_3Cl than Earth (Segura et al. 2005). For ozone, they find a similar absorption depth as for Earth and conclude that the ozone layer is large enough to protect the surface from harmful UV radiation (Segura et al. 2005). In reference to the previous discussion of biosignature gases that require continuous sources for simultaneous detection, they propose that it may be easier to simultaneously detect O_2 (or O_3) and either CH_4, N_2O, or CH_3Cl on an M star planet than on an Earth-like planet around a Sun-like star. They support previous conclusions (e.g., Lovelock 1965; Kaltenegger et al. 2002) that such simultaneous detections would provide strong evidence for the existence of life on that planet (Segura et al. 2005).

1.4.3 Biosignature Gases of the Early (Young) Earth

The early Earth (approximately the first 1.5 billion years of Earth's existence) had different atmospheric conditions (i.e. more reduced, which means much less O_2) than its present state; however, life did not require abundant atmospheric oxygen in order to develop (Domagal-Goldman et al. 2011 and references therein). In fact, life existed about 1.5 billion years (Gyr) before the upswing in atmospheric oxygen abundance (Schopf and Walter 1983; Schidlowski 1988; Mojzsis et al. 1996; Des Marais 1998; Schopf 1999; Kasting 2001; Pilcher 2003).[6] With the 1.5 billion year time span equaling about one-third of Earth's current lifetime, Domagal-Goldman et al. (2011) predict that there could exist a large number of inhabited planets with these early Earth conditions.[7] If exoplanets in early Earth stages exist, then we should anticipate

[5]The lifetime of CH_4 on Earth is about $10-12$ years; however, on M star planets, the lifetime increases to about 200 years (Segura et al. 2005). This increased lifetime (which leads to large atmospheric abundances) will provide a better chance for remote detection.

[6]Oxygen became abundant in Earth's atmosphere around 2.3 billion years ago while life formed about $3.5 - 3.8$ billion years ago (Pilcher 2003 and references therein).

[7]The sole case of the Earth switching from an anoxic atmosphere to its current state does not provide enough evidence that all planets would behave similarly; therefore, it is possible that planets could sustain anoxic conditions and life throughout their evolution. If the lifetime of the habitable anoxic planetary conditions increases beyond 1.5 Gyr, then the overall population of these sources will increase, leading to easier detections of this potential class of habitable planets.

that typical biosignature gases (e.g., oxygen and ozone) may not be good indicators in such systems.

Pilcher (2003) and Domagal-Goldman et al. (2011) investigate anoxic conditions representative of the early Earth. Methanogenesis and sulfur respiration were important processes for the early Earth; therefore, Pilcher (2003) suggest the subsequent reduced gases: methane, DMS, DMDS, and methanethiol as potential biosignature gases. The Domagal-Goldman et al. (2011) study chose to include carbon disulfide (CS_2) and carbonyl sulfide (OCS) in addition to DMS, DMDS, and methanethiol. They chose against including H_2S due to its large abiotic source term from volcanism.

Problems exist for detecting some of the above gases in atmospheric spectra. Methanethiol, DMS, and ozone have overlapping spectral features, therefore, distinguishing between the molecules may require high spectral resolution (Pilcher 2003). For added complication, water vapor features overlap many of the molecular bands of reduced gases, thus creating additional detection problems if water is abundant in the exoplanet atmosphere.

The atmospheric abundance of a biosignature gas plays an essential role in its detectability. Greater abundances lead to deeper absorption features and thus easier detection. In reference to detection with the *TPF*, Pilcher (2003) finds that methanethiol would require an abundance greater than 0.1%, while a methane atmospheric concentration of 1% could indicate methanogenic life.

Domagal-Goldman et al. (2011) furthered their analysis of the early Earth environment by analyzing the impact of three UV stellar fluxes [Sun-like, Ad Leo (an active M dwarf), and T3100 (a model M dwarf with surface temperature of 3100 Kelvin)] incident on an anoxic atmosphere. Expectedly, the mixing ratios of their gases increase as the UV flux decreases or the production of the species increases.[8] In fact, the 7 μm DMS feature and the DMDS and CH_3SH features between 9 and 11 μm were only visible for low UV fluxes or a 30 times increase in their production

[8]UV photons destroy these molecules, which explains why a lower UV flux leads to higher molecular abundances.

(with respect to Earth's current production; Domagal-Goldman et al. 2011). It must be noted that the above gases have features within Earth's $8 - 12$ μm atmospheric window. The $8 - 12$ μm wavelength range has been projected as a good candidate for exoplanet surface temperature measurements due to its transparency in Earth's atmosphere; however, the overlapping features from many biosignature gases may hinder the surface temperature measurements. Observing in other wavelength regions may provide the evidence necessary to disentangle the absorption features from surface temperature estimates in the 8 to 12 μm window (Domagal-Goldman et al. 2011).

Both Pilcher (2003) and Domagal-Goldman et al. (2011) provide even more intriguing, thought-provoking conclusions. Pilcher (2003) introduces an interesting distinction between their biosignature gases and other typical biosignature gases (e.g., oxygen, ozone). Since biosignature gases like oxygen and ozone result from biological processes, these gases describe processes that life conducts; however, the reduced biosignature gases due to how they are produced (many created by splitting off of a larger molecule like methionine) describe what composes life (Pilcher 2003). Domagal-Goldman et al. (2011) develop an equally interesting conclusion. They contradict previous biosignature arguments which state that we should be looking for systems out of equilibrium (e.g., Lovelock 1965). They state that photochemical disequilibrium may not indicate life in all conditions because anoxic inhabited systems may exist in equilibrium. Both of these conclusions introduce important concepts that the field must investigate further in order to fully understand the interaction between biosignature gases, life, and the environment.

1.4.4 Previous Transmission Radiative Transfer Studies

Ehrenreich et al. (2006) used a theoretical model of transmission spectroscopy to extend the models of Schneider (1994) and Webb and Wormleaton (2001) (which both focused on the detection of the oxygen A-band located at 760 nm) by investigating molecular absorption features between $200 - 2000$ nm from four atmospheric gases: water, carbon dioxide, ozone, and oxygen. In order to explore some of the atmo-

spheric parameter space, they model three atmospheric types: (1) N_2/O_2-rich, (2) CO_2-rich, and (3) N_2/H_2O-rich. The first two atmospheric compositions model an Earth-like atmosphere and a Cytherean atmosphere, respectively, while Ehrenreich et al. (2006) note the last composition to possibly be indicative of a water world. Interestingly, they analyze these three atmospheric compositions for each possible combination of three stellar spectral classes (an F, G, and K star) and three sizes of planets (with planet radii equal to one Earth radii, one-half an Earth-radii, and two Earth-radii). For the biosignature gases, they find that ozone provides a much better opportunity for detection within this wavelength region as their models do not return detectable oxygen features for their 10 nm resolution. They attribute the non-detectability of oxygen to the narrowness of the spectral features. The specific detectability (i.e. signal-to-noise ratios) for each of their atmospheric gases for each model can be found in their Table 3. The parameters that influence this detectability (e.g., stellar spectral type, atmospheric temperature gradient, atmospheric pressure, the planet's gravity and density) are discussed in their work, and their discussions are beneficial to the development of an intuition of the effects of these model parameters.

Kaltenegger and Traub (2009) focus on a much larger wavelength range ($0.3 - 20$ μm) than that of Ehrenreich et al. (2006). Their transmission spectrum analysis for an Earth-analog projects the detection of ozone and methane between $0.3 - 20$ μm and possibly oxygen within the wavelength range of $0.3 - 4$ μm.[9,10] They find that detections of oxygen, ozone, and methane are not possible with single transit observations and thus co-adding transits will be required, especially for a 6.5 m telescope [akin to the *James Webb Space Telescope* (*JWST)*]. For each analyzed gas, they list the anticipated SNRs that would occur for 200 hours of co-added observation (with a 6.5 m telescope) for planets revolving around a Sun-like star and a variety of M stars. To put the 200 hours of observation time into perspective, they list the number of transits and number of years that would be required to meet this observational time limit for the Sun-like star and each of their modeled M stars. The combina-

[9]These results take into account the spectral masking from water and carbon dioxide.

[10]They focus their studies on a 6.5 m telescope and, in many cases, use anticipated parameters for the *James Webb Space Telescope*.

tion of the 6.5 m telescope and the 200 hours of observation time is not sufficient to definitively detect all of the molecules (e.g., methane) for all stellar spectral types.[11] Improvement to these SNRs could occur by increasing the telescope size or increasing the observation time. The interplay between these two parameters in reference to reducing observational noise is discussed in Section 4.5.

For their transmission radiative transfer study, Rauer et al. (2011) investigate a similar wavelength region ($2 - 20$ μm) as Kaltenegger and Traub (2009). They analyze both Earth-like and super-Earth planets, though I only detail the results from their Earth-like planet case. They model several different stars (Sun-like, quiet M dwarves, and an active M dwarf) to determine the change in the resulting transmission spectra that occurs from changing stellar type. A very important distinction between the Rauer et al. (2011) study and the Kaltenegger and Traub (2009) is that Rauer et al. (2011) used consistent M dwarf stellar spectra to calculate the atmospheric temperature and pressure profiles of their modeled gases while Kaltenegger and Traub (2009) used Earth-representative profiles for their M star studies. Rauer et al. (2011) claim that the differences in their results as compared to Kaltenegger and Traub (2009) are significant, and thus, they emphasize that the use of a consistent model is important.

In reference to biosignature gases of interest to my work, Rauer et al. (2011) find that absorption from ozone, methane, and nitrous oxide could be detected in their transmission spectra. In their Table 3, they provide the SNRs for ozone and methane absorption for a single transit for a telescope configuration similar to the *JWST*. Their SNR results indicate that the stacking of multiple transits could provide for detectable signals [a similar conclusion as in Kaltenegger and Traub (2009)]. To this end, they detail the required observational parameters to achieve an SNR equal to 3 for their active M dwarf and an M5 star. As previously indicated, detections of at least 5σ will provide a much more believable spectral signature than that of a 3σ detection; thus, studies focusing on more reliable detections should plan accordingly.

[11] The exact detection metric may vary between researchers; however, it seems relatively accepted that a 5σ detection is satisfactory. Some studies (like this current work) require much higher SNRs (e.g., 10).

1.5 Motivation

The main ten biosignature gases chosen for this study are oxygen, ozone, methane, nitrous oxide, methyl bromide, methyl chloride, hydrogen sulfide, carbonyl sulfide, phosphine, and sulfur dioxide. Two gases in this ensemble, methyl bromide and phosphine, have not been investigated previously. While the other eight gases have received variable amounts of attention, my study analyzes them in a different manner (see below). The limiting criteria for the detailed analysis of a biosignature gas in this study is the existence of spectral line intensity data that can be mapped to different temperatures and pressures. The ten aforementioned gases have mapable spectral data courtesy of the HIgh-resolution TRANsmission molecular absorption (HITRAN) database (Rothman et al. 1998; Rothman et al. 2009). I will refer to these ten gases as "HITRAN biosignature gases". Since the molecular data for the HITRAN biosignature gases can be mapped to varying temperatures and pressures, I analyze these gases in depth (see below). Sixteen additional (and non-standard) biosignature gases included in my study do not have absorption cross sections that are currently mapable to alternative temperatures and pressures; therefore the investigation into these gases is unfortunately limited. These sixteen biosignature gases are acetaldehyde, acetone, benzene, carbon disulfide, dimethyl disulfide, dimethyl sulfide, dimethyl sulfoxide, ethanol, ethyl mercaptan, fluoroacetone, isoprene, methyl ethyl ketone, methyl mercaptan, methyl vinyl ketone, thioglycol, and toluene. The molecular data for these gases was retrieved from the Pacific Northwest National Laboratory (PNNL) database (Sharpe et al. 2004) and the National Institute of Standards and Technology (NIST) Quantitative Infrared database (Chu et al. 1999). I will refer to these sixteen biosignature gases as the "PNNL/NIST biosignature gases". I discuss the motivation for my work below.

Many of the previous studies (see Section 1.4) have focused on what spectral signatures would be detectable given atmospheric mixing ratios representative of a present-day Earth-analog or of different stages of Earth's atmospheric evolution. These studies have been very beneficial to the field as they have helped to determine

what we could observe for those particular planetary constructs. However, what if an exoplanet was almost Earth-like but had different atmospheric mixing ratios for one or more particular biosignature gases as compared to Earth? How large would the mixing ratio of these gases need to be in order for them to be detectable? One of the goals of my study is to determine the threshold mixing ratios required for molecular detection. Even though some of Earth's biosignature gases do not achieve these threshold mixing ratios in the current atmosphere of Earth, slightly different atmospheric chemistries and/or different source terms may allow them to constitute larger portions of exoplanet atmospheres, and thus, this region of the parameter space must be explored. For the HITRAN biosignature gases, I modeled transmissivity spectra of varying atmospheric mixing ratios of each HITRAN gas to determine threshold mixing ratios for successful detection with four telescope sizes (20 m, 35 m, 50 m, and 100 m; see Chapters 3 and 4). For the PNNL/NIST gases, since their absorption cross sections are not currently mapable to different temperatures and pressures, I was limited to estimating threshold mixing ratios (for detection with a 35 m telescope) using a few HITRAN biosignature gases as a reference point (see Section 4.7).

Some of the previous studies focus solely on very particular (i.e. popular) wavelengths for each biosignature gas (e.g., the 9.6 μm ozone feature). Determining alternative wavelengths to detect each biosignature gas is important for two reasons. The first reason for studying multiple features for each molecule is that future observations will produce spectra from which we will have to determine the species responsible for each absorption. A full knowledge of all possible absorption wavelengths for each molecule will help observers to identify all possible species that could lead to a particular absorption feature. Second, comparisons between the absorption strengths of multiple wavelength bands allows for better constraints on the atmospheric abundance of the gas. With better constraints on the atmospheric abundance, we can remove the contribution of each species from the absorption profile until we account for all major atmospheric species (i.e. species with large enough abundances to make an impact on the absorption spectrum). To aid future observational research with disentangling the absorption of atmospheric biosignature gases, I have investigated

in detail alternative molecular features that may prove useful for the detection and characterization of the HITRAN biosignature gases in exoplanetary atmospheres. For the PNNL/NIST biosignature gases, I only was able to predict where (in wavelength space) the PNNL/NIST gases may have spectral features based on an analysis of their absorption cross sections at a single temperature (296 K) and pressure (1 atm). Since I am unable to map the PNNL/NIST absorption cross sections to different temperatures and pressures, it is unknown if all of the predicted features would appear in the end transmissivity spectrum of the same model as that used for the HITRAN biosignature gases.

Many of the previous radiative transfer studies have been streamlined to predict results from telescopes of the same class as the *JWST*. In general, with the exception of the *TPF*/*Darwin*-type studies, not much work has been done for telescopes larger than the *JWST*. To this end, I have focused investigations on varying telescope sizes (most larger than the *JWST*) in order to demonstrate the detection levels (i.e. signal-to-noise ratios) that can be reached with each class of telescopes. My results frame the minimal observational requirements to detect the HITRAN biosignature gases with reference to varying levels of detectability. I then use those HITRAN biosignature gas results to predict atmospheric threshold mixing ratios required for the detection of the PNNL/NIST gases.

In Chapter 4, I investigate two additional topics through case studies: (1) the interaction between telescope aperture size and observation duration in reference to decreasing the noise budget and (2) the technological requirements for observing biosignature gases in low signal regions (the millimeter region for this case study). The core of both case studies involves increasing observational signal. An increase in signal will directly lead to the ability to detect lower atmospheric abundances of biosignature gases and/or the ability to probe longer wavelengths. As many biosignature gases exist in low abundances on Earth ($<$ ppm level), the ability to detect lower atmospheric molecular abundances on exoplanets will prove beneficial. In reference to the second case study listed above, the existence of long-wavelength features for many of the biosignature gases fuels my desire for increasing signal in long-wavelength

regions. Through the combined implications of both case studies — namely, (1) the difficulty associated with increasing signal in transit observations, (2) the necessity for a dramatic increase in the technological level of next-generation observational technology (e.g., a 35 m telescope is desired), and (3) the potential for creativity (e.g, utilizing a multi-telescope array consisting of smaller and more economical telescopes) instead of brute force (e.g., building one large telescope that could succumb to similar difficulties as the *JWST*) to be required for next-generation technologies and discoveries — I illuminate a current difficulty in the field, designate research areas that require growth for the future advancement of the field, and provide some framework for future work to address the presented difficulty and the needed growth.

1.6 Thesis Outline

Chapter 2 details transmissivity radiative transfer theory and the model used for the transmissivity radiative transfer calculations. Chapter 3 presents the results while Chapter 4 discusses their implications. The main findings and a short conclusion can be found in Chapter 5.

Chapter 2

Transmissivity Radiative Transfer Theory and Model

I now develop the transmissivity radiative transfer theory and model used for the in-depth analysis of the HITRAN biosignature gases listed in Section 1.5. All theory and discussion of the PNNL/NIST biosignature gas investigation can be found in Section 4.7. As the derivation in this chapter encounters new parameters, I often step away from the main derivation to systematically explain each parameter. After the full theory is presented, I describe the simulated observations, the model parameters, and the methodology of exploration. Throughout this chapter, I have incorporated many of the hidden intricacies that are not illuminated in standard texts. My goal for these descriptions is to ease the learning curve for theoretical transmissivity radiative transfer studies thereby providing a better learning platform for other researchers.

2.1 Radiative Transfer Theory

In order to dissect the light received from the atmosphere of an exoplanet, we must understand how the atmosphere changes the incident stellar light. Radiative transfer theory, which describes how light interacts with a medium, provides the basis for understanding these interactions. The difference between the beam of radiation (from the star) extant the atmosphere and the beam of radiation exiting the atmosphere

and encountering our detector can be interpreted via the losses and gains to the beam during transit through the atmosphere. If we assume a static atmosphere, then we can use the radiative transfer equation from Seager (2010) to describe the losses/gains to the beam of radiation, namely:

$$\frac{dI(\vec{x},\vec{n},\nu)}{ds} = -\kappa(\nu)\cdot I(\vec{x},\vec{n},\nu) + \epsilon(\vec{x},\vec{n},\nu), \tag{2.1}$$

where $\vec{x}$ represents the position in space, $\vec{n}$ is the normal vector to the direction of travel of the radiation, and ν is the frequency of radiation. The left side of the equation, $dI(\vec{x},\vec{n},\nu)/ds$, designates the change in the intensity of the beam of radiation, $dI(\vec{x},\vec{n},\nu)$, over the path length, ds, that the light traverses in the medium. The first term on the right hand side of Eq. (2.1), $\kappa(\nu)\cdot I(\vec{x},\vec{n},\nu)$, represents the losses to the beam based on the extinction coefficient, $\kappa(\nu)$, multiplied by the intensity, $I(\vec{x},\vec{n},\nu)$, of the radiation. The second term on the right hand side of Eq. (2.1), $\epsilon(\vec{x},\vec{n},\nu)$, accounts for the gains to the beam of radiation through the emission coefficient, $\epsilon(\vec{x},\vec{n},\nu)$. By incorporating the impact of every atmospheric particle on the incoming beam of radiation, I can calculate the resultant outgoing intensity. I note that Eq. (2.1) satisfies only time-independent systems and that adjustments to this equation must be made for time-dependent atmospheres (see Seager 2010 for further details).

In terms of solving the radiative transfer equation, Eq. (2.1) can be broken into three subgroups: thermal emission, scattering, and transmission. Each of the subgroups describe different interactions the incident stellar light could encounter. Thermal emission radiative transfer theory describes the light that is emitted by atmospheric particles that had previously absorbed either incident stellar light or radiation released from the planetary interior. Scattering radiative transfer theory addresses the light that interacts with atmospheric particles via scattering processes. Transmission radiative transfer theory focuses on analyzing the light that passes through the planetary atmosphere without being affected by particles within that atmosphere. While an analysis that incorporates all three mechanisms would fully describe the

exiting spectrum arriving at the detector located at Earth, such a study is beyond the scope of the current work. Since some exoplanet atmospheres have already been observed in transmission (Seager and Deming 2010 and references therein) and since transmission observations appear to be the direction the research field is heading, I choose a version of transmission radiative transfer called transmissivity radiative transfer as the starting point for biosignature gas studies.

2.1.1 Transmissivity Radiative Transfer Derivation Part I

For transmission/transmissivity spectroscopy to be possible, particular system geometry is required. The planet must transit its star as seen from a detector at Earth (see Fig. 2-1). In this manner, the detector can intercept the stellar light that picked up spectral signatures as the light traveled through the planetary atmosphere. If the planet is not in transit, then transmission/transmissivity observations are not possible (from a detector located at Earth). For out-of-transit atmospheric studies, one must observe scattered stellar light or thermal emission from the atmosphere. Due to the limited number of photons for these cases in comparison to transmission/transmissivity spectroscopy, high signal-to-noise detections become increasingly difficult. Furthermore, current technology cannot spatially resolve the atmosphere of an exoplanet, and, with the intense stellar radiation emitted, any photons from scattering or atmospheric thermal emission are likely to be drowned by the stellar flux.

For the current work, I solely model transmissivity spectra. I separate out thermal emission and scattering processes from the transmissivity analysis by assuming that the light exiting the planetary atmosphere does not have any gains due to emission or scattering of photons into the exiting beam. This assumption provides that the emission coefficient $\epsilon(\vec{x}, \vec{n}, \nu) = 0$ in Eq. (2.1) thus leading to

$$\frac{dI(\vec{x}, \vec{n}, \nu)}{ds} = -\kappa(\nu) \cdot I(\vec{x}, \vec{n}, \nu). \tag{2.2}$$

Through a technique called the plane parallel approximation, I break the atmosphere

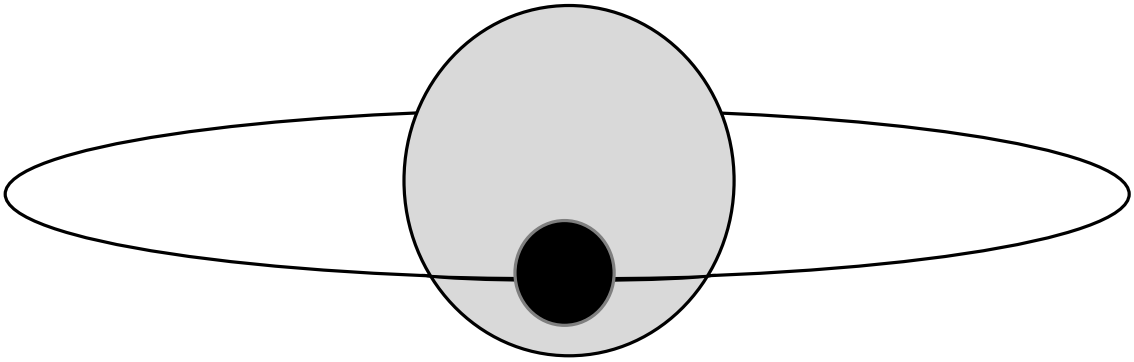

Figure 2-1: Illustration of a planet transiting its parent star. If the Earth is in line with the planet and star in this configuration, then a detector at Earth can observe the stellar light that passes through the planetary atmosphere. The atmosphere of the planet is shown in dark grey, while the planet is black and the star is light grey. The sizes are not necessarily to scale.

into concentric shells with constant temperature, pressure, and number density of particles in each shell. With axial symmetry, I find that the derivatives of intensity in the x and y directions drop out and, using z as the vertical axis (i.e. the altitude), that $\frac{dz}{ds} = cos(\theta) \equiv \mu$, where θ is the angle between the surface normal vector $\vec{n}$ and the radiation beam (Seager 2010). As μ represents the dependence on the surface normal vector and the position vector $\vec{x}$ is now only one dimensional within z, Eq. (2.2) becomes

$$\mu \frac{dI(z, \mu, \nu)}{dz} = -\kappa(z, \nu) \cdot I(z, \mu, \nu). \tag{2.3}$$

Equation (2.3) explicitly shows that the extinction coefficient is dependent on both

altitude, z, and frequency, ν. The extinction coefficient dependencies are very important and must be accounted for in any radiative transfer calculations. I now rearrange Eq. (2.3) into a more solvable form:

$$\frac{dI(z,\mu,\nu)}{I(z,\mu,\nu)} = -\frac{1}{\mu}\cdot\kappa(z,\nu)dz. \tag{2.4}$$

Upon integration of Eq. (2.4) over the interval encapsulated by the initial and final positions, z_i and z_f, respectively, we receive

$$\int_{z_i}^{z_f}\frac{dI(z,\mu,\nu)}{I(z,\mu,\nu)} = -\int_{z_i}^{z_f}\frac{1}{\mu}\kappa(z,\nu)dz \Longrightarrow I(z_f,\mu,\nu) = I(z_i,\mu,\nu)e^{-\frac{1}{\mu}\int_{z_i}^{z_f}\kappa(z,\nu)dz}. \tag{2.5}$$

In Eq. (2.5), the exponent of the exponential on the right hand side of the equation is the definition of optical depth, τ_ν (Seager 2010). I utilize this definition to arrive at Beer's Law which describes the transmitted intensity:

$$I(\tau_\nu,\mu,\nu) = I(0,\mu,\nu)e^{-\tau_\nu}. \tag{2.6}$$

The left side of Beer's Law, $I(\tau_\nu,\mu,\nu)$, represents the combined spectrum of the star and atmosphere, while the intensity on the right hand side, $I(0,\mu,\nu)$ (where optical depth $\tau_\nu = 0$), designates only the stellar intensity. The right side of Eq. (2.6), $I(0,\mu,\nu)\cdot e^{-\tau_\nu}$, can be conceptually viewed as the stellar spectrum with "bites" taken out due to the absorption of the atmosphere.

The subtleties of Eq. (2.6) and, subsequently, the subtleties of the transmissivity radiative transfer equation derived below [Eq. (2.11)] lie entwined with the frequency-dependent optical depth. I note here that I assume that the optical depth equals zero both between the star and the planetary atmosphere and between the atmosphere and the detector located at Earth, such that the light is only affected by the planet's atmosphere and not by the interstellar medium.

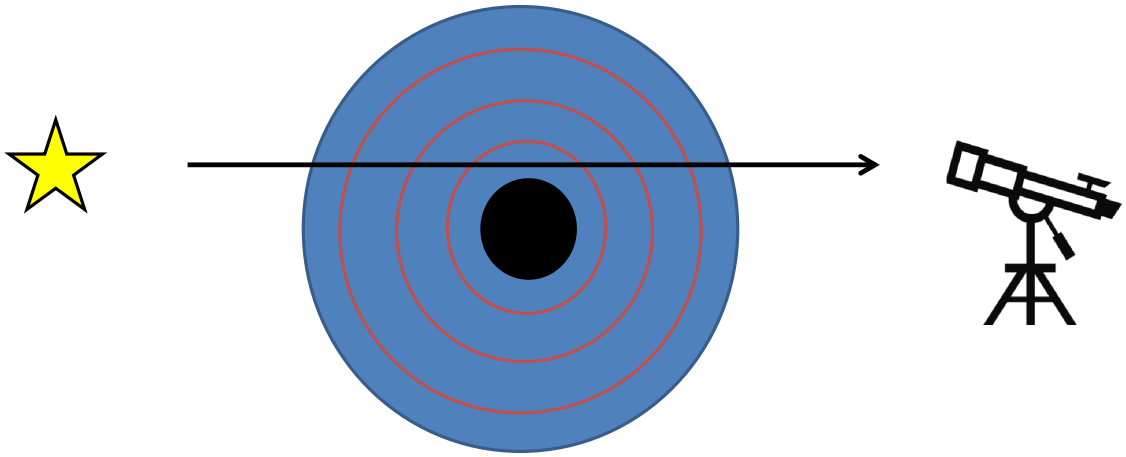

Figure 2-2: Exaggerated atmospheric layers of an exoplanet atmosphere. The center black circle designates the solid portion of the planet, while the red rings indicate boundaries between layers in the atmosphere with different temperature, pressure, and number density of molecules. The arrow indicates an example path travelled by incident stellar radiation to the detector. This figure is not to scale.

2.1.2 Dissecting Optical Depth Part I

The variable τ_ν is the key to calculating theoretical transmissivity spectra. In my models, light travels from the star, through the planetary atmosphere, and impacts the detector located at Earth. As the light travels through the atmosphere, it interacts with many atmospheric layers, each with a different pressure, temperature, and concentration profile. The effects from these differing layers are incorporated into Eq. (2.6) through the optical depth parameter:

$$\tau_\nu(w) = \int_{w_{initial}}^{w_{final}} \kappa(w) dw = \int_{w_{initial}}^{w_{final}} n(w)\sigma dw, \tag{2.7}$$

where $\kappa(w)$ is the extinction coefficient and equals $n(w)\cdot\sigma$, $n(w)$ is the number density of atmospheric particles, σ is the absorption cross section of the molecule, $w_{initial}$ is the location at which the light enters the atmosphere, w_{final} is the location at which the light exits the atmosphere, and dw is the path length the light travels in the atmosphere. To make the path (i.e. "w") indices much simpler, I take advantage of atmospheric symmetry about the geometric north/south axis. In this case, I simplify Eq. (2.7) to

$$\tau_\nu(w) = \int_{w_{initial}}^{w_{final}} n(w)\sigma dw = 2\cdot\int_0^{w_{final}} n(w)\sigma dw. \tag{2.8}$$

I then change coordinate systems by utilizing the right triangle depicted in Fig. 2-3, thus changing Eq. (2.8) from its w (path length) dependence to an r (radial) dependence. Using the right triangle in Fig. 2-3, I find $w = \sqrt{(r^2 - h_2^2)}$, which leads to $dw = \frac{r}{\sqrt{(r^2-h_2^2)}}dr$. I must now change the $n(w)$ dependence into $n(r)$. To calculate $n(r)$, I use the ideal gas law $n(r) = \frac{P(r)}{k\cdot T(r)}$, where $P(r)$ designates atmospheric pressure (altitude dependent), k equals Boltzmann's constant, and $T(r)$ designates atmospheric temperature (altitude dependent). Substituting these relations into Eq. (2.8), I find

$$\tau_\nu(h) = 2\int_{h_1}^{R_1} n(r)\sigma\cdot\frac{r}{\sqrt{r^2-h_2^2}}dr. \tag{2.9}$$

My goal with Eq. (2.9) is to calculate an optical depth for every atmospheric layer (see Section 2.6.1 for atmospheric layer geometry). I evaluate $n(r)$ at the center of each layer and use this value as the particle number density for the entire layer. The parameter h_2 is the distance between the center of the planet and the middle of the atmospheric layer corresponding to $n(r)$. For the indices of integration, h_1 is the distance between the center of the planet and the bottom of the atmospheric layer corresponding to $n(r)$, and R_1 is the distance between the center of the planet and the top of the atmospheric layer corresponding to $n(r)$. Since $n(r)$, h_2, and the limits of integration are different for every layer of the atmosphere, care must be taken in order to properly evaluate Eq. (2.9). The end result for $\tau_\nu(h)$ is a vector with a value for optical depth corresponding to every atmospheric layer.

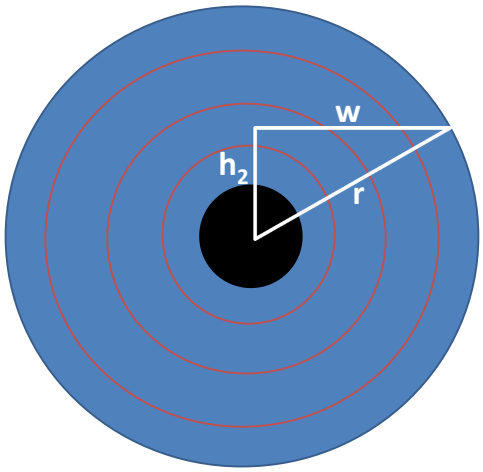

Figure 2-3: Geometric interpretation of a planetary atmosphere. This figure models a geometry similar to that of Figure 2-2. In this manner, the star would be on the left side of the planet in the plane of the paper while the detector (located at Earth) would be to the right of the planet and also in the plane of the paper. Light would travel from the star through the planetary atmosphere to the detector on lines parallel to that designated as "w" in this figure.

2.1.3 Transmissivity Radiative Transfer Derivation Part II

By recognizing the optical depth height dependency as presented in Eq. (2.9) and dividing Eq. (2.6) by the incident stellar radiation, $I(0, \mu, \nu)$, I find the height dependent atmospheric intensity, $I_a(h)$:

$$I_a(h) = \frac{I(\tau_\nu, \mu, \nu)}{I(0, \mu, \nu)} = e^{-\tau_\nu(h)}. \tag{2.10}$$

The transmissivity spectrum radiative transfer solution can then be obtained by integrating $I_a(h)$ over the entire atmosphere and dividing by the total area of the atmosphere such that

$$Transmissivity = \frac{1}{\pi(R_p^2 - R_s^2)} \int_{h_{bottom}}^{h_{top}} I_a(h) \cdot 2\pi h dh, \tag{2.11}$$

where R_p equals the distance between the center of the planet and the top of the atmosphere, R_s equals the distance between the center of the planet and the surface

of the planet, h_{bottom} equals the distance between the center of the planet and the bottom of the atmospheric layer corresponding to $I_a(h)$, and h_{top} equals the distance between the center of the planet and the top of the atmospheric layer corresponding to $I_a(h)$. Though Eq. (2.11) is the "end" equation that provides all of the results, many subtleties are folded into this equation. Explanations of these intricate details are described in the remaining sections of this chapter. For details concerning the relationship between the transmissivity spectrum, the transmission spectrum, and the effective height of absorption spectrum, please see Appendix A.

2.1.4 Temperature and Pressure Shell Structure

One of the intricate details requiring discussion is the temperature and pressure shell structure of the atmosphere. As seen in the ideal gas law, $n(r)$ is dependent on both temperature and pressure which both vary with altitude above the planetary surface. By breaking the atmosphere into concentric shells, each with its own temperature, pressure, and thus number density of particles, I can more accurately model the atmosphere. Since the temperature and pressure structure of an atmosphere affects its $n(r)$ and its absorptive properties (through the molecular cross section σ), one difficulty in atmospheric modeling is properly determining the atmospheric shell structure.

Whether the atmospheric temperature decreases, increases, or is isothermal with respect to altitude changes how that atmosphere impacts the incoming radiation. Atmospheric temperature profiles are undoubtedly not as simple as a straight increase or decrease with respect to altitude, as the temperature structure can contain both processes at differing altitudes (as seen by Earth's atmospheric temperature profile). As determining the temperature structure of exoplanet atmospheres is outside our current observational technological reach, the first theoretical studies, due to the complexity of atmospheric dynamics and chemistry, will likely detail individual case studies and not a statistical analysis across many exoplanets; thus, it will likely require decades of theoretical research and subsequent observations before we gain a full understanding of the different categories of atmospheric profiles.

Even though we have limited knowledge of planetary atmospheric structure, I still

must choose a representative atmospheric profile and pursue the theoretical modeling. Our understanding of Earth's atmosphere surpasses our understanding of other atmospheres and, thus, the Earth provides a viable starting point. For the current work, I have chosen to use the temperature and pressure profile of the Earth provided by the 1976 US standard atmosphere publication (NOAA, NASA, & USAF 1976). Examples of alternative temperature/pressure constructs that should be investigated in future modeling are detailed in Section 4.8.4.

2.1.5 Dissecting Optical Depth Part II

I began Section 2.1 by working with the radiative transfer equation until I demonstrated the importance of the optical depth, τ_ν. I then side-stepped into a partial analysis of τ_ν which demonstrated its dependence on altitude. From this dependence, I finished the derivation for the transmissivity radiative transfer spectrum [Eq. (2.11)]. I then took a slight detour to emphasize the importance of exploring the temperature/pressure parameter space for an atmosphere. I now transition my general focus back to τ_ν in order to finish the analysis of this key element. The second main parameter in solving for τ_ν in Eq. (2.9) is the molecular cross section

$$\sigma_{lu} = S_{lu} \cdot f(\tilde{\nu} - \tilde{\nu}_0), \tag{2.12}$$

where S_{lu} is the line intensity of the transition, $f(\tilde{\nu}-\tilde{\nu}_0)$ describes the line broadening profile for the transition, and the subscript "lu" references the transition between lower and upper energy levels (Seager 2010). It is here that I have to side step again. I must first introduce my data source in order to calculate S_{lu} (see Section 2.2), and I must introduce line broadening profiles in order to explain and evaluate $f(\tilde{\nu}-\tilde{\nu}_0)$ (see Section 2.3). By developing an understanding of the constituents of the line intensity and line broadening parameters, I explain the factors influencing σ_{lu}, thereby allowing for a full understanding of τ_ν and, correspondingly, the transmissivity spectrum.

2.2 Line Intensity and the HITRAN Database

Light, when absorbed by a molecule, causes the molecule to enter an excited state. Depending on the energy of the incident photon, the light could cause an electronic, a vibrational, and/or a rotational transition. A molecule can easily have millions of potential transitions thus allowing for interactions with a variety of photon energies.[1] Each molecular transition for every molecule has a corresponding line intensity, S_{lu}, that describes the strength of the transition. I begin the analysis of Eq. (2.12) through detailing the line intensity parameter S_{lu}. To evaluate the line intensity parameter for the HITRAN biosignature gases, I utilize molecular data from the HITRAN database[2] (Rothman et al. 1998; Rothman et al. 2009) which is operated by the Atomic and Molecular Physics Division at the Harvard-Smithsonian Center for Astrophysics. The HITRAN database provides the line strengths (i.e. line intensities) for molecular transitions of many molecules at the HITRAN reference temperature, T_{ref}, equal to 296 Kelvin. My modeled atmosphere, however, consists of many different temperatures than solely 296 Kelvin; thus, I must scale the S_{lu} provided by the HITRAN database such that I have proper line intensities (for every transition of every molecule) for each atmospheric temperature layer in my model. I can accomplish this goal by utilizing the following relation presented in Rothman et al. (1998) and Seager (2010):

$$S_{lu}(T) = S_{lu}(T_{ref}) \cdot \frac{Q(T_{ref})}{Q(T)} \cdot \frac{e^{-\frac{c_2 E_l}{T}}}{e^{-\frac{c_2 E_l}{T_{ref}}}} \cdot \frac{1 - e^{-\frac{c_2 \tilde{\nu}_{lu}}{T}}}{1 - e^{-\frac{c_2 \tilde{\nu}_{lu}}{T_{ref}}}}, \tag{2.13}$$

where $S_{lu}(T)$ designates the line intensity (for each transition $\tilde{\nu}_{lu}$) at the temperature denoted in the corresponding parentheses, T designates the temperature grid for which S_{lu} is being calculated, T_{ref} is the HITRAN reference temperature of 296 Kelvin, Q represents the molecular partition function of the corresponding temper-

[1] Water vapor is an example of a molecule with millions of transitions, which is one reason why water is such a good absorber with broad spectral features that can mask the spectral features of biosignature gases.

[2] Further information about the HITRAN database and how to gain access to the database can be found at http://www.cfa.harvard.edu/hitran.

ature values, $c_2 = \frac{hc}{k_b}$ (h equals Planck's constant, c equals the speed of light, and k_b equals Boltzmann's constant), E_l is the energy of the lower energy level of the transition, and $\tilde{\nu}_{lu}$ is the wavenumber of the transition where the subscripts l and u represent the lower and upper levels of the transition, respectively. In the current work, $S_{lu}(T)$ is actually a 2-dimensional matrix with each entry representing a particular S_{lu} for each given molecular transition (first dimension of array) and each temperature in my temperature grid (second dimension of array).

I will now dissect each term on the right hand side of Eq. (2.13). The first term on the right hand side of Eq. (2.13), $S_{lu}(T_{ref})$, is the HITRAN line intensity provided in the database at the reference temperature, T_{ref}, equal to 296 Kelvin. The second term on the right hand side of Eq. (2.13), the ratio of partition functions, $\frac{Q(T_{ref})}{Q(T)}$, introduces the factor that accounts for the change in the partition function that results from a change in temperature (i.e. $T_{ref} \longrightarrow T$; Seager 2010). The partition functions for most of the HITRAN molecules can be retrieved from the HITRAN database, and interpolation of the data will provide partition functions for any temperature grid with temperatures between 70 and 3000 Kelvin. The third term on the right hand side of Eq. (2.13), $\frac{e^{-\frac{c_2 E_l}{T}}}{e^{-\frac{c_2 E_l}{T_{ref}}}}$, adjusts for the change in Boltzmann populations that results from the temperature change $T_{ref} \longrightarrow T$ (Seager 2010). In the third term, c_2 and T_{ref} are constants, the lower energy level of each transition, E_l, is provided in the HITRAN database, and the researcher chooses the temperature grid T; therefore, the third factor in Eq. (2.13) is easily evaluated once a proper temperature grid is chosen. The last term on the right hand side of Eq. (2.13), $\frac{1-e^{-\frac{c_2 \tilde{\nu}_{lu}}{T}}}{1-e^{-\frac{c_2 \tilde{\nu}_{lu}}{T_{ref}}}}$, accounts for the difference in stimulated emission resulting from the change in temperature $T_{ref} \longrightarrow T$ (Seager 2010). The only new term in this ratio is the wavenumber, $\tilde{\nu}_{lu}$, which is provided by HITRAN as the wavenumber corresponding to $S_{lu}(T_{ref})$.

Given all of the aforementioned parameters, I am now able to calculate $S_{lu}(T)$. Upon combination of $S_{lu}(T)$ with the broadening profile, $f(\tilde{\nu} - \tilde{\nu}_0)$, as shown in Eq. (2.12), I can calculate molecular cross sections that are representative of each atmospheric layer. Before turning to the discussion of the broadening profile, $f(\tilde{\nu}-\tilde{\nu}_0)$, I want to emphasize the importance of the HITRAN database and other such catalogs.

The HITRAN database has undergone many revisions/additions over the years, each making substantial improvements over previous editions. The future inclusion of additional molecular transitions and the integration of additional molecules into the database provides for a better understanding of the molecules in question and further expansion of studies utilizing the HITRAN data. The number of current and potential research opportunities involving the use of HITRAN-like data are numerous. In order for those studies to accurately represent the modeled scenarios, the researchers must have quality molecular data from quality databases; therefore, it is imperative that the scientific community advocates for funding both the databases and the research that strengthens them.

2.3 Broadening Profile

2.3.1 Natural, Doppler, Lorentz, and Voigt Broadening: Which One is the Proper Choice?

With the description of the line intensity, S_{lu}, presented above, I can now return to develop a better understanding of Eq. (2.12). If molecular (or atomic) transitions between energy levels were infinitely sharp in energy or frequency space (i.e. no broadening), then the molecular (or atomic) cross section would simply be $\sigma_{lu} = S_{lu}$ and the calculations would simplify greatly. However, an incident photon need not carry the classically-described "exact" amount of energy, E, necessary to cause the energy level transition as long as the photon is carrying an energy "close enough" to that of the transition. The flexibility in energy absorption demonstrates that there exists a spread of energies that can cause each particular transition. The energy spreading is termed natural line broadening and is a direct result of quantum mechanical effects and the Heisenberg Uncertainty Principle. Since the quantum mechanical effects prevent infinite sharpness, I must include the broadening profile $f(\tilde{\nu} - \tilde{\nu}_0)$ in Eq. (2.12) to properly describe the molecular absorption cross section.

For planetary atmospheres, natural broadening does not cause a dominant im-

pact (as compared to other broadening mechanisms) on the molecular cross sections and, thus, can be neglected (Seager 2010). However, three other broadening profiles (Doppler, Lorentz, and a combined Doppler/Lorentz profile called a Voigt profile) have a potentially larger impact than natural broadening and, thus, must be investigated. Doppler broadening describes the line broadening that occurs due to the thermal motion of molecules. For Doppler broadening, as the molecule de-excites by releasing a photon, that photon is either red-shifted or blue-shifted in wavelength as a result of the emitting molecule moving away from or towards the observer, respectively. If the emitting molecule is not moving away or towards the observer, then the emitted photon has a wavelength value within that of the natural broadening. This red/blue-shifting broadens the spectral line (wider than natural broadening) and is calculated by the Doppler broadening profile.

Lorentz broadening describes the line broadening that occurs due to the collisions between molecules. For Lorentz broadening, the intermolecular forces between two particles near collision change the energy levels of the particles. By shifting these energy levels, the intermolecular forces cause the emitting particle to release a photon at a different frequency, thus causing a broadening in the spectral line (Liou 2002).

A Voigt profile takes into account both the Doppler and Lorentz broadening effects. Even though introducing a Voigt profile would "cover all the bases" in terms of proper broadening profiles, as radiative transfer calculations can be quite computationally taxing, if either Doppler or Lorentz broadening clearly dominates over the other, then introducing the complexity of a Voigt profile does not provide advantages to the research and may increase the run time of the models.

One way to compare Doppler and Lorentz broadening is through the analysis of the full width at half maximum (FWHM) for each broadening profile. The FWHM of a spectral line is the width of the spectral line at a value equal to half of its maximum. By comparing the FWHMs resulting from Doppler and Lorentz broadening, I can determine if one broadening mechanism dominates over the other. Upon running Doppler and Lorentz broadening tests for carbon monoxide, it was noticed that the FWHM of the Lorentz broadening was orders of magnitude greater than that of

Doppler broadening. These results, as anticipated, demonstrated that I could neglect Doppler broadening (and, hence, neglect the Voigt profile) and continue solely with the Lorentz broadening profile for $f(\tilde{\nu} - \tilde{\nu}_0)$ in Eq. (2.12) (see also Liou 2002).

It must be noted that the simplification made above may not be fully justified in all atmospheric settings. The comparative effects between Doppler and Lorentz profiles are dependent on altitude (i.e. the temperature/pressure structure of the atmosphere), thus, it is possible that they may take turns dominating over each other in differing atmospheric layers. I have chosen to continue solely with a Lorentz broadening description (as opposed to incorporating a Voigt profile) since the number density of particles, especially in the lower atmosphere, is large enough such that the broadening due to molecular collisions dominates over the broadening due to molecular thermal motions. Furthermore, the lower sections of the atmosphere is also where the majority of the observable absorption occurs, as the number densities of particles are too low to create strong signals at higher altitudes in the atmosphere (for an Earth-like planet).

2.3.2 Lorentz Broadening Profile

To calculate the Lorentz broadening profile for each molecular transition, I use the equation given in Rothman et al. (1998), namely:

$$f(\tilde{\nu} - \tilde{\nu}_0) = \frac{1}{\pi} \frac{\gamma(P,T)}{\gamma(P,T)^2 + [\tilde{\nu} - (\tilde{\nu}_0 + \delta(P_{ref}, T_{ref}) \cdot P)]^2}, \tag{2.14}$$

where π has its standard definition, $\gamma(P,T)$ is the half width of the line at half maximum [see Eq. (2.15)], $\tilde{\nu}$ is the wavenumber for which the broadened intensity is being calculated, $\tilde{\nu}_0$ is the wavenumber corresponding to the ideal, non-broadened line strength S_{lu}, $\delta(P_{ref}, T_{ref})$ is the air-broadened pressure shift (provided by the HITRAN database) at the HITRAN reference pressure ($P_{ref} = 1$ atmosphere) and reference temperature ($T_{ref} = 296$ Kelvin), P designates the atmospheric pressure, and T designates the atmospheric temperature. Note that the pressure, P, and the temperature, T, are both vectors corresponding to the different atmospheric layers.

Before diving into the parameters of Eq. (2.14), I must describe how the broadening parameter, $f(\tilde{\nu} - \tilde{\nu}_0)$, interacts with the line intensity, S_{lu}, in calculating the cross sections given by Eq. (2.12). The line strength, S_{lu}, of every transition is retrieved from Eq. (2.13) (for varying temperatures) for every idealized HITRAN wavenumber $\tilde{\nu}_0$. This same "strength" is then broadened over the wavenumber range chosen using Eq. (2.14) such that, if one integrates the line intensity over the entire broadening profile, then the value of S_{lu} is returned. Conceptually, it can be viewed that the strength of the line is spread over the designated, broadened wavenumber interval. In this manner, the line strength at the center of the broadened line (i.e. at $\tilde{\nu}_0$) is less than that of an ideal (non-broadened) line.

The wavenumber interval over which to broaden each line intensity can be chosen by the researcher. One possibility is to calculate the broadened line intensity contribution of each HITRAN transition for every value in the researchers wavenumber grid; however, this technique is very computationally expensive and not necessary. Instead, one can determine a cut-off point (at some wavenumber distance away from the line center) at which the broadened intensity does not contribute significantly to the overall intensity and, thus, can be neglected. The FWHM of each line provides the perfect reference for determining how wide to calculate the broadening. For a conservative approach, I have chosen to calculate the broadening profiles out to one hundred times the FWHM on each side of the line center. By doing such, the corresponding cross sections on the wings of the broadening profile are orders of magnitude lower than that at the center. At that distance in the wings of the profile, the broadening contributions are so minute that the strengths of other line centers easily dominate in those regions; therefore, the contributions further out than one hundred times the FWHM can be neglected. If the line centers of different transitions are spaced farther apart than one hundred times the FWHM of the lines, I assume that the broadening of each line center does not contribute to its neighbors profile. I note that the wavenumber range of one hundred times the FWHM (on each side) of each transition may calculate the broadening further out than is necessary, but I am able to incorporate this conservative approach without any significant increase in computational

time and resources.

I will now begin dissecting Eq. (2.14). The half width at half maximum, $\gamma(P,T) = \frac{1}{2} \cdot FWHM$, given in Eq. (2.14) is dependent on both temperature and pressure and, thus, must be scaled for each layer of the modeled atmosphere. Rothman et al. (1998) provide this scaling relation through

$$\gamma(P,T) = \left(\frac{T_{ref}}{T}\right)^n [\gamma_{air}(P_{ref},T_{ref})(P-p_s) + \gamma_{self}(P_{ref},T_{ref})p_s], \tag{2.15}$$

where T_{ref} is the HITRAN reference temperature (296 Kelvin), P_{ref} is the HITRAN reference pressure (1 atmosphere), T is the temperature of the corresponding atmospheric layer, n is the coefficient of temperature dependence on the air-broadened half width [provided by the HITRAN database and satisfies the equation $\gamma_{air}(P_{ref},T) = \gamma_{air}(P_{ref},T_{ref}) \cdot (\frac{T_{ref}}{T})^n$], $\gamma_{air}(P_{ref},T_{ref})$ is the air-broadened half width at half maximum (provided by the HITRAN database), P is the pressure of the corresponding atmospheric layer, p_s is the partial pressure of the gas species in the corresponding atmospheric layer, and $\gamma_{self}(P_{ref},T_{ref})$ is the self-broadened half width at half maximum (provided by the HITRAN database) (Rothman et al. 1998).

For Eq. (2.15), as indicated above, T_{ref}, n, $\gamma_{air}(P_{ref},T_{ref})$, and $\gamma_{self}(P_{ref},T_{ref})$ are provided by the HITRAN database. The only parameters not provided by the HITRAN database are the temperature/pressure structure of the atmosphere along with the partial pressure, p_s, of the gas in question. Details concerning atmospheric temperature and pressure profiles were discussed in Section 2.1.4. Choosing a partial pressure (with altitude dependence) for an atmospheric species can be tricky for several reasons. The first aspect is that, through our current general understanding of atmospheres (which is very limited), there is no wrong choice for p_s, though some choices may be more realistic than others. The difficulty involved with choosing a proper partial pressure derives mostly from the fact that we really only have one atmosphere (Earth's) that we semi-understand. Even our current, best understanding of the inner working of Earth's atmosphere still contains large holes, which is why atmospheric research is such an active area. The only other terrestrial planet atmo-

spheric examples are Mars and Venus, but, without probes continuously sampling their atmospheres (especially the atmosphere of Venus), our understanding is very restricted.[3] We do have the gas giants, Jupiter and Saturn, but it appears that their atmospheric dynamics and chemistry are much more complicated than that of Earth. Untangling these complications is an active area of research that, once understood, will help elucidate the many secrets governing atmospheric structure, chemistry, and dynamics. Unfortunately, the current stage of atmospheric research (both terrestrial and gas giant) is still in its youth and has not yet provided a unifying picture for the varying types of exoplanetary atmospheres.

Transferring back to our best understood atmosphere (Earth's), finding altitude-dependent partial pressures for gases in Earth's atmosphere is increasingly difficult, and, for most gases, partial pressure data do not exist for all atmospheric altitudes. Some of the gases only have surface measurements; therefore, good constraints on how the surface values scale with atmospheric height do not exist. The situation simplifies for gases that are evenly mixed throughout the atmosphere (e.g., carbon dioxide on the Earth), but then one can raise the question: "To what altitude are the gases evenly mixed?". In many cases, the researcher has to use his or her experience and expertise to answer this question and to best estimate how the partial pressure of other gases behave over the entire modeled atmosphere.

By only partially understanding the atmosphere of one habitable planet, we cannot expect to fully visualize all possible flavors of habitable planet atmospheric compositions; therefore, the parameter space for p_s is extraordinarily large. For first round studies, as long as the choice of p_s can be justified on some level, the corresponding research will add to our general understanding of atmospheres. For future studies, as we develop technology that provides the ability to resolve the atmospheres of exoplanets, we will be able to use the observations to constrain our theoretical models for better physical descriptions of the varying types of atmospheres. Through exoplanet atmospheric analyses, we will hopefully be able to develop a catalog of planetary

[3]Mercury essentially does not have an atmosphere, though it may contain small abundances of argon.

atmospheres with the optimism that the sheer numbers of exoplanet atmospheric examples will aid us in developing a better understanding of atmospheric formation, dynamics, chemistry, interaction with internal processes of the planet, etc.

A valuable technique for incorporating the chosen partial pressure for each gas is to utilize the mixing ratio parameter (a measure of atmospheric abundance) that relates the partial pressure to the total atmospheric pressure. The mixing ratio parameter will also be used to connect the number density of the gaseous species, $n_s(r)$, with the total atmospheric number density, $n(r)$. The relations comparing the gaseous partial pressure to the total atmospheric pressure and the number density of the gaseous species to the total number density of particles in the atmosphere are

$$p_s(r) = \zeta(r) \cdot P(r) \tag{2.16}$$

and

$$n_s(r) = \zeta(r) \cdot n(r), \tag{2.17}$$

where $p_s(r)$ is the partial pressure of the gas species, $\zeta(r)$ is the mixing ratio for the gas, $P(r)$ is the total pressure of the atmospheric layer, $n_s(r)$ is the number density of the gas species, and $n(r)$ is the number density of the atmospheric layer given by $n(r) = \frac{P(r)}{k_b T(r)}$ [$P(r)$ is the pressure of the atmospheric layer, k_b is the Boltzmann constant, and $T(r)$ is the temperature of the atmospheric layer]. With the addition of the partial number density of a gas to the analysis, the $n(r) \longrightarrow n_s(r)$ in Eq. (2.9) for each individual biosignature gas. After choosing a temperature/pressure grid, the only unknown parameter left for calculating Eqs. (2.16) and (2.17) is the mixing ratio, $\zeta(r)$.

The earlier discussion that pertained to the large parameter space for partial pressure ultimately results from the large parameter space for the altitude dependent mixing ratio. Mixing ratios can be constant with altitude (e.g., carbon dioxide on the Earth) or could vary with altitude (e.g., ozone on the Earth). If the mixing ratio varies with altitude, it does not necessarily need to follow a straight increase or decrease. The mixing ratio may actually follow a more complicated profile due to

the specific atmospheric dynamics and chemistry of the planet. For my work, since I am modeling the Earth's atmosphere, I used Earth-based mixing ratios (see Section 2.6.2 for further details).

As shown above, I can use the mixing ratio to calculate the partial pressure required for Eq. (2.15) (which leads to the calculation of the molecular cross section) and the number density required for Eq. (2.9) (which leads to the calculation of the transmissivity spectrum). An ideal study would incorporate the mixing ratio coupling between the molecular cross section and transmissivity calculations [i.e. use the same mixing ratio, $\zeta(r)$, for both Eqs. (2.15) and (2.9)]. If an "ideal" study changes the mixing ratio of the gas, then new molecular cross sections must be calculated before transmissivity spectrum calculations can proceed. Depending on the resolution of the wavenumber grid chosen, the width of the Lorentz broadening profile incorporated, and the number of molecular line transitions, the cross section calculations can become quite computationally expensive.[4] I can avoid constantly recalculating the molecular cross sections for every change in mixing ratio because such changes do not dramatically affect the absorption cross section results. Therefore, I choose one altitude-dependent mixing ratio for each molecule for the absorption cross section calculations (see Section 2.6.2) and then use those absorption cross sections for the varying transmissivity spectrum models.

With the theory developed thus far, I can now calculate a perfect transmissivity spectrum (i.e. no synthetic noise and no wavelength binning) by proceeding through the following steps. With a chosen mixing ratio and atmospheric pressure profile, I can calculate the partial pressure of the atmospheric gas. By combining the partial pressure with the temperature and pressure profile of the chosen atmosphere, I can calculate the half width at half maximum given by Eq. (2.15). From there, given a wavenumber grid, the wavenumbers for the HITRAN transitions, and the

[4]Ozone has over 400,000 HITRAN line transitions. For the properties chosen in my model (860 atmospheric layers, Lorentz broadening out to one hundred times the FWHM on each side, etc.), these 400,000 HITRAN transitions require billions of calculations. The sheer number of the required calculations is what causes the cross section calculations to require significant amounts of computational time in some cases. I aim to avoid this endeavor and describe my approach further in the text after this footnote.

air-broadened pressure shift of each transition, I can calculate the broadening profile $f(\tilde{\nu} - \tilde{\nu}_0)$ through Eq. (2.14). I can then combine the broadening profile of Eq. (2.14) with the line strengths calculated from Eq. (2.13) to solve for the molecular cross sections designated by Eq. (2.12). I then use the molecular cross sections and, given a proper $n(r)$, evaluate the height dependent optical depth via Eq. (2.9). Finally, I plug the optical depth into Eq. (2.10) and the subsequent result into Eq. (2.11) in order to obtain my goal, the transmissivity spectrum representative of all input parameters.

2.4 Simulated Noise

Following the above formulation provides for the calculation of clean, theoretical transmissivity spectra; however, "perfect" spectra are never observed due to observational noise. Contributors to the noise budget can include an atmospheric component (from the Earth's atmosphere if utilizing ground observations), systematics, photon noise, etc. In this study, I model within 20% of the photon noise, but have not considered any other noise sources. The following derivation describes how to link the theoretical transmissivity radiative transfer calculations to the corresponding photon noise which depends on the blackbody emission from the host star, the telescope aperture size, the observational time, the distance to the target, and the stellar radius. The main parameter required for determining the photon noise is the number of photons observed; therefore, the goal of the following calculation is to determine how many photons are received at each wavelength of interest. The steps of the derivation follow below.

The amount of absorption that can occur in any spectral band of an atmospheric gas is partially dependent on the wavelength-dependent incident radiation. For my study, I model the incident stellar radiation as a blackbody given by

$$B_\lambda(T) = \frac{2hc^2}{\lambda^5} \frac{1}{e^{\frac{hc}{\lambda k_b T}} - 1}, \tag{2.18}$$

where $B_\lambda(T)$ is the blackbody radiation in units of $\frac{\mathrm{J}}{\mathrm{m}\cdot\mathrm{m}^2\cdot\mathrm{s}\cdot\mathrm{sr}}$, h is Planck's constant, c is the speed of light, λ is the wavelength of interest, k_b is Boltzmann's constant, and T is the temperature. One aspect to note about the units of $B_\lambda(T)$ is that the "m" unit in the denominator refers to the wavelength or spectral band of interest while the "m^2" refers to the square area of the emitting body. This difference is why they are not combined into m^3. In many studies, the m is given in alternate units such as nanometers or angstroms to avoid any confusion; therefore, while utilizing the blackbody formula, make sure to use consistent units throughout the following calculations regardless of what exact units are chosen.

One way to determine how to transition from the blackbody equation to the number of photons observed at each wavelength is to analyze the units as presented above. The energy unit, Joules, in $B_\lambda(T)$ provides the pathway to calculate the number of photons observed at each wavelength; however, I cannot transition straight to the number of photons until I account for the other parameters (or units) in $B_\lambda(T)$. Since all of the other parameters are located in the denominator of Eq. (2.18), I will be multiplying $B_\lambda(T)$ by each of the following factors (described below) in order to calculate the total amount of energy received in a given observational period with given instrument specifications.

The first parameter to account for is each wavelength bin of the observation. A telescope does not observe at discrete wavelengths, but rather retrieves a flux value for a range of wavelengths defined by each wavelength bin. Multiplying $B_\lambda(T)$ by the width of each wavelength bin accounts for the m in the units of $B_\lambda(T)$. I define the edges of the wavelength bins as the midpoints between each point in my wavelength grid (see Section 2.5 for an explanation of the wavelength grid chosen for this analysis). I then use the distance between these midpoints (where the wavelength of interest is essentially at the center between them) as the width, w_λ, of wavelength bin. Since I do not use a constant wavelength spacing in my wavelength grid (see Section 2.5 for details), the width of the wavelength bands is wavelength dependent.

The next parameter to account for is the m^2 in the denominator of Eq. (2.18). The m^2 parameter describes the unit area on the star from which the energy is released.

Since I take into account radiation released from the entire stellar surface that faces the exoplanet (as opposed to just 1 m^2), I multiply $B_\lambda(T)$ by the disk area of the star, $A_{star} = \pi R_{star}^2$. My model star is a Sun-like star, and, thus, I choose $R_{star} = R_{Sun}$.

The unit of time in the denominator of Eq. (2.18) shows that the blackbody formula calculates the energy released per unit time. In order to account for how long the telescope observes the target, I multiply $B_\lambda(T)$ by the observation time, Δt. For most of my models (unless otherwise indicated), I use an observation time equivalent to 100 hours.

The last parameter to account for in calculating the total energy received in an observation is the solid angle [i.e. the steradian unit of $B_\lambda(T)$] over which the observation occurs. The solid angle is calculated by $\psi = \frac{\pi r_{detector}^2}{d^2}$, where $r_{detector}$ is the radius of the observing telescope and d is the distance to the target.

Putting all four of these parameters together, I calculate the total energy received by the detector as

$$E_{total} = B_\lambda(T) \cdot w_\lambda \cdot A_{star} \cdot \Delta t \cdot \psi. \tag{2.19}$$

I now convert the total energy received into the number of photons impacting the detector through

$$n_\lambda = \frac{E_{total}\lambda}{hc}. \tag{2.20}$$

Note that the number of photons calculated by Eq. (2.20) is wavelength dependent, and, thus, there will be a value for every wavelength in the wavelength grid.

It is at this point that I can now calculate the synthetic noise imposed on the models. The impact of photon noise falls off as $\frac{1}{\sqrt{n_\lambda}}$, where n_λ is the number of photons at each wavelength [given by Eq. (2.20)]. The photon noise relation shows that the larger the number of incident photons, the smaller the corresponding photon noise. This effect is a physical property of photon (i.e. poisson) noise. For my particular models, I am modeling within 20% of the photon noise, thus my total noise budget is given by

$$\Sigma(\lambda) = 1.2 \cdot \frac{1}{\sqrt{n_\lambda}}. \tag{2.21}$$

I must now relate the noise [$\Sigma(\lambda)$] given in Eq. (2.21) to the resultant noise on

the transmissivity spectrum which is denoted as $\Sigma_{transmissivity}(\lambda)$. $\Sigma(\lambda)$ is related to $\Sigma_{transmissivity}(\lambda)$ by

$$\Sigma_{transmissivity}(\lambda) = \frac{\Sigma(\lambda) R_{star}^2}{2 R_{surface} H}, \tag{2.22}$$

where R_{star} is the radius of the host star, $R_{surface}$ is the distance from the center of the exoplanet to the exoplanet surface, and H is the total atmospheric height. H is measured from the surface of the planet and not from the center of the planet. The following equation relates the "noisy" transmissivity spectrum, $T_{noise}(\lambda)$, to the clean transmissivity spectrum, $T_{clean}(\lambda)$:

$$T_{noise}(\lambda) = T_{clean}(\lambda) \pm \Sigma_{transmissivity}(\lambda) \cdot \alpha, \tag{2.23}$$

where α is a gaussian distribution with a standard deviation equal to one. The multiplication between $\Sigma_{transmissivity}(\lambda)$ and α is required to move the standard deviation of the distribution to equal $\Sigma_{transmissivity}(\lambda)$. Now that I have calculated the synthetic noise, I can utilize Eq. (2.23) to calculate the transmissivity spectrum with synthetic noise included that has its base in observational parameters (telescope aperture, distance to target, etc.).

2.5 Modeled Spectral Regions and Binning Resolution

2.5.1 Wavelength Grid

Since spectroscopic data is usually binned in wavelength or wavenumber space, I must also bin my transmissivity data accordingly in order to more closely model spectra that could be observed in the coming years. Before describing the chosen bin structure, I must first discuss the wavenumber/wavelength grid (hereafter, grid, unless otherwise noted) chosen for my trials. I determined the endpoints of my grid based on the wavenumber range of the transitions of the different molecules in the HITRAN database such that I could utilize the same grid for every molecule. Using

the same wavelength grid for all HITRAN molecules provides for the easy combination of multiple molecules within the same transmissivity calculations. I chose a very wide wavenumber range ($1 - 29{,}000$ cm^{-1}) for the calculations in order to investigate non-traditional wavelength regions. In addition, as more transitions at other wavelengths for the biosignature gases become published, my large grid will accommodate their inclusion into the analysis.

Since my wavenumber range ($1 - 29000$ cm^{-1}) spans many orders of magnitude, it is too computationally expensive to have constant wavenumber spacing in the grid. In fact, constant grid spacing over such a large range is not realistic. For example, if one chooses a grid spacing of ten nanometers, then this decision is quite useful in the visible portion of the spectrum while, at the same time, huge overkill elsewhere (e.g., at millimeter wavelengths). Similarly, a constant spacing chosen with the millimeter range in mind would work excellent there, but find itself too coarse in the visible or infrared regions. In addition, depending on how many layers one includes in the modeled atmosphere, too fine of a grid could cause out-of-memory computational errors by requiring too much memory storage during absorption cross section calculations.

In order to get a (non-constant) spacing for my wavenumber grid that resolves individual spectral lines, I utilized the property of resolving power given by

$$RP = \frac{\nu}{\Delta\nu} = \frac{\nu_i}{\nu_{i+1} - \nu_i}, \tag{2.24}$$

where RP designates resolving power, ν_i denotes a wavenumber point in the grid, and $\Delta\nu$ denotes the difference between adjacent grid points ν_{i+1} and ν_i. In order to build a grid, one can choose a constant resolving power and rearrange Eq. (2.24) such that

$$\nu_{i+1} = \nu_i + \frac{\nu_i}{RP}. \tag{2.25}$$

In Eq. (2.25), it is noticed that the resolving power can be varied to get the resolution desired for the trials.

Before binning the data, I transferred my wavenumber grid into a wavelength grid

by utilizing the relation

$$\lambda(nm) = \frac{10,000,000}{\nu(cm^{-1})}. \tag{2.26}$$

where λ represents wavelength (in nm) and ν represents wavenumber (in cm^{-1}). After changing units, it is noticeable that, due to the enormous range of the grid (340 nanometers $-$ 0.01 meters), binning with a constant bin size for the entire region is not effective. In order to use constant bin sizes, I separate the wavelength grid into five distinct regions: (1) Visible, (2) Infrared (IR), (3) Sub-millimeter (sub-mm), (4) Far-Infrared (far-IR), and (5) Millimeter (mm). These regions correspond to 340 nm $-$ 1000 nm, 1 μm $-$ 10 μm, 10 μm $-$ 100 μm, 0.1 mm $-$ 1 mm, and 1 mm $-$ 10 mm, respectively. The corresponding constant bin sizes are 10 nm, 0.1 μm, 1 μm, 0.01 mm, and 0.1 mm, respectively.

2.5.2 Monte Carlo Noise Propagation Method in Reference to Wavelength Binning

The synthetic noise introduced in Section 2.4 is applied to each transmissivity value in the wavelength grid. The transmissivity data (with noise included) then undergoes a wavelength binning process; thus, the input noise must be properly propagated through the binning process. Two different techniques provide a solution to the noise propagation: (1) analytical propagation and (2) a Monte Carlo method. The calculations used to bin the data are complex enough that analytical propagation is not a feasible opportunity; however, a Monte Carlo error propagation is an accurate and easily accessible alternative.

I incorporate the Monte Carlo error propagation method through the Gaussian distribution, α, in Eq. (2.23). I model thousands of α's and thereby calculate thousands of "noisy" transmissivity spectra via Eq. (2.23). I then bin each of the "noisy" transmissivity spectra in wavelength space. From the thousands of binned spectra, the median transmissivity value is retrieved for each wavelength and called $T_{median}(\lambda)$. The standard deviation of the thousands of "noisy" transmissivity values is the propagated 1σ error [called $\sigma_{binned}(\lambda)$]. The desired, wavelength-binned transmissivity

[called $T_{plotted}(\lambda)$] is the median transmissivity [$T_{median}(\lambda)$] perturbed by the noise from each bin [$\sigma_{binned}(\lambda)$], namely

$$T_{plotted}(\lambda) = T_{median}(\lambda) \pm \sigma_{binned}(\lambda) \cdot \beta, \tag{2.27}$$

where β is a Gaussian distribution. The 1σ error for $T_{plotted}(\lambda)$ is $\sigma_{binned}(\lambda)$. Note that for a large enough number of α trials using Eq. (2.23), $T_{median}(\lambda)$ is equivalent to a wavelength binned $T_{clean}(\lambda)$. In this work, the wavelength-binned transmissivity plots that include noise are representative of Eq. (2.27).

2.6 Model Parameters

In the previous sections, I have described how to calculate transmissivity spectra while paying strict attention to describing many intricacies not discussed in standard texts. The upcoming sections detail my model parameters and input data. The motivation for my work can be found in Section 1.5.

2.6.1 Atmospheric Temperature/Pressure Profile

I use the temperature and pressure profile of the Earth's atmosphere provided by the 1976 US standard atmosphere publication (NOAA, NASA, & USAF 1976). The radius of the modeled planet is equal to the Earth's radius, and my atmosphere extends from the surface to an altitude of 86 kilometers. I divide the atmosphere into 860 concentric shells of 100 meters width (measured in the radial direction). To best average the temperature and pressure over each layer, I interpolate for the values of temperature and pressure in the center of the layer and then use those values to calculate the number density of molecules for the entire layer. The current state of observational technology cannot provide such a detailed of temperature/pressure resolution of an exoplanet; therefore, alternative models may prefer a more coarse atmospheric structure.

2.6.2 Mixing Ratios

I have previously discussed the difficulty that arises in choosing mixing ratios for the cross section and transmissivity calculations (see Section 2.3.2). I further the discussion here. For many molecular species, mixing ratios as a function of altitude for the Earth's atmosphere do not exist. In order to include such gases in transmissivity radiative transfer studies, I must estimate their mixing ratios using reasonable assumptions. In my experience, varying the mixing ratio in the absorption cross section calculations does not affect the resultant absorption cross sections significantly, even if the mixing ratios change by orders of magnitude in some cases. The apparent lack of strong impact is due to the relations between the self/air-broadening half-widths and the partial pressure of the gas as listed in Eq. (2.15). For molecules that are not a major constituent of the atmosphere, the partial pressure is small enough that it can be assumed to equal zero in Eq. (2.15). A caveat exists with setting the partial pressure equal to zero; namely, if the self-broadening half-width for the molecule is relatively large compared to the air-broadening half-width for the molecule, then setting the partial pressure equal to zero in the absorption cross section calculations is not a proper choice. As previously mentioned, changing the mixing ratio has a much more dramatic effect in the transmissivity calculations. In fact, varying the mixing ratio (and thus the atmospheric abundance) in the transmissivity radiative transfer analysis is the corner stone of how I determine threshold atmospheric mixing ratios required for the detection of each HITRAN biosignature gas in the modeled exoplanet atmosphere.

Table 2.1 lists the fractional volumes (i.e. volume mixing ratios) or the partial pressures chosen for the HITRAN biosignature gases for the absorption cross section calculations. Oxygen is given a mixing ratio (constant for all altitudes) equal to Earth's value, methane is assumed to be well mixed with a fractional volume equal to 2.0×10^{-6} (NOAA, NASA, & USAF 1976), and the trace gases, as described above, are given a partial pressure equal to zero. Since the 1976 US standard atmosphere publication included altitude dependent mass mixing ratio data for ozone (NOAA,

NASA, & USAF 1976), I can calculate altitude dependent partial pressures for ozone directly from Eq. (2.16). The provided mass mixing ratio data for ozone represented altitudes between 2,000 − 74,000 meters in 2,000 meter increments. Unfortunately, the publication did not include mass mixing ratios for altitudes between 0 − 2,000 meters and 74,000 − 86,000 meters. In order to have ozone mass mixing ratios between 0 − 2,000 meters, I assumed well-mixed ozone in the lower atmosphere such that the mass mixing ratio between 0 and 2,000 meters is always that of the 2,000 meter value. For altitudes above 74,000 meters, I analyzed how the mass mixing ratio decreased with increasing altitude in the published data. Through my analysis, I chose to set the mass mixing ratio at 86,000 meters equal to 1.0 x 10^{-7} and have the mixing ratio decrease in even increments from its value at 74,000 meters to that chosen for 86,000 meters. I interpolated within this distribution to retrieve mass mixing ratios in the 100 meter increments required for my atmospheric layer model. Note that the mixing ratios given in NOAA, NASA, & USAF (1976) are mass mixing ratios.[5] My models and the equations presented in this work require volume mixing ratios. To convert between the two ratios, utilize the following relation:

$$Mass\ Mixing\ Ratio(r) = \zeta(r) \cdot \frac{Molar\ Mass\ of\ gas\ species}{Molar\ mass\ of\ air\ without\ gas\ species}, \quad (2.28)$$

where $\zeta(r)$ is the volume mixing ratio.

2.6.3 HITRAN Data

For the derivations presented earlier in this chapter, the data retrieved from the HITRAN database are transition dependent and are as follows: wavenumber, $\tilde{\nu}_0$; line strength, $S_{lu}(T_{ref})$; air-broadened half-width, γ_{air}; self-broadened half-width, γ_{self}; lower energy level, E_l, of the transition; the coefficient of temperature dependence of the air-broadened half width, n; and the air-broadened pressure shift, $\delta(P_{ref}, T_{ref})$. The partition functions for the molecules were also obtained from the

[5]The mixing ratios provided by NOAA, NASA, & USAF (1976) are the only mass mixing ratios in my work. It should be assumed (unless otherwise noted) that all other uses of the words mixing ratio refer to volume mixing ratio.

Table 2.1: Fractional Volumes/Partial Pressures used for the Molecular Absorption Cross Section Calculations for the HITRAN Biosignature Gases

Molecule	Fractional volumes (FV) or Partial Pressure (p_s)
O_2	FV=0.209476 (all altitudes)
O_3	See Table 18 in NOAA, NASA, & USAF (1976) and description in Section 2.6.2.
CH_4	FV=2.0 x 10^{-6}
N_2O	p_s=0.0 (all altitudes)
CH_3Br	p_s=0.0 (all altitudes)
CH_3Cl	p_s=0.0 (all altitudes)
H_2S	p_s=0.0 (all altitudes)
OCS	p_s=0.0 (all altitudes)
PH_3	p_s=0.0 (all altitudes)
SO_2	p_s=0.0 (all altitudes)

HITRAN database.

There have been many updates to the HITRAN database since its original publication. For my models, I have used the HITRAN 2008 database to retrieve the above data for CH_4, N_2O, CH_3Br, H_2S, and PH_3. Since the publication of the 2008 database, there have been updates/corrections to several molecules. I have used any updates that were available as of June 2012. The molecules from which I retrieved updated parameters are O_2, O_3, CH_3Cl, OCS, SO_2, and H_2O.[6]

2.6.4 Observational Properties

I model an Earth temperature/pressure atmosphere (as described in Sec. 2.6.1) on an Earth-size planet revolving around a Sun-like star. The distance to the target is 35.45 parsecs and the observation time is 100 hours (unless otherwise indicated). I model many telescope aperture sizes and detail those effects in Section 3.1. The noise budget is modeled to be within 20 percent of the photon noise as described in Section 2.4.

[6]The HITRAN 2008 database can be accessed by following the instructions located on http://www.cfa.harvard.edu/hitran/. The data for the updated molecules can be found on the "HITRAN updates" tab on that website.

2.6.5 Modeled Atmospheric Abundances

In each of my models, I use an Earth-like temperature and pressure atmospheric profile (as described in Section 2.6.1) and the ideal gas law to calculate the altitude-dependent number density of particles (denoted as N_{alt} in this subsection). In the remainder of my work, I describe each of my models as representing certain abundances of particular atmospheric gases using the N_{alt} of Earth as a reference. The modeled atmospheric gas abundances are either listed as atmospheric percentages or as volume mixing ratios. In either case, they describe the atmospheric proportion of the particular atmospheric species in reference to the N_{alt} of Earth. In many of my models, the combined number density of all modeled atmospheric species is less than the N_{alt} from the reference Earth. In these cases, the remaining constituents in the atmosphere are assumed not to contribute to the transmissivity spectra. Using this assumption, I can isolate the absorption from each modeled gas in order to study the gases individually. As will be described in Section 3.4, I include a 1% water constituent in the majority of my modeled atmospheres in order to analyze water's potential spectral masking of other atmospheric species. The models that contain 100% of an atmospheric species along with a 1% water component technically have a larger number of particles in their atmospheres ($1.01 \cdot N_{alt}$) than the reference Earth ($1 \cdot N_{alt}$). In these cases, I am basically modeling a slightly larger atmosphere than that of Earth. The overall reasoning for using the Earth as a reference point for the descriptions of the models is to provide a comparison platform between the modeled atmosphere and the Earth's current atmosphere.

2.7 HITRAN Database: Wavelengths of Molecular Absorption

The results presented in Chapter 3 and the HITRAN biosignature gas discussion that follows in Chapter 4 are strictly dependent on the input data from the HITRAN database. If molecular transition data do not exist in certain wavelength ranges (as is

the case for many molecules), then I cannot exclusively determine if the molecule can be detected in the "no-data" regions. Therefore, I only conclude on the detectability of a molecule at wavelengths where transition data exists.

The best way to demonstrate the wavelength domains where the HITRAN database has transition data for each molecule is to plot the clean (no synthetic noise, no data binning) transmissivity spectrum for each molecule. Whenever the transmissivity value equals unity that means that the molecule may not absorb in those regions. These "non-absorbing" regions either mean that the molecule does not actually have absorptions in that region or that the molecular absorptions are not yet included in the HITRAN database. Determining between the two possibilities above is beyond the scope of this manuscipt. Since I do not have the means to fill in "data-less" regions myself, I must push forth with the existing data. Figure 2-4 demonstrates the absorption features for each molecule.

One quick note about Fig. 2-4: Since the point of these figures is to demonstrate where (in wavelength space) the molecules absorb, they simulate the transmissivity profile that would result if the atmosphere of the planet consisted of 100 percent of the modeled gas and no other constituents. Natually, the strength of each feature would increase or decrease based on if the abundance in the model was increased or decreased, respectively; thus, the absorption strength in these plots is not the important aspect to focus on, but rather where (in wavelength space) the gases absorb is the main importance. The modeled atmosphere for all subfigures of Fig. 2-4 has an Earth-like temperature/pressure profile as described in Section 2.6.1.

As can be seen from Fig. 2-4, some gases have more published transition data than others. One interesting aspect is the absorption profile of water (Fig. 2-4k) demonstrates how effective water is at absorbing light. In fact, water has the ability to mask the absorption from other molecules (see Section 3.4 for further details). I use the location of the water absorption to determine the regions, for each HITRAN biosignature gas, where detection is more probable due to less overlap by water features.

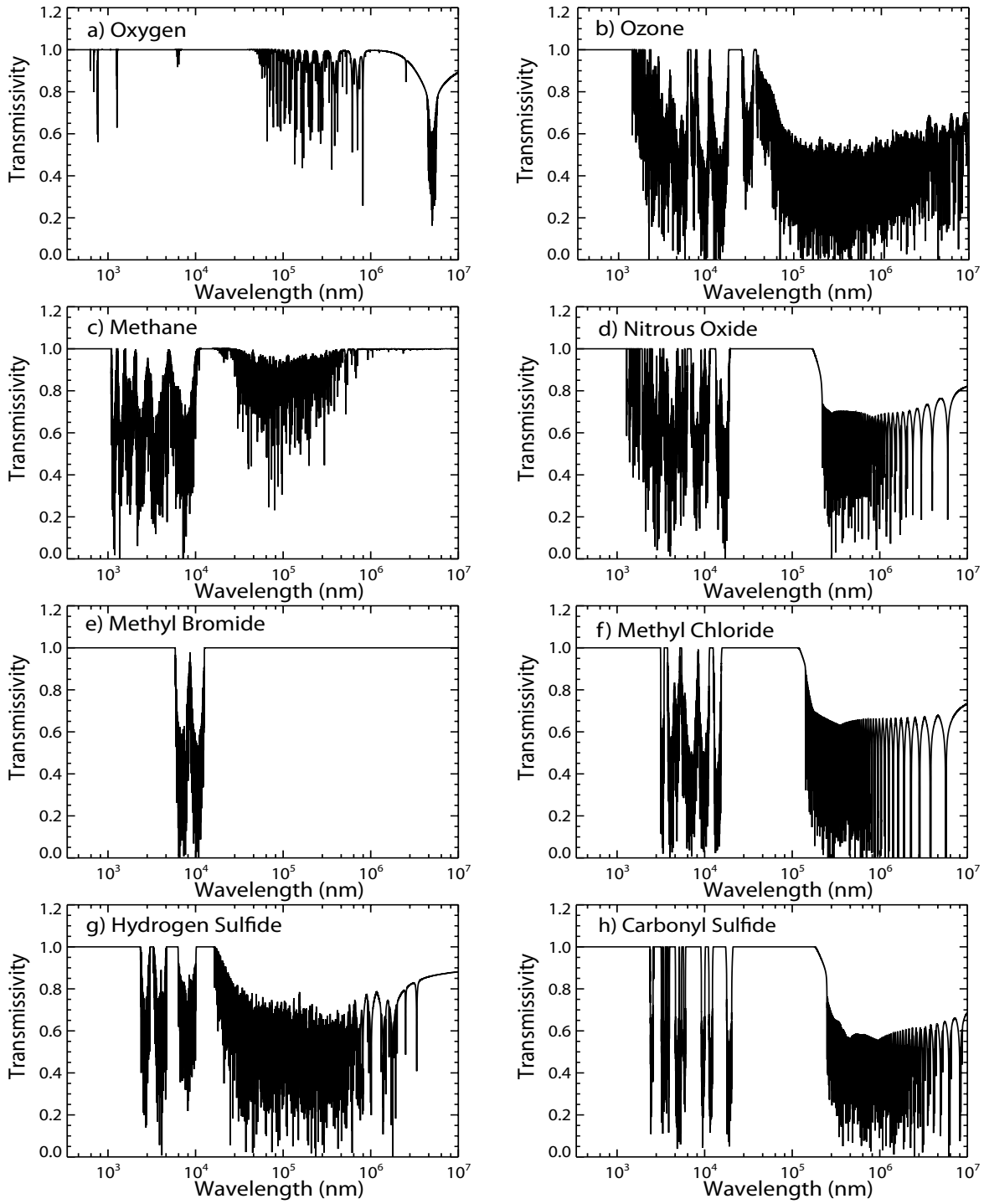

Figure 2-4: Wavelength regions where the HITRAN database has line intensity data for each molecule. Each subfigure represents the transmissivity spectrum resulting from an atmosphere consisting of 100% of the respective gas. The modeled atmosphere has an Earth-like temperature/pressure profile. The spectra are representative of an 86 km annulus surrounding a planet with a radius equal to Earth's radius. These figures do not incorporate any observational noise or wavelength binning.

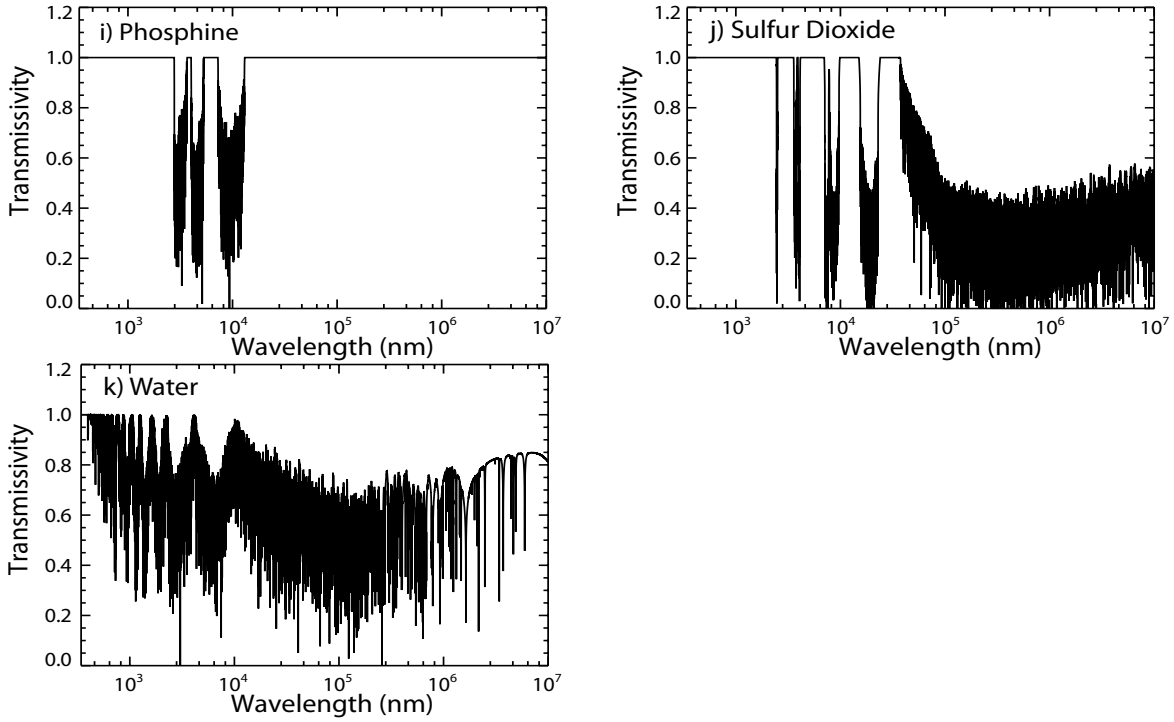

Figure 2-4: cont.

2.8 Methodology of Exploration

Using the theory developed and the molecular data provided in this Chapter, I calculate the molecular absorption cross sections for each HITRAN biosignature gas listed in Table 2.1. I input the calculated absorption cross sections into my transmissivity radiative transfer algorithm and, by varying the atmospheric mixing ratios of the gases, I produce simulated transmissivity spectra. A further description of my study along with the motivation behind my study can be found in Section 1.5. The results of the HITRAN biosignature gas investigation can be found in Chapter 3 with discussion following in Chapter 4. All information pertaining to the investigation of the PNNL/NIST biosignature gases can be found in Section 4.7.

Chapter 3

Results

3.1 Telescope Aperture Size

One battle for detecting the constituents of an atmosphere is the ability to observe enough photons that travel through the atmosphere. One of the main factors that contributes to the total number of photons observed is the telescope aperture. Basically, the larger the aperture, the more photons that can be recorded. Observing more photons is especially important because the synthetic noise, which is based solely on shot noise in my study, decreases in strength as more photons are observed. Therefore, increasing the number of observed photons will help spectral features become more visible over the imposed noise. Furthermore, limiting the shot noise will govern how future telescopes are designed because if we cannot reduce such noise sources, then we will be unable to detect anything in exoplanet atmospheres.

I show the telescope aperture effect for a 100 percent O_3 atmosphere for four telescope diameters: 6 m, 20 m, 50 m, and 100 m (see Fig. 3-1). I have chosen O_3 because the HITRAN database has a large number of published line intensities (over 400,000) and O_3 should be detectable in an atmosphere for even very small atmospheric O_2 abundances. The ozone atmospheric abundance of 100 percent is chosen so that the locations of the spectral features are obvious. The ozone telescope aperture models represent an Earth-like temperature/pressure atmosphere on an Earth-size planet orbiting a Sun-like star at a target distance of 35.45 parsecs with an observation time

equal to 100 hours.

The dramatic effect of the photon noise can be seen in Fig. 3-1. The reason for such noisy data for the 6 m telescope in Fig. 3-1a is due to not enough photons being observed with the 6 meter aperture. The amount of noise decreases as the telescope size increases as seen in Figs. 3-1b − d. Similar levels of noise for each telescope size and similar reduction in the strength of the noise as the telescope size is increased occurs for all modeled HITRAN molecules. Given the synthetic noise in my model, it would be difficult to propose that a 6 m class telescope could detect, with a significant degree of confidence, biosignature gases on an Earth-like exoplanet orbiting a Sun-like star for a target distance of 35.45 parsecs. In fact, the results for many of the HITRAN biosignature gases (see Section 3.5) point to a 35 meter class or larger telescope to be required in order to detect atmospheric gases.[1,2] Since the 6 meter class does not produce satisfying results, I focus on larger aperture sizes (20 m, 35 m, 50 m, and 100 m) for the investigations presented below.

3.2 Detection Metric

In order to determine the detectability of a biosignature gas, I must set a threshold for detection. I am conservative in my detection metric by requiring a signal-to-noise ratio equal to 10 for a biosignature gas spectral feature to be considered detectable. The reasoning for choosing such a high SNR is to account for my model not including other noise sources and possible statistical effects from modeling only one β in Eq. (2.27) [see Section 4.4.1 for more details concerning the stastical effects from the Gaussian distribution β from Eq. (2.27)]. The signal-to-noise ratio is calculated through

$$SNR = \frac{T_{out} - T_{in}}{\sqrt{\sigma^2_{T_{out}} + \sigma^2_{T_{in}}}}, \tag{3.1}$$

[1]The specific detection metric is discussed in Section 3.2.

[2]It is very important to emphasize that my models refer only to Earth-like temperature/pressure atmospheres on Earth-size planets orbiting Sun-like stars. Different atmospheric sizes, different stellar spectral classes, different temperature/pressure structure of the atmosphere, etc. will affect the detectability of a biosignature gas on an exoplanet as well as the telescope aperture required to detect the gases.

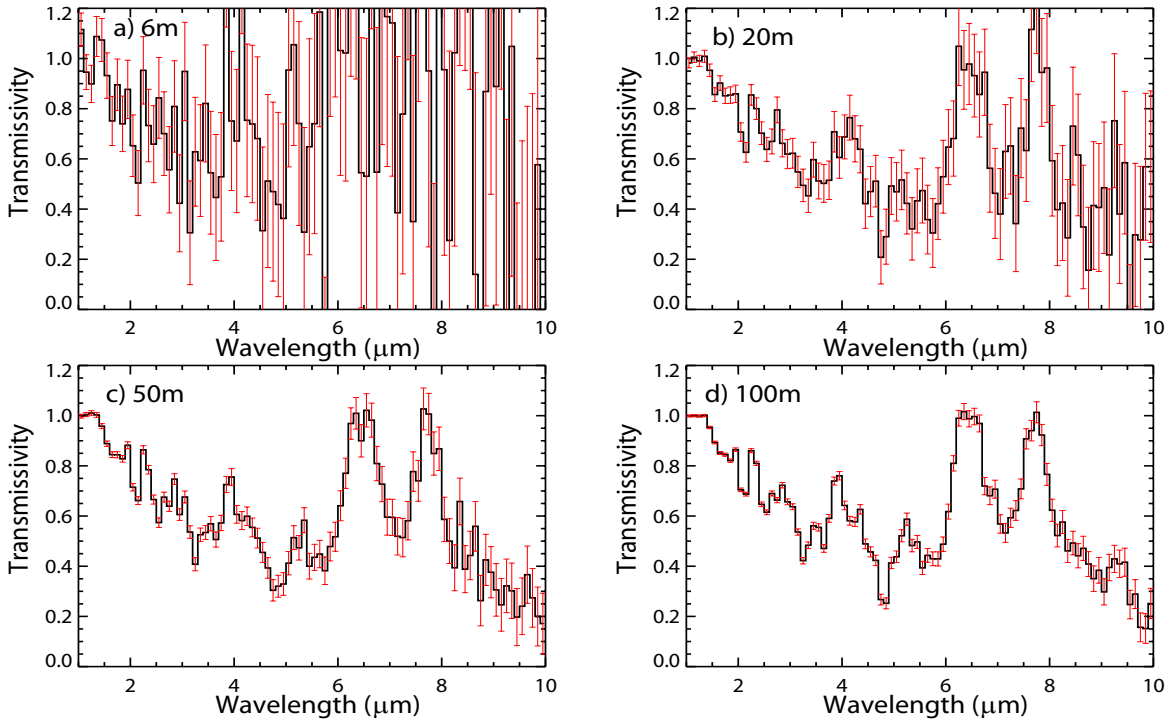

Figure 3-1: Transmissivity spectra for a 100% ozone atmosphere for telescope sizes as indicated in each subfigure for a source located at 35.45 parsecs, observed for 100 hours, and modeled within 20% of the shot noise. The noise level decreases with increasing telescope size due to the increased number of photons observed with larger telescopes. For the 6 m telescope, similar indiscernability occurs for all modeled HITRAN biosignature gases, and, thus, the 6 m telescope size will not be considered further in this chapter. The level of detectability for each class of telescopes in this figure is representative of all modeled HITRAN biosignature gases. These transmissivity spectra are representative of an 86 km annulus surrounding a planet with a radius equal to Earth's radius. See text for further details.

where T_{out} is the transmissivity value of the continuum, T_{in} is the transmissivity value of the feature, $\sigma_{T_{out}}$ is the error on the continuum transmissivity, and $\sigma_{T_{in}}$ is the error on the in-feature transmissivity. Even though I require an SNR = 10 for successful detection of a HITRAN biosignature gas, I present the SNRs for each biosignature gas spectral feature such that if someone chooses an alternate SNR for successful detection, he or she can easily determine which molecules are detectable and how the conclusions change based on the researcher's chosen SNR.

3.3 Wavelength Regions Requiring Investigation

As alluded to in previous sections, the detectability of an atmospheric gas is strongly dependent on the number of photons observed. The maximum number of photons that have the potential to be observed depends on the number of photons released from the star. The emission of a star can be modeled as a blackbody as shown in Eq. (2.18). It is noticeable from the blackbody equation that the amount of energy released decreases rapidly towards longer wavelengths (sub-mm and beyond); thus fewer photons are released at longer wavelengths. With fewer long-wavelength photons released, less travel through the planetary atmosphere and even fewer arrive at a detector located at Earth. This relatively low signal at longer wavelengths (in combination with our current technology) severly limits our ability to probe longer wavelength radiation (sub-mm and beyond). The low signal in long wavelength regions is disheartening because many of the molecules in Fig. 2-4 show significant absorption in the long-wavelength regions. Unfortunately, without a large source of long wavelength radiation impinging the exoplanet atmosphere, many of the long-wavelength features lay undetectable on targets at realistic distances from Earth.

To demonstrate the requirements for observing in long wavelength regions, I once again use ozone as the case study. In effort to retrieve the required large number of photons (in order to decrease the photon noise), I model a telescope aperture of 1000 meters. Though the 1000 m telescope size is unrealistic, it very appropriately emphasizes the difficulty in observing the long wavelength regions. Figure 3-2 shows

transmissivity spectra for a 100 percent ozone atmosphere with observations using a 1000 meter telescope aperture for 100 observation hours for a target located at a distance of 35.45 parsecs for the a) IR, b) sub-mm, c) far-IR, and d) millimeter wavelength regions, respectively. The large telescope size makes detection of ozone in the IR very easy as the red error bars are about the same size as the histogram line width. As one moves to the Sub-mm region, the absorption and corresponding error still allows for reasonable detection. Problems clearly begin to arise in the far-IR (0.1 $-$ 1 mm) where it becomes clear that even a 1000 meter telescope is not large enough to collect the number of photons required to decrease the photon noise sufficiently in order to detect ozone. As expected, the millimeter region is the worst of all with error bars larger than the transmissivity axis for the majority of the wavelengths.

Similar degradation in detectability as the wavelength increases occurs for each HITRAN biosignature gas in this study. As the telescope size decreases from 1000 meters, the degradation begins to occur at lower wavelengths. For example, for a 100 meter telescope, the degradation begins in the sub-mm range, while the degradation begins in the IR for a 20 meter telescope. The larger degradation that occurs as wavelength increases is due to the combination of the thermal blackbody spectrum of the star (as described above) and the fact that the photon noise (as discussed in Section 2.4) decreases proportional to the inverse square root of the number of photons observed. Thus, the lower the number of photons observed at increasing wavelengths, the larger the noise and hence, the degradation at longer wavelengths.

Due to the degradation, I can eliminate wavelength regions requiring investigation. The millimeter region is clearly out as even a 1000 meter telescope cannot retrieve enough photons to realistically observe in the millimeter region. The far-IR is also not a region that would provide any useful data for realistic telescope sizes (telescopes smaller than 100 meters). The sub-mm region is a toss up depending on what telescope size one chooses to model. However, even a telescope size of 100 meters would not feasibly be able to observe at wavelengths greater than 30 μm. It is possible that a 50 meter telescope may be able to detect features in the sub-mm between $10 - 20$ μm, but not anything at larger wavelengths. As the 50 m and 100 m

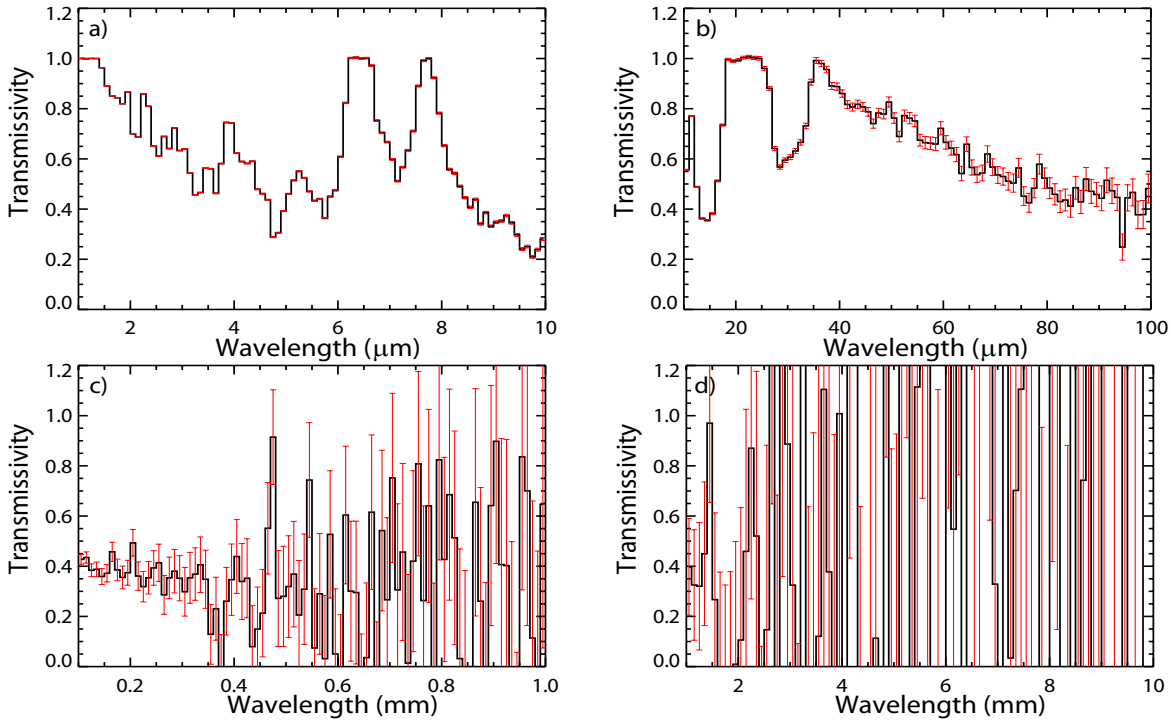

Figure 3-2: These figures demonstrate the transmissivity spectra (modeled within 20% of the shot noise) that would result from a 100% ozone atmosphere observed with a 1 km telescope aperture for 100 hours of observation time with the distance to the source equal to 35.45 parsecs for the a) IR, b) sub-mm, c) far-IR, and d) the millimeter wavelength regions. These transmissivity spectra are representative of an 86 km annulus surrounding a planet with a radius equal to Earth's radius. While the 1 km telescope is unrealistic for current technology, it demonstrates that even that large of a telescope would only allow for detectability in the IR and sub-mm and thus a larger telescope is required if one wants to probe the far-IR or mm wavelength regions.

telescopes are well beyond current technology, I will ignore their ability for detection in the sub-mm. I am now left with only two other wavelength regions: the visible and the IR. The only modeled HITRAN biosignature gas in my study that has data in the visible region is molecular oxygen; therefore, unless more visible data for the HITRAN biosignature gases are published, the visible region cannot be used reasonably in my study. The lack of data for spectral features in the visible wavelength range is disheartening because the emission profiles of many stars peak in the visible and thus are releasing substantial amounts of photons which may exist in number large enough to provide detectable signals from the atmospheres of exoplanets. The remaining region, the IR, is a middle ground for many of the difficulties of my study (existence of spectral data, sufficient incident photons, realistic telescope size, etc.) and will thus receive the most attention in the analysis below as it provides the most promising range for detectability.

3.4 Inclusion of Water

Water vapor is not a biosignature gas, though liquid water is believed to be necessary for life to exist unless some other molecule can provide the same functionality as water. I include water vapor in my study due to its importance to life and because its broad absorption features (demonstrated in Fig. 2-4k) could overlap the spectral features of the biosignature gases. Depending on the severity of the overlap and the spectral resolution of the observations, some biosignature molecular features may not be observable. For my analysis, I have restricted the atmospheric water vapor abundance to equal a globally averaged one percent. If water vapor has an influence on the detectability of a particular HITRAN biosignature gas spectral feature, I discuss its impact on that particular feature during the results analysis below. Though I choose an atmospheric water vapor abundance of 1% for my HITRAN biosignature gas models, one can conceptually picture that a larger or smaller water percentage would lead to larger or smaller influences on the transmissivity spectra, respectively. Therefore, for future observational studies of exoplanetary atmospheres, it is imperative to have

significant confidence on the atmospheric water vapor abundance in order to deduce the atmospheric abundances of other atmospheric species.

3.5 Biosignature Gases

Since Fig. 3-1a demonstrates that a telescope aperture larger than 6 m will be required to detect biosignature gases at reliable SNRs, I will be analyzing four alternative telescope sizes (20 m, 35 m, 50 m, and 100 m), where each represents a different class of telescopes. I have now included a 35 m telescope as this telescope size is a natural technological step likely required between the 20 m and 50 m telescope technologies and due to other studies (e.g., Ehrenreich et al. 2006) emphasizing that a $30 - 40$ meter telescope would be required to detect Earth-like atmospheres on exoplanets.

In the following section, I split each HITRAN biosignature gas into its own subsection. For each gas, I describe the spectral features that provide the best opportunities for detection and eliminate weaker features that do not warrant investigation. For each HITRAN biosignature gas, I describe how the detectability varies with changing telescope size and varying atmospheric abundances. I augment the analysis with figures demonstrating the transmissivity spectra for chosen atmospheric abundances for each modeled telescope size. The referenced tables provide the data for the spectral features, the chosen continuum, and the detectability (SNR) of the spectral features. The modeled biosignature gas atmospheric abundances listed in the tables decrease in the order of 100%, 50%, 20%, and 1% and then by orders of magnitude until the particular feature is indiscernible from the continuum. I designate a feature as "indiscernible" when its absorption depth is effectively the continuum or when its corresponding error approaches values similar to the variation in the transmissivity data. The first case of indiscernability tends to occur for larger telescope sizes (e.g., 100m) while the second case occurs for smaller telescopes (e.g., 20 m). I occasionally increase the wavelength bin size at longer IR wavelengths in order to try to reduce the photon noise so that the long-wavelength molecular features can become discernible. The technique of binning at a lower resolution is common in theoretical and observational

studies. The analysis of each biosignature gas follows below.

3.5.1 Oxygen

The only observable feature for O_2 is in the visible region at 765 nm. Figure 3-3 shows the transmissivity spectra for chosen atmospheric abundances for the four modeled telescopes. As previously discussed, all models include one percent atmospheric H_2O to determine where overlapping features may occur. The 765 nm O_2 feature becomes indiscernible from the continuum in Fig. 3-3a−c and Fig. 3-3d for an atmospheric abundance of one percent and 20 percent, respectively. The exact data and level of detectability (the SNR) are listed in Table B.1. The reason O_2 is not visible for lower abundances (like other molecules) is due to O_2 not having strong features. The narrowness of the 765 nm feature also plays a role as a broader feature may be more detectable at lower abundances. Though, it is convenient that the O_2 feature occurs between the two H_2O features as opposed to overlapping with one of them. Unfortunately, none of the models lead to high SNRs except for those for the 100 m telescope; however, since such a telescope is well beyond current technology, I conclude that the realistically attainable SNRs for O_2 do not provide for undeniable detection. Although, if one is satisfied with a 4σ detection, then O_2 could be detected with a 50 m telescope.

A contradiction to the claim that O_2 can only be distinguished in the visible region may seem valid if one notices the O_2 IR features in Fig. 2-4a. However, these features are so narrow that they disappear during the wavelength binning process. In order to detect such features, one would need a higher resolution than that included in my models (the O_2 IR is binned at a 0.1 μm resolution). If a high enough resolution is used and if the molecular absorption is strong enough, then the IR may be a suitable region to detect O_2.

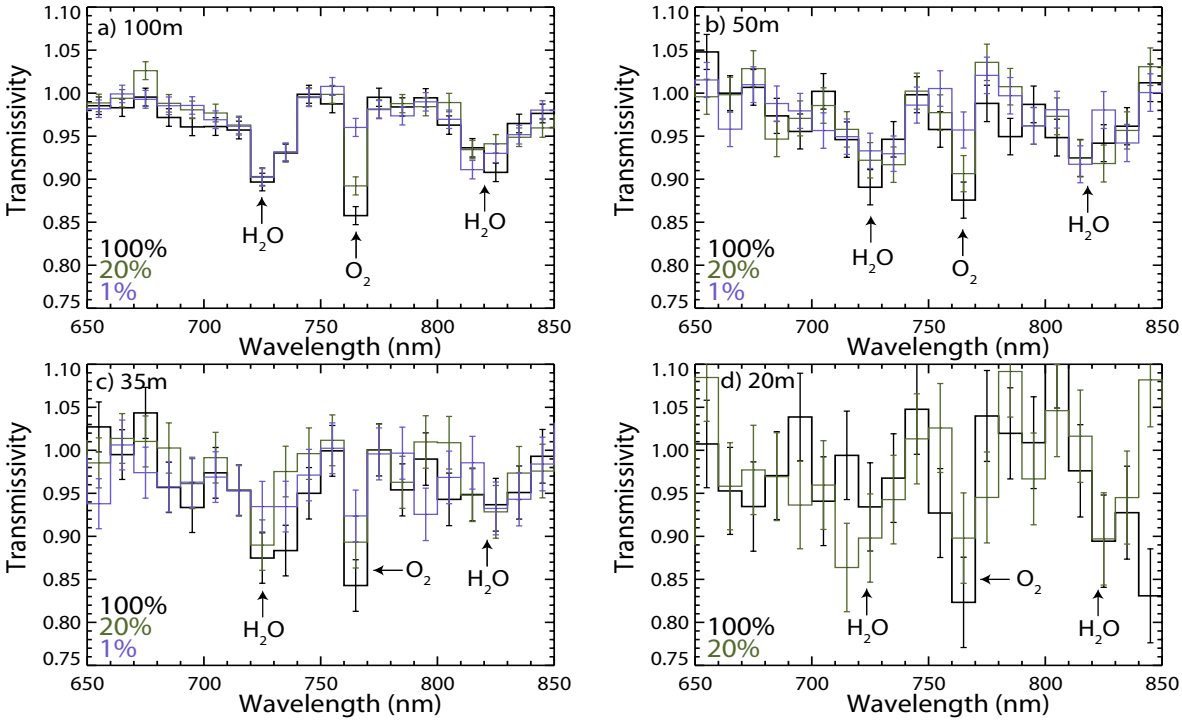

Figure 3-3: Oxygen: For varying telescope sizes and oxygen atmospheric abundances, these figures demonstrate the anticipated visible transmissivity spectra (modeled within 20% of the shot noise) for a source (orbiting a Sun-like star) located at 35.45 parsecs and observed for 100 hours. These transmissivity spectra are representative of an 86 km annulus surrounding a planet with a radius equal to Earth's radius. The oxygen and nearby water features are indicated in each subfigure. The atmospheric water abundance for these models is 1%. The bin size is equal to 10 nm.

3.5.2 Ozone

The detection of ozone in exoplanet atmospheres holds great importance as it can act as a tracer for O_2. Specifically, O_3 lines saturate for levels of O_2 which are undetectable in remote sensing. To determine the detectability of ozone, I modeled and analyzed the most important and distinguishable ozone features within the IR wavelength region. The five features presented occur at approximately 3.25, 3.65, 4.75, 5.75, and 9.65 μm. Figure 3-4 plots the features for chosen atmospheric abundances for the four telescope sizes. The current "messiness" in some of the plots is a very important detail specifically included (and, to some level, will be included in the following molecules as well). The data degradation demonstrates the importance of observing enough photons such that the noise decreases in a manner that the individual spectral features can be observed. As seen in Fig. 3-4, as the telescope size decreases and/or as the abundance decreases, the noise begins to mask features. It is important to note that only one abundance is plotted in Fig. 3-4h. Only plotting one abundance is due to the wavelength range of Fig. 3-4h for the 20 m telescope being dominated by noise. Even though I have arrowed where O_3 should have features in Fig. 3-4h, none of the features would be detectable because the variation in the noise is on the same order as the depth of the features. The non-detectability of the ozone features in Fig. 3-4h is supported by plotting a zoomed-out ozone IR spectrum (not shown).

Table B.2 lists the detectability of each of the analyzed ozone features for varying telescope sizes and atmospheric abundances.[3] The 100 m telescope does an amazing job at resolving the first four features (3.25, 3.65, 4.75, and 5.75 μm) with an SNR above 10 in all cases, while it maintains an SNR larger than 5.0 for the majority of the abundances for the 9.6 μm feature. Moving to slightly more realistic telescope sizes, the 50 m and 35 m telescopes do quite well themselves with an SNR larger than 5.0 in the majority of cases. Only for smaller atmospheric abundances do the SNRs

[3]For broad features and for some narrow features, the center of the band sometimes "wanders" between bins. In these cases, I have used my experience to choose the proper location (i.e. λ) for the feature for each trial. This reasoning is why some of the features appearing in Table B.2 are centered in one bin (e.g., 3.25 μm) for some of the telescope sizes/abundances and a different bin (e.g., 3.35 μm) for others.

for the 50 m and 35 m telescopes drop below 5. The 20 m telescope has much more difficulty exploring the IR wavelength region as its SNR ranges from $2 - 4$ in most cases, though the 20 m telescope shows higher SNRs for the 4.75 μm feature which is one of the stronger and more detectable O_3 features in this wavelength region. The 20 m telescope does encounter significant problems for the longer wavelength 9.6 μm feature where it can actually not detect the feature even for a 100% atmospheric ozone abundance. The difficulty for detectability with the 20 m telescope arises from the "smaller" telescope not being able to observe enough photons to reduce the noise within the IR wavelength region.

While water does not hide all ozone features within the IR spectral region (as indicated by the detectability listed in Table B.2), water vapor does act to mask a few spectral features. The most important place in the spectrum where the water masking occurs is near 7 μm where ozone has a significant absorption feature with its continuum rising directly to a transmissivity value equal to unity on both sides of the feature. Such an absorption would typically be a golden opportunity for detection as the continuum for most other spectral features (due to the broadness of the absorption profiles) is forced to be chosen at a relative value since the transmissivity profile does not usually return to equal unity between such features. Unfortunately, the 7 μm feature is nearly completely masked by a broad band water feature which spans from approximately $4.5 - 8$ μm. This broad water absorption feature does not significantly affect the 4.75 or 5.75 μm features but completely absorbs within the low-wavelength, transparent (where Transmissivity=1) side of the 7 μm feature. By removing the low-wavelength, clearly distinguishing continuum from the 7 μm O_3 feature, water essentially masks this feature. Remnants of the feature can still be seen just longward of 7 μm in Figs. 3-4e and f; however, I determined this signal to be too minute in reference to the surrounding noise and thus did not include it in the detectability analysis.

The effective masking of the 7 μm ozone feature by water vapor shows the importance of including water in any such analysis that models terrestrial-like planets. Without such inclusion, one could come to a conclusion that the 7 μm ozone feature

is a great feature to target telescope observations, when in fact, it is not. It is important to note that other molecules can act as spectral masks. One could determine the potential masking of each biosignature gas presented in my study by comparing where each molecule's spectral features occur in the respective wavelength regions. Simply by placing the presented transmissivity spectra from each molecule side-by-side, one can begin to develop a sense of the best regions for observation in the presence of other potential masking sources.

3.5.3 Methane

The three most promising IR features for detecting CH_4 occur at approximately 2.35, 3.35, and 7.85 μm. The 7.85 μm feature resembles much more of a band than a spectral line because CH_4 absorbs between $5 - 10$ μm with the exact broadness depending on the modeled atmospheric abundance. However, due to overlap with water absorption, the CH_4 band is only visible on the long wavelength side of the band. Luckily, the water band only absorbs between $4.5 - 8$ μm where the absorption tails off at the longer wavelengths and thus, the methane absorption is not completely covered. The 7.85 μm wavelength is chosen as one possible wavelength for the detection of this methane band.

As anticipated, the 100 m telescope provides astonishing detectability with SNRs reaching upwards of 30 for larger atmospheric abundances for the 2.35 and 3.35 μm features. The 100 m telescope can even detect low atmospheric abundances (e.g., 100 ppm) with an SNR of approximately 15 for both the 2.35 and 3.35 μm features. The 50 m telescope provides significant detectability for the 2.35 and 3.35 μm features with SNRs ranging from 8 to 17 depending on the atmospheric abundance, while the 35 m telescope provides detection for the 2.35 and 3.35 μm features ranging from 6σ to approximately 14σ. For either feature, the 20 m telescope provides for detections less than 7σ for each atmospheric abundance modeled, though it does provide 5σ detections for the majority of abundances modeled.

Due to the lower number of incident photons, the 7.85 μm feature is more difficult to detect than the 2.35 and 3.35 μm features. In order to counteract the lower number

of incident photons at longer IR wavelengths, I have binned the surrounding region at a lower resolution (0.2 μm bins instead of the 0.1 μm bins used for the 2.35 and 3.35 μm features). The SNR barely reaches 12 for the 100 m telescope. While the SNR for the 100 m telescope is above 5σ in all cases for the other telescope sizes, the only other 7.85 μm detection with an SNR above 5 occurs for a 50 m telescope with 20% atmospheric abundance. All other telescope sizes and atmospheric abundances return SNRs lower than 5 for this feature. The low signal results for the 7.85 μm methane feature suggest that definitive detection may require a telescope size at least greater than 35 m.

Table B.3 shows the corresponding data and calculated SNRs for all three of the methane features for varying atmospheric abundances while Fig. 3-5 shows the transmissivity spectra for each telescope size for a chosen set of atmospheric abundances. The 10 ppm line plotted in Fig. 3-5a, b, e, and f demonstrates the atmospheric abundance at which the CH_4 features are no longer observable.[4] Since the contribution to the transmissivity spectrum from CH_4 is so low at an abundance of 10 ppm, the absorption in these transmissivity spectra is mainly resulting from the 1% H_2O included in the models. Figures 3-5a and b demonstrate very nicely how decreasing atmospheric abundance causes a decrease in absorption up until the point of nondetectability. The distinctions in transmissivity spectra of different modeled abundances demonstrate how the atmospheric abundances could be estimated through modeling techniques. As usual, the 20 m telescope shows the most difficulty in resolving the features due to the lower number of photons observed in comparison to the larger telescope sizes.

[4]The atmospheric abundance corresponding to a nondetectable biosignature feature is determined by comparing the spectrum that includes both the biosignature gas and the one percent water profile with the spectrum that only includes the one percent water profile. The biosignature gas no longer contributes to the absorption in a detectable way at wavelengths where these two spectra are equivalent.

3.5.4 Nitrous Oxide

Nitrous oxide has a variety of features within the infrared region. I have chosen the four most promising of these features to highlight for N_2O's potential detectability. The first two features (4.05 and 4.55 μm) both occur in a region where water contributes very little to the absorption. In fact, a 1% water contribution has a transmissivity value nearly equal to unity in the region of these features thus making them prime candidates for detection. The last two features (approximately 7.85 and 8.65 μm) occur on the long wavelength edge of the water band that stretches between approximately 4.5 and 8 μm. These features are close enough to the edge of the water band that their absorption has the potential to be distinguished. Figure 3-6 plots the transmissivity spectrum for chosen atmospheric nitrous oxide abundances while Table B.4 provides the relevant data and SNR of each analyzed spectral feature for each modeled telescope size and atmospheric abundance. In Fig. 3-6, the first two features have a bin resolution of 0.1 μm while the last two features have a bin resolution of 0.2 μm. The two longer wavelength features are plotted with a lower resolution in order to decrease the shot noise so that the spectral features are more discernible. This modified binning is the same as I used for the longer wavelengths of CH_4.

For the first two features (4.05 and 4.55 μm), the 100 m telescope provides very nice detectability with SNRs above 9 (reaching as high as 17 in some cases) for the majority of the modeled abundances. One interesting aspect for the 100 m telescope is that it can detect the 4.55 μm feature of N_2O at a 5σ level for an atmospheric abundance as low as 100 ppb. This detectability provides great promise for very future generation instruments being able to detect very low biosignature gas abundances on exoplanets. For the 4.05 μm feature, the 50 m and 35 m telescopes achieve decent SNRs (above 5) for the higher abundance models, but are unable to attain 5σ detections for abundances of 1000 ppm or lower. The 4.55 μm feature is the stronger of these features, and the 50 m telescope obtains a detection level above 5σ for abundances larger than 100 ppm and barely misses a 5σ detection (detecting at

a 4.6σ level) for an atmospheric abundance of 10 ppm. The 35 m telescope does well itself for the 4.55 μm feature by producing detections larger than 5σ for abundances larger than 1000 ppm and detections close to 4σ for atmospheric abundances of 100 ppm and 10 ppm. While the 20 m telescope does not do well for the 4.05 μm feature (with detection levels ranging from approximately 1.5 to 4σ), it almost reaches a detection level of 5σ for the 4.55 μm feature at higher atmospheric abundances. The variation that occurs in the detection level for the 4.55 μm feature with the 20 meter telescope (namely, that the detection for a lower abundance of 1000 ppm is larger than that of many of the higher abundances) is a result of the variations in the absorption depth of the feature and the level of the continuum. Similar occurances appear in other models/molecules and may lead to a slightly overestimated SNR due to the nature of the synthetic noise in the models. However, it is not anticipated that such occurances will affect the broad-scale results of my study.

The longer wavelength features (7.85 and 8.65 μm) are more difficult to detect for the same reasons as discussed for previous molecules. The lack of a significant amount of detected photons for this wavelength region leads to larger noise (due to the properties of shot noise) and thus lower detectability (i.e. lower SNRs). In this manner, the 100 m telescope only reaches detectability above 10σ for two models, though it does attain SNRs near or above 7σ for the majority of the models. For the 7.65 μm feature in particular, the 50 m and 35 m telescope provide for detections ranging from approximately 3 to 6σ. The higher edge of this detectability range is slightly more promising but any detection of 3σ is subject to scrutiny. The 20 m telescope barely achieves 3σ for the detection of the 7.65 μm feature. For the 8.65 μm feature, the SNRs are typically lower than that of the 7.65 μm feature when comparing similar telescope sizes and atmospheric abundances between these two features.

Though the outlook for detecting N_2O is not terrible (especially when the atmospheric abundance is not too low), I would have hoped for better detection especially at shorter wavelengths where there is not as much overlap with water features. However, the opportunity for large scale telescopes (e.g., 100m) to detect very low

abundances of N_2O is very promising.

3.5.5 Methyl Bromide

From Figure 2-4e, it is seen that CH_3Br only has two published spectral features (centered near 7 and 11 μm) in the HITRAN database. Since these two features span two of my regions (the long wavelength IR and the short wavelength sub-mm by my region definitions), I have created a specialty wavelength region ($4 - 13$ μm) for analysis (binsize = 0.25 μm). As these two features are quite broad (as seen in Fig. 2-4e), the deepest absorption for each feature sometimes occurs at different wavelengths. This aspect is demonstrated in Fig. 3-7 and Table B.5, which show transmissivity spectra for chosen atmospheric abundances and the relevant spectral data, respectively.

I have chosen to preferentially probe the long wavelength side of the 7 μm feature for detectability determination. The reasoning for this decision is based on the 7 μm CH_3Br feature nearly completely overlapping (in wavelength space) with an H_2O absorption band. However, the CH_3Br feature is responsible for a higher percentage of absorption on the long wavelength side (i.e. where I probe). For high enough atmospheric abundances (as listed in Table B.5), the absorption depth cannot be attributed solely due to H_2O absorption and thus the absorption from CH_3Br can be detected with the SNRs listed in Table B.5.

The 100 m and 50 m telescopes provide very good SNRs (>10) for most of the atmospheric abundances for the first methyl bromide feature (7.625 μm). The advantage of the larger telescopes for methyl bromide is that they can detect CH_3Br at an abundance as low as 100 ppm at a level above 8σ. The 35 m telescope does quite well with nearly 10σ detections for atmospheric abundances larger than 20% and provides almost a 5σ detection for an atmospheric abundance of 100 ppm. The 20 m telescope only provides SNRs around 4 for the modeled abundances for the 7.625 μm feature. The 5.2σ detection with the 20 m telescope for the 1000 ppm atmospheric abundance should be taken lightly as this detection is most likely an overestimation caused by the variability in the noise and particular location chosen to measure the feature.

The second methyl bromide feature (approximately 10.5 μm) has the potential to be a more distinguishing feature for CH_3Br because water does not contribute significantly to the absorption in this wavelength region (approximately $9 - 13$ μm depending on the exact model parameters chosen); however, the calculated SNRs for the 10.5 μm feature are less than the SNRs of the 7.625 μm feature. The 100 m telescope can still detect above 10σ for abundances equal to or larger than 1000 ppm. Interestingly, it can detect the 10.5 μm feature at a 3.5σ level for an atmospheric abundance of 1 ppm. While a 3.5σ detection will be subject to scrutiny and require subsequent verification, this ability of the 100 m telescope holds promise for future missions detecting low abundances of methyl bromide on exoplanets. The 50 m telescope maintains SNRs for the 10.5 μm feature above 5σ for the majority of the abundances while the 35 m telescope has detections ranging from $3.5 - 6.6\sigma$ depending on the exact atmospheric abundance modeled. The 20 m telescope agains lacks in its ability by only producing detections near the 3σ level. The data for all of the above conclusions are listed in Table B.5.

Figure 3-7 plots the transmissivity spectra of methyl bromide for chosen atmospheric abundances for each telescope size. Figures 3-7a and b show how the absorption weakens as the atmospheric abundance decreases. One interesting aspect for Figs. 3-7a and b can be noticed when comparing the 10 ppm transmissivity profile with Table B.5. For the 10 ppm CH_3Br model, the absorption seen in the 7.625 μm feature for the 100 m and 50 m telescope is due solely to water and thus methyl bromide does not contribute to a noticeable level in this band for an atmospheric abundance of 10 ppm; however, as water does not absorb significantly between approximately 9 and 13 μm, the CH_3Br absorption from an atmospheric abundance of 10 ppm can be detected for the 10.5 μm feature at SNRs provided in Table B.5. Figures 3-7c and d show the difference in spectral profiles for atmospheric abundances of 100% and 1000 ppm for the 35 m and 20 m telescopes, respectively. For the 35 m telescope, these two abundances map how the absorption decreases as the atmospheric abundance decreases. The decrease in absorption strength is not as noticeable for the 20 m telescope because the worsening noise hides this variation for the 20 m

telescope.

3.5.6 Methyl Chloride

Methyl Chloride has four distinct features within the IR region located at approximately 3.25, 4.05, 4.85, and 7.25 μm. I analyzed each of these features with the typical telescope sizes and atmospheric abundances as used for previous molecules. Though I measure near 7.25 μm, the broad CH_3Cl feature actually ranges from approximately $5.25 - 8.5$ μm. I analyze at a wavelength longward of the center of this range because the overlapping, broad water feature has a lower contribution at these longer wavelengths.

The 3.25 μm feature provides the highest SNR for detection for each telescope as compared to the other three features. The 100 m, 50 m, and 35 m, and 20 m telescopes can detect a 100 ppm CH_3Cl atmosphere with SNRs of 14.2, 6.9, 5.5, and 4.0, respectively. The 50 m, 35 m, and 20 m telescopes cannot detect the 3.25 μm feature at lower abundances because the feature becomes indiscernible from the water absorption; however, the 100 m telescope can detect an abundance down to 10 ppm with an SNR of 12.7. The only telescope that can detect the 4.05 μm feature at levels above 10σ is the 100 m telescope for atmospheric abundances equal to or larger than 1000 ppm. The 50 m and 35 m telescopes make detections for the 4.05 μm feature above 5σ for abundances equal to or larger than 1000 ppm and 1%, respectively, while the 20 m telescope only achieves, at maximum, a 4σ detection for the 4.05 μm feature.

The 4.85 μm feature has the lowest detectability on average when comparing to the other three features. A 10σ detection only occurs for a 100% CH_3Cl atmosphere and the 100 m telescope. The 50 m, 35 m, and 20 m detections for the 4.85 μm feature range from approximately $2 - 7\sigma$, $2 - 5\sigma$, and $2 - 3\sigma$, respectively; therefore, probing one of the other CH_3Cl features may be a better option in terms of detectability. The last feature, the 7.25 μm feature, holds more promise than its 4.85 μm counterpart. The 100 m telescope has SNRs above 10 for atmospheric abundances equal to or larger than 100 ppm, while the 50 m telescope maintains detections above 5σ for

those same abundances. The detectability ranges from approximately $3 - 6\sigma$ and $3 - 4.5\sigma$ for the 35 m and 20 m telescopes, respectively, for the 7.25 μm feature. These data and associated SNRs are listed in Table B.6.

Figure 3-8 plots the transmissivity spectra for chosen CH_3Cl atmospheric abundances for each telescope size. Figures 3-8a−d show the 3.25 μm, 4.05 μm, and 4.85 μm features at a 0.1 μm resolution while Figures 3-8e−h show the absorption from the 7.25 μm feature with a 0.2 μm resolution. Figure 3-8a demonstrates how the absorption strength decreases with decreasing CH_3Cl abundance. For Fig. 3-8a, the only detectable feature at an 10 ppm CH_3Cl abundance is the 3.25 μm feature, thus the rest of the 10 ppm plot demonstrates absorption from the 1% atmospheric water included in my models. For the 50 m telescope (Fig. 3-8b), none of the first three CH_3Cl features (3.25 μm, 4.05 μm, and 4.85 μm) are detectable for a 10 ppm abundance, and, thus, the 10 ppm curve in Fig. 3-8b also demonstrates water absorption. Though, in the 10 ppm curve in Fig. 3-8b, there appears to be CH_3Cl absorption at 4.85 μm, a zoomed-out plot (not shown) and a comparison to a pure 1% H_2O atmosphere (not shown) demonstrate this "absorption" to be consistent solely with water vapor and not with a significant CH_3Cl contribution. Figures 3-8c and d demonstrate the spectral profiles for 100%, 1%, and 100 ppm CH_3Cl atmospheres. The 100 ppm spectral profile for Figs. 3-8c and d demonstrates the lowest abundance for which CH_3Cl can be distinguished from the 1% water atmosphere for the 3.25 and 4.05 μm features, while, the 100 ppm profile also demonstrates the non-detectability of the 4.85 μm feature for both telescope sizes.

The last four subfigures, Figs. 3-8e−h, show the transmissivity profiles for varying CH_3Cl atmospheric abundances for each telescope size for the 7.25 μm feature. The continuum for the 7.25 μm feature is not shown because I zoomed-in on the feature in order to better show the profiles of varying abundances. Figure 3-8e nicely shows the effect from decreasing abundances while also depicting how the 10 ppm profile does not demonstrate a CH_3Cl feature and thus is indicative of the 1% water profile. The 10 ppm profile in Fig. 3-8f (the 50 m telescope) acts in the same manner as described for Fig. 3-8e while the 1% CH_3Cl profile in Fig. 3-8f demonstrates how the absorption

changes with decreasing abundance. Figures 3-8g and h demonstrate a few spectral profies for the 35 m and 20 m telescope, respectively, where the 100 ppm profile in each subfigure demonstrates the lowest abundance at which CH_3Cl absorption can be distinguished from the water absorption in the model.

3.5.7 Hydrogen Sulfide

Hydrogen sulfide has three IR bands centered approximately at 2.6, 4, and 8 μm. Unfortunately, the 2.6 μm band sits directly in the middle of a water band. Though the 2.6 μm absorption strength is larger for higher H_2S abundances than that of solely the 1% water absorption profile, a larger $\frac{H_2S}{H_2O}$ atmospheric composition ratio may not be distinguishable from an atmosphere simply containing a larger water abundance. The 8 μm band suffers a similar fate. Unfortunately, the H_2S absorption depth is similar to that of the water band; therefore, it would be increasingly difficult to distinguish the 8 μm H_2S band from absorption due to higher water concentrations. I have thus eliminated the 2.6 and 8 μm bands from the analysis and have continued solely with the 4 μm band.

The H_2S absorption is not symmetric within the 4 μm band, as the absorption is deeper on the short wavelength side (near 3.65 μm for most cases). The 4 μm band also encounters trouble due to the masking from water features because the H_2S band can only be discerned from the 1% H_2O profile for abundances equal to or larger than 1000 ppm for the 100 m, 50 m, and the 35 m telescopes. The 20 m telescope can only discern H_2S atmospheric abundances equal to or larger than 1%. While the 100 m telescope attains an 8σ detection for the 4 μm feature (data measured at 3.65 μm) for an atmospheric abundance of 1000 ppm, the 50 m and 35 m telescopes attain less than a 4σ detection for the same abundances. In fact, the 35 m telescope does not achieve a 5σ detection for any atmospheric abundance. The 20 m telescope achieves approximately a 3σ detection for atmospheric abundances of 1%, 20%, and 50% percent and can detect a 100% atmosphere at the 4.9σ level. The relevant data for each telescope size and modeled abundances are provided in Table B.7.

Figure 3-9 plots the transmissivity spectra of chosen atmospheric abundances for each telescope size. The H_2S band is indicated in each subfigure. The varying abundances in each subfigure demonstrate how the feature decreases in strength for decreasing atmospheric abundances. The 100 ppm H_2S profile in Figures 3-9a−c demonstrates the abundance at which the H_2S band is no longer discernible from the water absorption for those telescope sizes, while the 1% H_2S profile in Figure 3-9d shows the lowest modeled abundance at which the H_2S feature is discernible for the 20 m telescope. Due to the generally lower SNRs for H_2S (see Table B.7) in comparison to other biosignature features and since H_2S only has one realistically observable feature in the IR, it may prove more difficult to detect H_2S than other biosignature gases.

3.5.8 Carbonyl Sulfide

Out of nine possible IR features for carbonyl sulfide, I chose to analyze the four that appeared to have the best chances for detectability. These four features are located at approximately 3.45, 4.85, 5.25, and 5.85 μm. The first two features provide better opportunities for detection because the last two features are closer to the broad water band centered near 6.5 μm. Though, for higher abundances, all four features are seen over the absorption resulting from the 1% water atmosphere included in the models. The 100 m telescope can detect the 3.45 μm feature with an SNR above 12 for an atmospheric abundances equal to or larger than 100 ppm. Interestingly, the 100 m telescope can detect abundances as low as 100 ppb and 10 ppb at 3.4σ and 3.7σ level, respectively, for the 4.85 μm feature (the most detectable of the four features). The 50 m telescope demonstrates promising results as well with detections of no less than 6.7σ for the 3.45 μm feature for atmospheric abundances equal to or larger than 100 ppm. The 35 m telescope does surprisingly well for the 3.45 μm feature with detections above 5.4σ for atmospheric abundances larger than 100 ppm. As usual, the 20 m telescope does not do as well as the other telescope sizes with detections ranging between $2.4\sigma - 5.3\sigma$ for the varying OCS atmospheric abundances for the 3.45 μm and 4.85 μm features.

As previously mentioned, the last two features (5.25 μm and 5.85 μm) are not as easily detected as the first two features. The 100 m and 50 m telescopes can only discern the features from the water profile for OCS atmospheric abundances of 1000 ppm or larger while the 35 m and 20 m telescopes require OCS atmospheric abundances greater than 1%. With one exception (one atmospheric abundance for the 50 m telescope), the 100 m telescope is the only telescope to provide above 5σ detections for these two features. The majority of the 35 m detections hover around 2 or 3σ, though one of the modeled cases approaches nearly 5σ. The 20 m telescope essentially does not detect either of the last two OCS features as the SNRs are never larger than 3. The relevant data and associated SNRs are provided in Table B.8.

The four analyzed OCS absorption features are shown for varying atmospheric abundances and each telescope size in Fig. 3-10. The 100 m telescope transmissivity profiles demonstrate how decreasing abundance weakens the absorption on a global scale. Surprisingly, the 100 ppb curve in Fig. 3-10a still shows a semi-distinctive OCS feature near 4.85 μm (at a detection level of 3.4σ). The 50 m telescope (Fig. 3-10b) also demonstrates the 100 ppb absorption for the 4.85 μm feature. The 35 m telescope (Fig. 3-10c) does not have as noticeable of a 4.85 μm feature for an atmospheric abundance of 100 ppb as the SNR for this feature is less than 2. Such a low SNR would be unlikely to be attributed to OCS with any significant level of confidence. The 20 m telescope subfigure (Fig. 3-10d) shows two example spectral profiles (100% and 100 ppm OCS atmospheric abundance). The 100 ppm profile for the 20 m telescope shows the lowest abundance at which the first two features can be discerned from the continuum while concurrently showing the non-discernability for the last two features. When taking the OCS IR absorption as a whole in relation to the varying telescope sizes and modeled abundances, it is clear from Fig. 3-10 and Table B.8 that the best OCS IR feature (for discernability at low atmospheric abundances) is the 4.85 μm feature while the feature that provides the highest relative SNRs is the 3.45 μm feature.

3.5.9 Phosphine

Three phosphine bands exist in the IR with their deepest aborption located near 2.95, 4.45, and 9 μm. I only consider the first two of these bands in the analysis because the third one combines with the water absorption to produce a relatively flat spectrum longwards of 6 μm. The first feature (2.95 μm) nearly directly overlaps with water and thus is only distinguishable for PH_3 abundances equal to or larger than 1% for the 100 m, 50 m, and 35 m telescopes and 20% for the 20 m telescope. However, if the PH_3 atmospheric abundance is that high, then the related SNRs for the 2.95 μm feature are above 5 for all telescopes and modeled abundances. The second feature (4.45 μm) provides the ability to probe lower atmospheric abundances, but returns lower SNRs as well. The 100 m, 50 m, and 35 m telescopes can probe down to atmospheric abundances of 1 ppm with detections of 3.1σ, 2.9σ, and 2.3σ, respectively. The 20 m telescope probes down to a 10 ppm atmospheric abundance with a detection of 2.4σ. Unfortunately, for the 4.45 μm feature, for the 50 m, 35 m, and 20 m telescopes, only two modeled abundances (100% and 50% for the 50 m telescope) have SNRs greater than 5. The rest of the detections for the 50 m, 35 m, and 20 m telescopes are less than 5σ and bottom out near 1.1σ. The data for each model and the corresponding SNRs are located in Table B.9.

Figure 3-11 plots the transmissivity spectra for chosen atmospheric abundances of PH_3. In each subfigure, the diminishing effect of absorption at lower atmospheric abundances is seen. Furthermore, the different abundances in each plot overlap at certain regions. This is especially important between $2 - 4$ μm as it demonstrates the effect of water. One can then see how the 2.95 μm phosphine feature overlaps with the nearby water feature. By comparing the plotted PH_3 abundances, one can notice why the phosphine abundance has to be above a certain level in order for the 2.95 μm feature to be discernible from the water profile. Note that if the water abundance is increased, it may become increasingly difficult to discern the 2.95 μm phosphine feature in the transmissivity spectrum. Luckily, the second phosphine feature (4.45 μm) shows a much stronger profile at lower abundances. The potential low abundance

detection is demonstrated by the 100 ppm and 10 ppm spectral profiles for the 100 m telescope and the 100 ppm spectral profile for the 50 m and 35 m telescopes. In the 20 m telescope subfigure (Fig. 3-11d), the 100% profile is only accompanied by the 10 ppm profile in order to demonstrate how the water profile covers any phosphine contribution near 2.95 μm while also demonstrating the lowest phosphine atmospheric abundance in which the 4.45 μm feature can be distinguished from the water profile. When combining all of the results together, it is clear that the 2.95 μm feature provides better SNRs, but only for larger atmospheric abundances, while the 4.45 μm feature provides the opportunity to probe lower atmospheric abundances, but returns lower SNRs in the process.

3.5.10 Sulfur Dioxide

Five features appear in the IR spectrum for SO_2; however, the one located at 2.45 μm overlaps with a water feature and thus is not the most appropriate feature for a dectability analysis that includes water. The four remaining features are located at approximately 3.65, 4.05, 7.45, and 8.45 μm. The 3.65 and 4.05 μm features are quite narrow which makes them easier to analyze. The last two features (7.45 and 8.45 μm) are much broader and thus the deepest absorption within these features sometimes varies between bins. I have used my experience to choose the proper wavelengths at which to analyze each feature.

The 4.05 μm feature is stronger than the 3.65 μm feature. The difference in strength is noticed either by looking at the transmissivity spectra (see Fig. 3-12) or by simply comparing the SNRs for the second feature as compared to the first (see Table B.10). In fact, the 20 m telescope is even able to attain 5σ detections for some of the models for the 4.05 μm feature. The 4.05 μm feature can be used to probe lower atmospheric abundances of SO_2. The 100 m, 50 m, and 35 m telescopes can detect 10 ppm of SO_2 at a 6.3σ, 4.1σ, and 2.9σ level, respectively. The 20 m telescope can detect a 100 ppm SO_2 atmosphere at a 2.8σ level for the 4.05 μm feature. In comparison, for the 3.65 μm feature, the 100 m, 50 m, and 35 m telescopes can only detect SO_2 if its atmospheric abundance is equal to or larger than 1000 ppm while

the 20 m telescope requires an atmospheric abundance equal to or larger than 1%. Even though the 4.05 μm feature may be a slightly easier feature for detection, the SNRs of the 3.65 μm feature, for many of the modeled atmospheric abundances, are respectfully high and thus the 3.65 μm will still prove valuable for studies that desire the detection of multiple molecular features for spectral identification.

The last two features (7.45 and 8.45 μm) are broader by spanning approximately 0.75 μm and 2 μm, respectively. For larger telescope sizes (100 m and 50 m), these two features can be probed down to atmospheric abundances of 10 ppm with SNRs ranging from $1.8 - 4.4$. Interestingly, the 35 m telescope can probe the 8.45 μm feature down to atmospheric abundances of 10 ppm at a 2.1σ level, but only down to 1000 ppm for the 7.45 μm feature with a detection of 4σ. Unfortunately, the 20 m telescope does not perform higher than a 2.4σ level for either of these features. The data for each model and the calculated SNR for each feature is listed in Table B.10.

Figure 3-12 plots the transmissivity spectra for each telescope size for chosen atmospheric abundances. Each subfigure demonstrates how the absorption weakens with decreasing atmospheric abundance for each particular feature and telescope size. Figures 3-6a−d depict the 3.65 and 4.05 μm features at a resolution of 0.1 μm, while Figures 3-6e−h depict the 7.5 and 8.45 μm features at a resolution of 0.2 μm. For Figures 3-12a−c, within the 3.65 μm feature, the 10 ppm profile demonstrates the absorption due to water (i.e. therefore no SO_2 signature), while, within the 4.05 μm feature, the 10 ppm profile demonstrates the lowest abundance at which that feature is discernible from the water absorption. Similarly, for figure 3-12d, the 100 ppm profile demonstrates the 1% water absorption for the 3.65 μm feature (i.e. no detectable SO_2 feature) while it also demonstrates the lowest abundace at which the 4.05 μm feature can be detected. For Figures 3-12e and f, the 10 ppm profile shows the lowest abundace for which the 7.45 and 8.45 μm features are discernible from the continuum while the other abundances demonstrate how the absorption weakens for lower atmospheric abundances. In Fig. 3-12g, the 1000 ppm profile shows an example of a lower abundance profile than the comparison 100% profile.

Though Fig. 3-12h is similar to Fig. 3-12g in terms of the reference abundances,

a short discussion must occur concerning Fig. 3-12h. The bin centered near 8.65 μm technically has a transmissivity value lower than zero. The negative transmissivity value is an artifact resulting from the noise generation which randomly samples a gaussian distribution during the calculation process. Statistically, for a very small number of wavelengths, the sampling will choose a value far away from the statistical median of the distribution. These farther away values, when sampled, provide much larger values for the synthetic noise than the norm. This effect is seen for the 8.65 μm bin in Fig. 3-12h and for some of the other bins (in other models) which have unrealistically small or large values compared to the continuum (e.g., bins whose transmissivity is much greater than unity). I have used my experience to deduce when such occasions occur and have made sure not to use those particular bins as the wavelength chosen to measure a feature nor as the chosen continuum from which to compare the feature for proper SNR determination. These artifacts can be limited by increasing the number of trials in the Monte Carlo method used to introduce the synthetic noise. By increasing the number of trials in the Monte Carlo method, these infrequent occurences will be averaged out and not noticeable in end data.

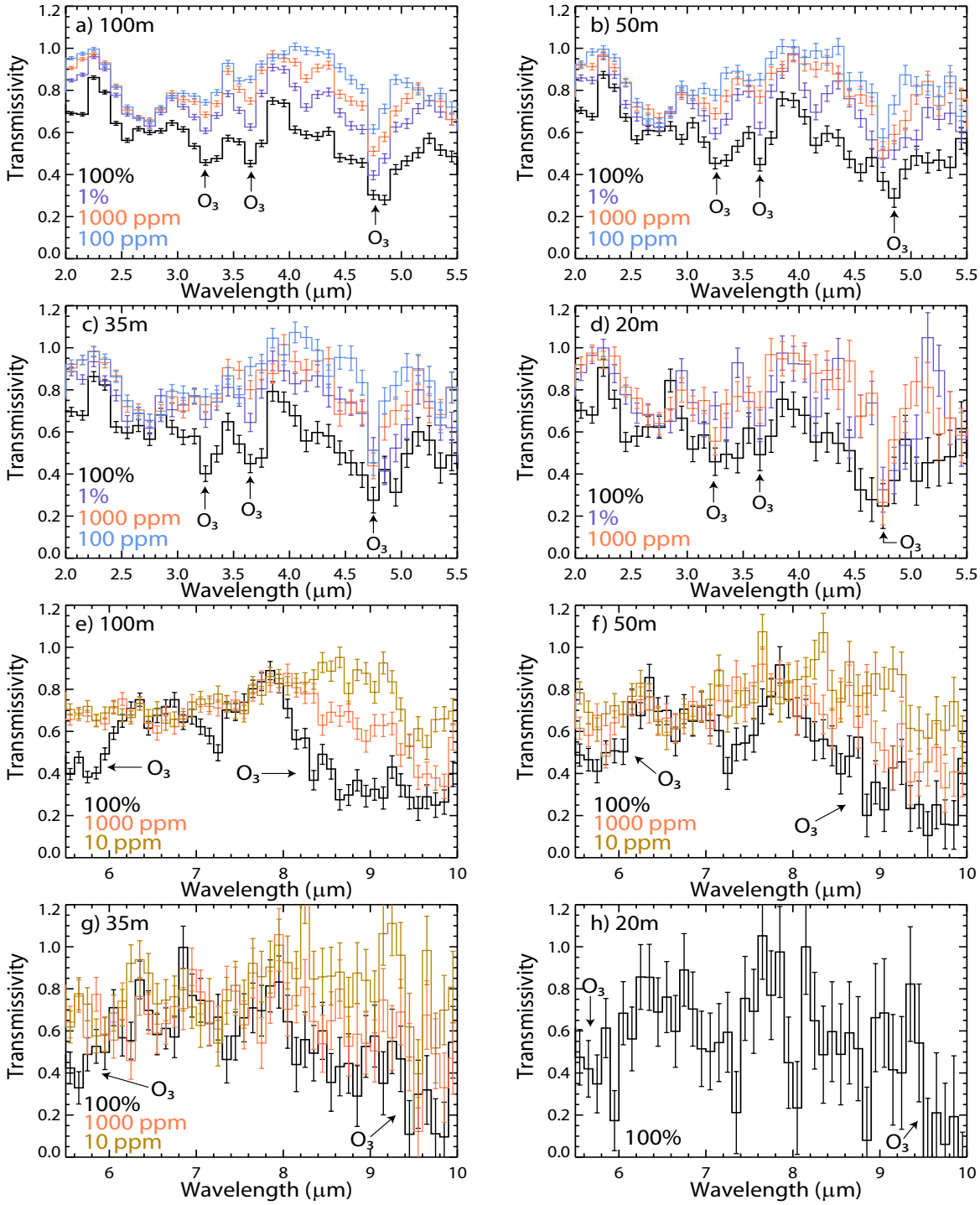

Figure 3-4: Ozone: These figures depict the IR transmissivity spectra (modeled within 20% of the shot noise) for varying ozone abundances along with a 1% atmospheric water contribution for a source (orbiting a Sun-like star) located at 35.45 parsecs and observed for 100 hours. These transmissivity spectra are representative of an 86 km annulus surrounding a planet with a radius equal to Earth's radius. The first four subfigures zoom in on the three ozone features located between 2 and 5.5 μm while the last four subfigures focus on the two features located between 5.5 and 10 μm. The bin size is 0.1 μm for all subfigures.

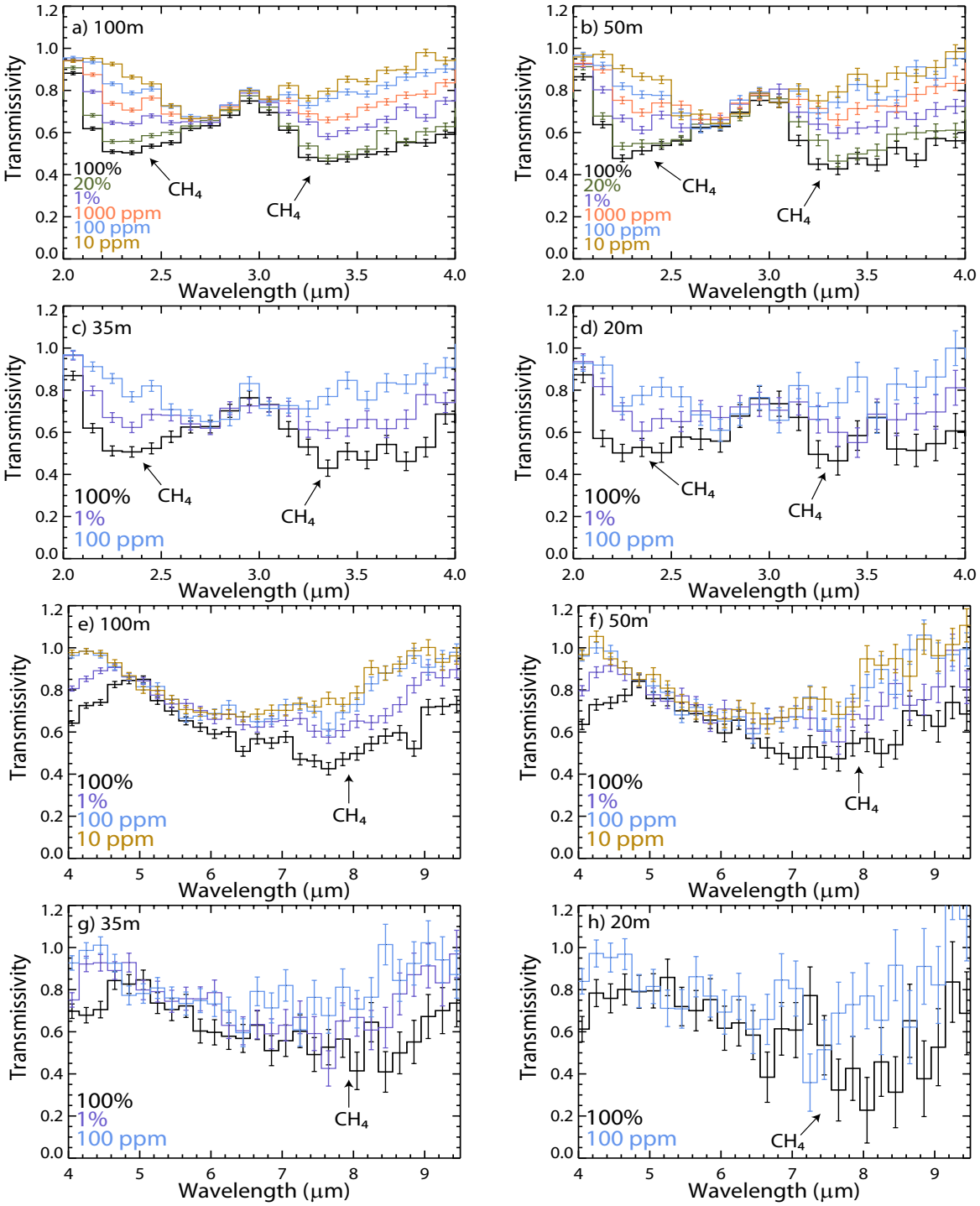

Figure 3-5: Methane: These figures depict the IR transmissivity spectra (modeled within 20% of the shot noise) for varying methane abundances along with a 1% atmospheric water contribution for a source (orbiting a Sun-like star) located at 35.45 parsecs and observed for 100 hours. These transmissivity spectra are representative of an 86 km annulus surrounding a planet with a radius equal to Earth's radius. The first four subfigures zoom in on two methane features located between 2 and 4 μm while the last four subfigures focus on the methane feature located near 8 μm. The bin size for plots a-d is 0.1 μm, and the bin size for plots e-h is 0.2 μm.

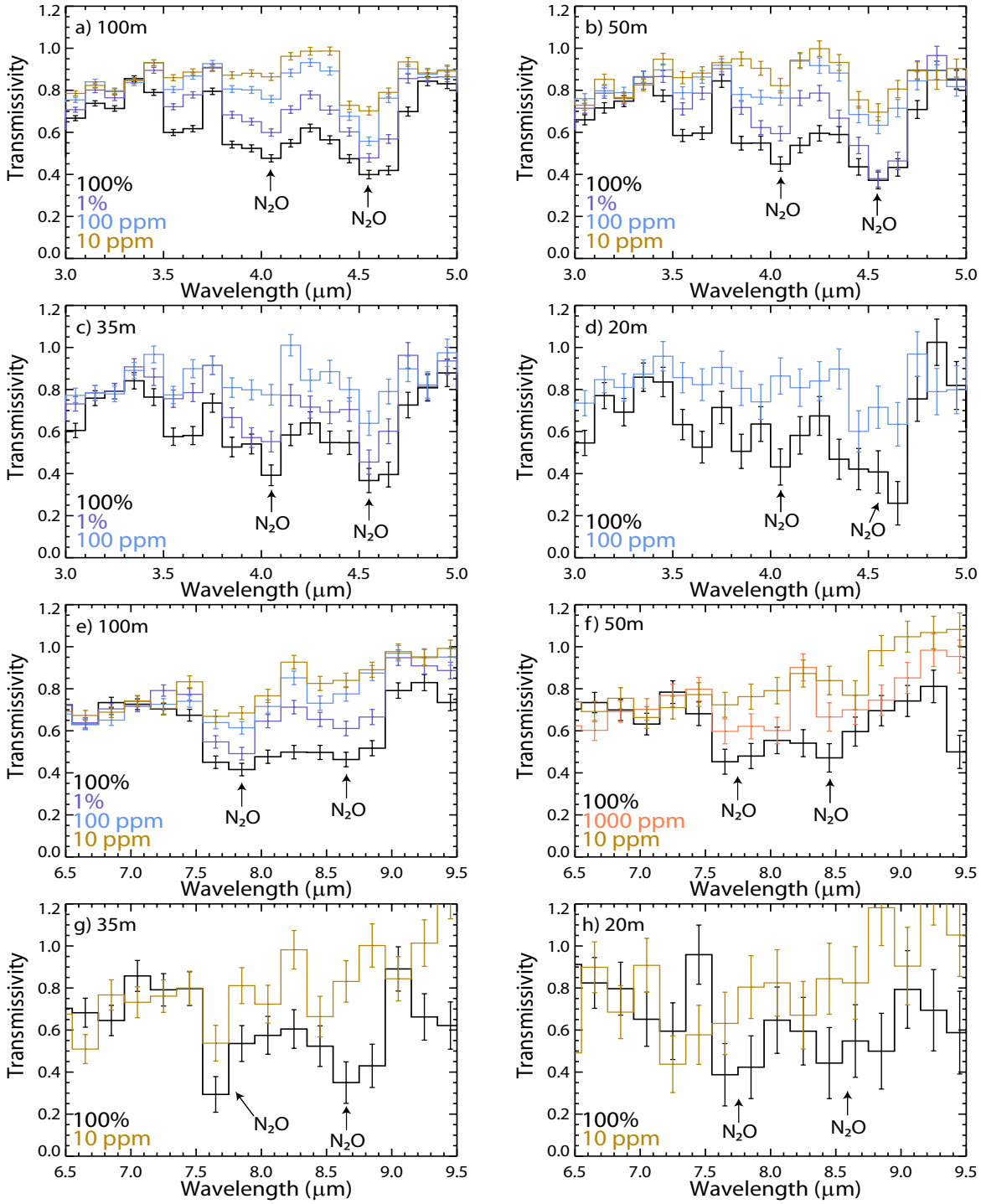

Figure 3-6: Nitrous Oxide: These figures depict the IR transmissivity spectra (modeled within 20% of the shot noise) for varying nitrous oxide abundances along with a 1% atmospheric water contribution for a source (orbiting a Sun-like star) located at 35.45 parsecs and observed for 100 hours. These transmissivity spectra are representative of an 86 km annulus surrounding a planet with a radius equal to Earth's radius. The first four subfigures zoom in on two nitrous oxide features located between 3 and 5 μm while the last four subfigures focus on the two features located between 6.5 and 9.5 μm. The bin size for plots a-d is 0.1 μm, and the bin size for plots e-h is 0.2 μm.

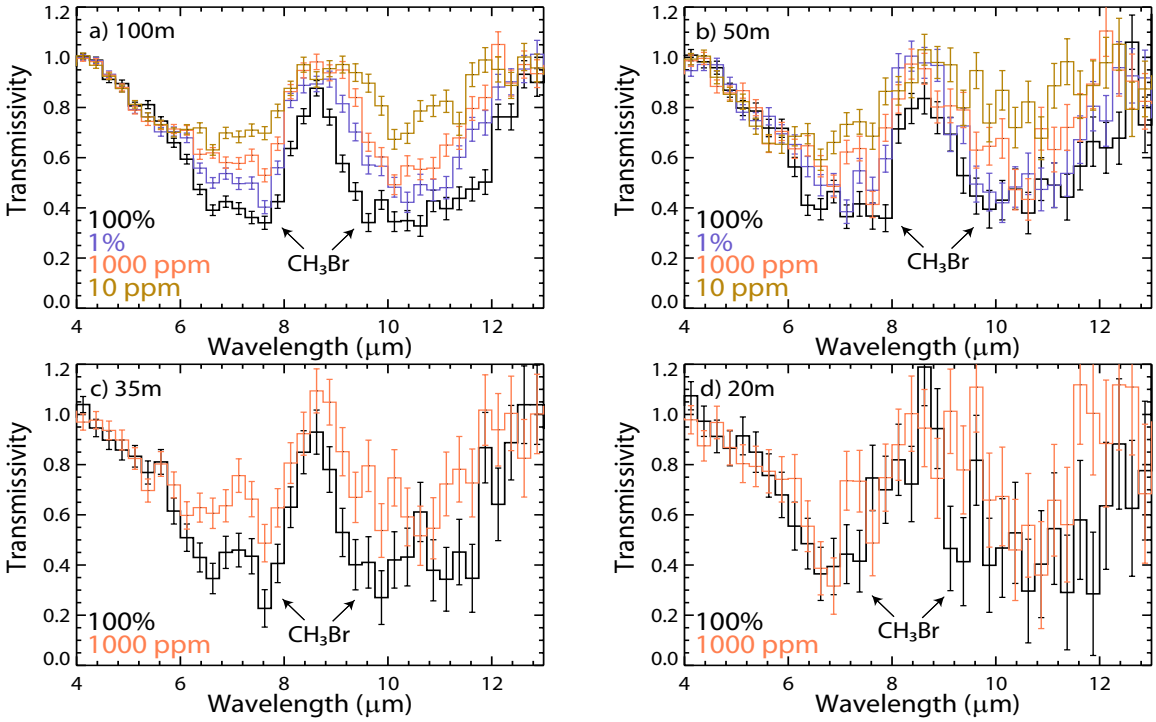

Figure 3-7: Methyl Bromide: These figures depict the IR transmissivity spectra (modeled within 20% of the shot noise) for varying methyl bromide abundances along with a 1% atmospheric water contribution for a source (orbiting a Sun-like star) located at 35.45 parsecs and observed for 100 hours. These transmissivity spectra are representative of an 86 km annulus surrounding a planet with a radius equal to Earth's radius. The two features occur near 7 and 11 μm and are marked in the subfigures. The bin size for plots a-d is 0.25 μm.

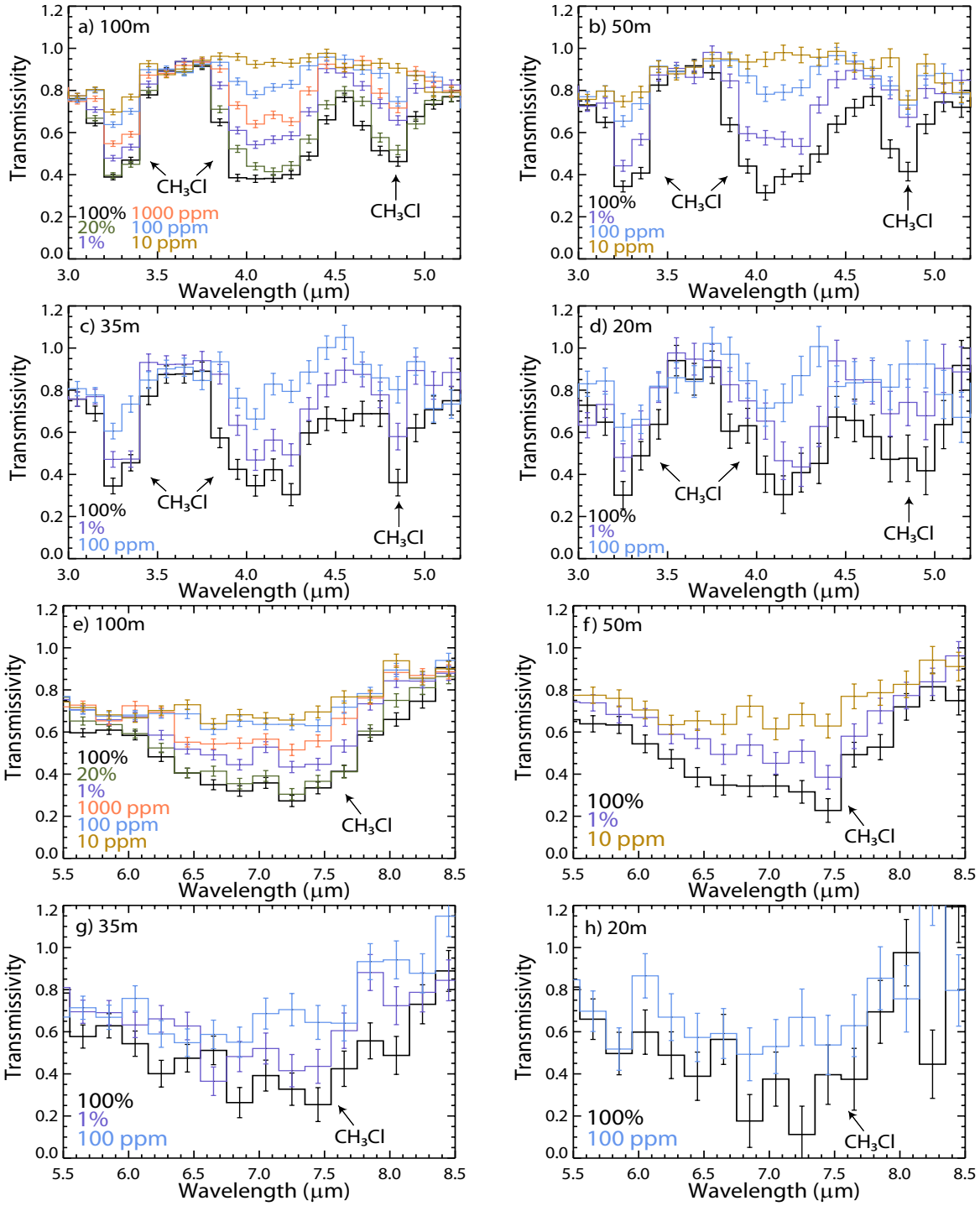

Figure 3-8: Methyl Chloride: These figures depict the IR transmissivity spectra (modeled within 20% of the shot noise) for varying methyl chloride abundances along with a 1% atmospheric water contribution for a source (orbiting a Sun-like star) located at 35.45 parsecs and observed for 100 hours. These transmissivity spectra are representative of an 86 km annulus surrounding a planet with a radius equal to Earth's radius. The first four subfigures zoom in on the three methyl chloride features located between 3 and 5.2 μm while the last four subfigures focus on the feature located between 5.5 and 8.5 μm. The bin size for plots a-d is 0.1 μm, and the bin size for plots e-h is 0.2 μm.

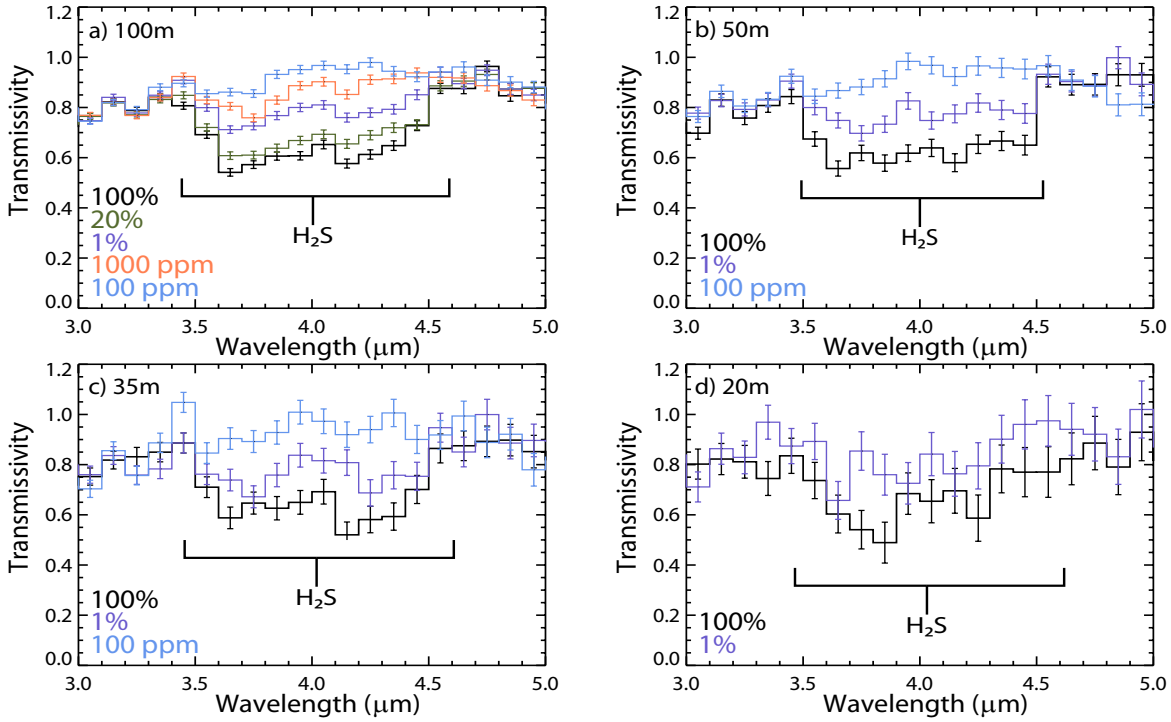

Figure 3-9: Hydrogen Sulfide: These figures depict the IR transmissivity spectra (modeled within 20% of the shot noise) for varying hydrogen sulfide abundances along with a 1% atmospheric water contribution for a source (orbiting a Sun-like star) located at 35.45 parsecs and observed for 100 hours. These transmissivity spectra are representative of an 86 km annulus surrounding a planet with a radius equal to Earth's radius. The four subfigures zoom in on the hydrogen sulfide absorption between 3.5 and 4.5 μm. The bin size for plots a-d is 0.1 μm.

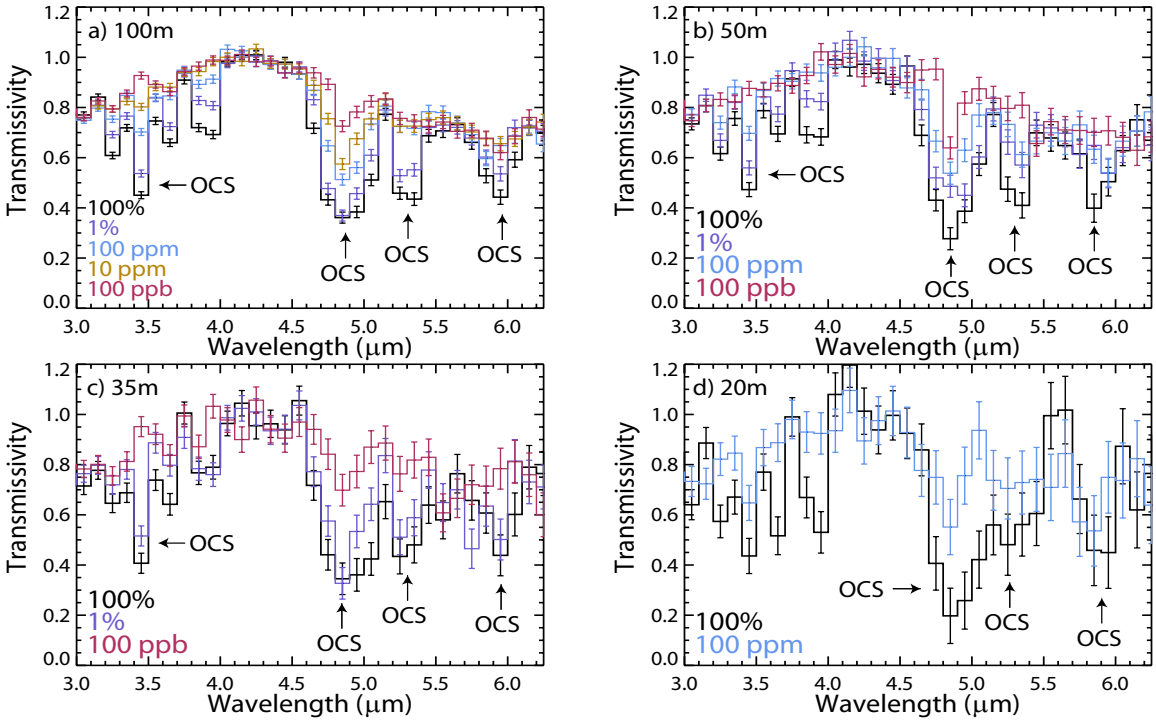

Figure 3-10: Carbonyl Sulfide: These figures depict the IR transmissivity spectra (modeled within 20% of the shot noise) for varying carbonyl sulfide abundances along with a 1% atmospheric water contribution for a source (orbiting a Sun-like star) located at 35.45 parsecs and observed for 100 hours. These transmissivity spectra are representative of an 86 km annulus surrounding a planet with a radius equal to Earth's radius. The four analyzed features are denoted in each subfigure. The bin size for plots a-d is 0.1 μm.

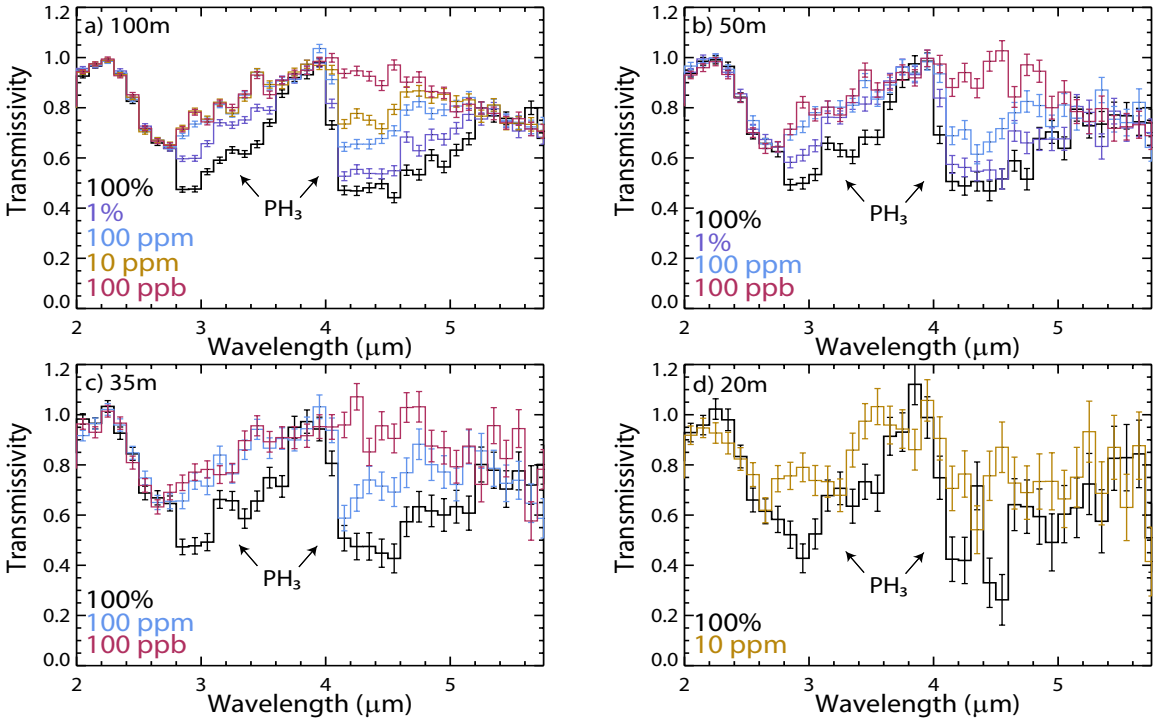

Figure 3-11: Phosphine: These figures depict the IR transmissivity spectra (modeled within 20% of the shot noise) for varying phosphine abundances along with a 1% atmospheric water contribution for a source (orbiting a Sun-like star) located at 35.45 parsecs and observed for 100 hours. These transmissivity spectra are representative of an 86 km annulus surrounding a planet with a radius equal to Earth's radius. The bin size for plots a-d is 0.1 μm.

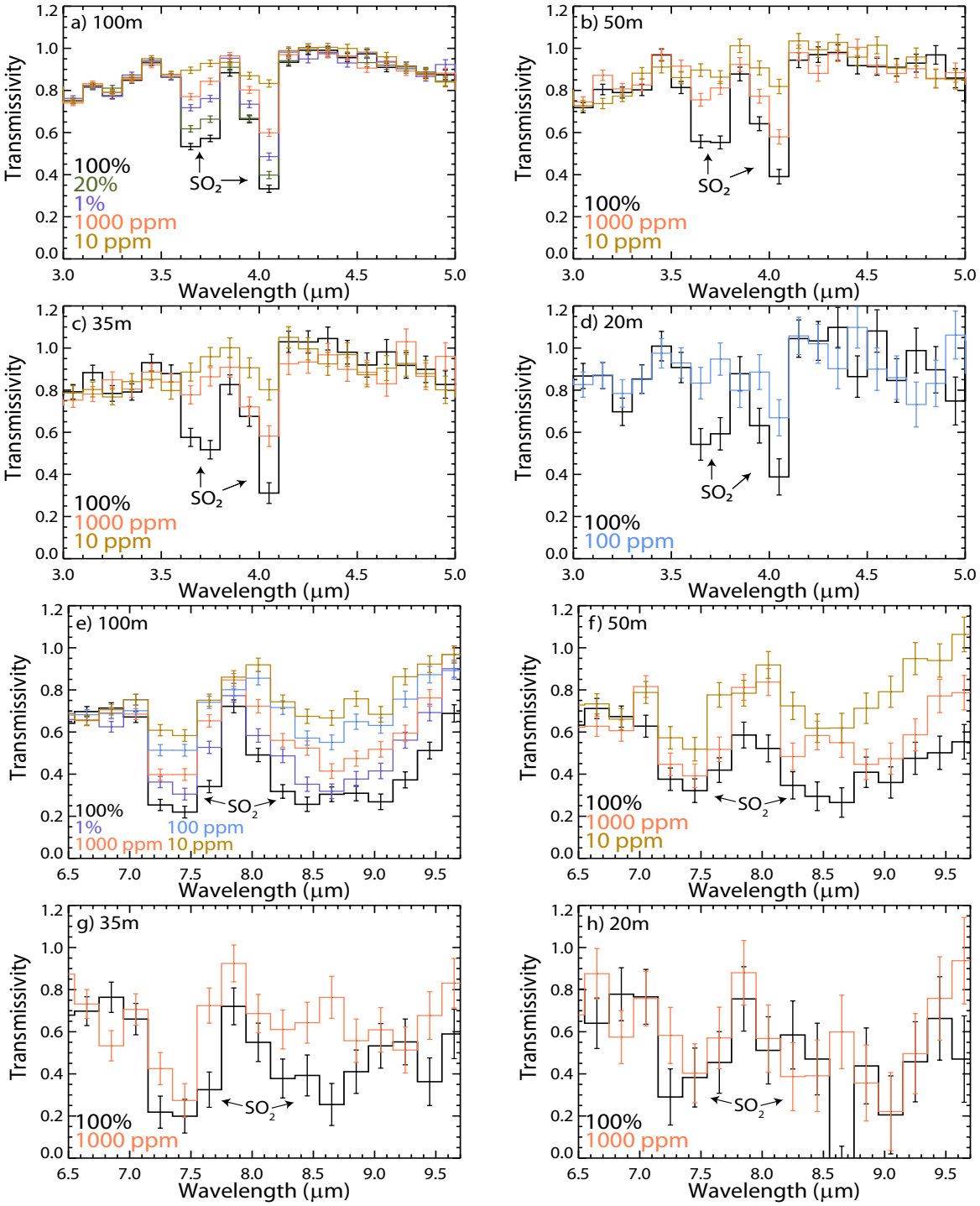

Figure 3-12: Sulfur Dioxide: These figures depict the IR transmissivity spectra (modeled within 20% of the shot noise) for varying sulfur dioxide abundances along with a 1% atmospheric water contribution for a source (orbiting a Sun-like star) located at 35.45 parsecs and observed for 100 hours. These transmissivity spectra are representative of an 86 km annulus surrounding a planet with a radius equal to Earth's radius. The first four subfigures zoom in on the two sulfur dioxide features located between 3 and 5 μm while the last four subfigures focus on the two features located between 6.5 and 9.5 μm. The bin size for plots a-d is 0.1 μm, and the bin size for plots e-h is 0.2 μm

Chapter 4

Discussion

4.1 Detectability at the 10σ level

For reference, I have summarized in Table 4.1 the locations of the HITRAN biosignature gas spectral features of interest that were discussed in Chapter 3.

Table 4.1: Analyzed HITRAN Biosignature Gas Features

Molecule	Feature(s)
O_2	0.765 μm
O_3	3.25, 3.65, 4.75, 5.75, 9.65 μm
CH_4	2.35, 3.35, 7.85 μm
N_2O	4.05, 4.55, 7.85, 8.65 μm
CH_3Br	7, 11 μm
CH_3Cl	3.25, 4.05, 4.85, 7.25 μm
H_2S	2.6, 4, 8 μm
OCS	3.45, 4.85, 5.25, 5.85 μm
PH_3	2.95, 4.45, 9 μm
SO_2	3.65, 4.05, 7.45, 8.45 μm

In Chapter 3, I presented the HITRAN biosignature gases such that other researchers can determine the detectability of a particular gas based on their own preferred value for the SNR. Here, I will stick to my 10σ criteria for detectability as previously described and summarize what gases are detectable given the 10σ criteria.

The only gas from which no modeled abundance or telescope size fit the 10σ detection limit is O_2. The lack of a 10σ detection for O_2 is not that surprising given that only one O_2 feature appears in the models and since O_2 has not previously proven

to be a strong absorber. Luckily, O_3 lines saturate for very low concentrations of O_2 and thus can act as a tracer for O_2; therefore, the failure for O_2 to meet the 10σ criteria is not a game-changer.

The other nine HITRAN biosignature gases can be detected above a 10σ level for at least one of their features with the 100 m telescope. While a 100 m space telescope is quite a long way from production (likely beyond our lifetimes), the 100 m telescope's results demonstrate the fruitful observational opportunities for a telescope of the 100 m size. As I decrease to more realistic telescope sizes, it becomes apparent that ozone and hydrogen sulfide are not detected above a 10σ level for any atmospheric abundance with the 50 m, 35 m, and 20 m telescopes. However, the other seven HITRAN biosignature gases have at least one feature with a 10σ detection (for at least one atmospheric abundance) for the 50 m telescope. The only HITRAN biosignature gases that produce above a 10σ detection for a 35 m telescope are CH_4, CH_3Cl, OCS, and SO_2. The 20 m telescope does not produce a 10σ detection for any HITRAN biosignature gas. The above results from each telescope size demonstrate that, for a 10σ level of detection, a 35 m telescope is essential. However, the 35 m telescope only opens the opportunity to detect a few of the HITRAN biosignature gases, thus a 50 m class telescope may actually be required if one wants to detect the additional HITRAN gases at a 10σ level (with the exception of oxygen, ozone, and hydrogen sulfide).

4.2 Earth at 35.45 Parsecs

After the detailed individual analysis of each HITRAN biosignature gas in Chapter 3, the next natural step is to combine all HITRAN biosignature gases together to determine the IR transmissivity spectra from an Earth-like atmosphere on an Earth-sized planet orbiting a Sun-like star located at a distance of 35.45 parsecs with 100 hours of observation for the 100 m, 50 m, 35 m, and 20 m telescopes. In order to model the Earth's current atmosphere, I have chosen globally averaged atmospheric abundances for each HITRAN biosignature gas (see Table 4.2). In addition to the

HITRAN biosignature gases, I included the standard 1% water profile in the analysis.

Table 4.2: Abundances of HITRAN Biosignature Gases on Earth

Molecule	Mixing Ratio	Source
O_2	20%	
O_3	8.2 ppm	Brasseur and Solomon (2005)
CH_4	1.745 ppm	Seinfeld and Pandis (2006)
N_2O	315 ppb	Seinfeld and Pandis (2006)
CH_3Br	10 ppt	Brasseur and Solomon (2005)
CH_3Cl	600 ppt	Brasseur and Solomon (2005)
H_2S	13 ppt	Seinfeld and Pandis (2006)
OCS	500 ppt	Seinfeld and Pandis (2006)
PH_3	14 ppt	Han et al. (2011)
SO_2	200 ppb	Seinfeld and Pandis (2006)

The corresponding transmissivity spectra for the Earth-like atmosphere for varying telescope sizes are shown in Fig. 4-1. Due to the relatively low atmospheric abundances of many of the biosignature gases (CH_3Cl, OCS, etc.) in Earth's atmosphere, the features resulting from the low abundance gases remain hidden while only the features from more abundant gases (e.g., O_3, N_2O, and CH_4) can be seen. From Fig. 4-1, it is clear that water could be detected in many of the spectra. Unfortunately, the spectral features from N_2O, O_3, and CH_4 are harder to discern. The 4.5 μm N_2O and the 4.8 μm O_3 features are likely to be blended (as depicted in Fig. 4-1b−d) for telescopes smaller than 100 m, though higher resolution observations may allow for the two features to be disentangled. The combined absorption from methane and nitrous oxide near $7 - 8$ μm will likely be very difficult to separate from the water profile, especially if the exoplanet's atmospheric water concentration is larger than the globally averaged 1% used for this model. The 9.6 μm ozone feature does hold some promise, but does not appear to be detectable with a high SNR as seen in Figs. 4-1e−h.

The above results indicate that, for an Earth-like atmosphere on a Earth-size planet orbiting a Sun-like star located at a distance of 35.45 parsecs and observed for 100 hours, while we should be able to detect absorption separate from that of a water profile, we will likely encounter significant difficulty identifying the species responsible for the "extra" absorptions due to the weakness of the absorption and the blending of the spectral features. Higher resolution observations and increased

signal will help in differentiating spectral features of different gases. Alternatively, increased atmospheric abundances for the HITRAN biosignature gases would help them become more visible over the water profile. While the abundances of the HITRAN biosignature gases included in the Earth-like model are representative of the current atmosphere of the Earth, it is possible for the gases to attain higher (thus more detectable) abundances on near-Earth-like exoplanets. Discussion concerning the atmospheric abundances required for the HITRAN biosignature gases to be detectable can be found in Chapter 3.

4.3 Comparison to Previous Models

As different physics govern scattering, thermal emission, and transmission/transmissivity radiative transfer, the results presented in my transmissivity radiative transfer study can only be compared to other studies that model transmission/transmissivity radiative transfer. The first of the transmission studies that was introduced in Section 1.4.4 is Ehrenreich et al. (2006). The available comparability between my study and their study is limited since my work did not have much input data in their wavelength region ($200 - 2000$ nm). One of the most important differences is that Ehrenreich et al. (2006) predict that the oxygen A-band feature at 760 nm is not detectable in their study; however, my models indicate that the 760 nm O_2 feature is distinguishable from the continuum (see Sections 3.5.1 and B.1 for further details). Their reasoning for the O_2 feature not appearing is due to the narrowness of the band in relation to the 10 nm wavelength binning they use; however, my study utilizes a similar 10 nm binning and it is noticed the oxygen A-band is not necessarily "too thin" as the absorption is seen in my models. One potential explanation for the discrepancy between the two studies is due to their models including the presence of clouds which effectively act to increase the radius of the planet since they are optically thick. If the majority of the oxygen absorption in my model occurs below their 10 km cloud deck, then our results are not necessarily in disagreement; rather, we are just modeling slightly different atmospheres.

Though Kaltenegger and Traub (2009) present results for a larger wavelength range ($0.3 - 20$ μm) than I have presented in my work (i.e. $0.3 - 10$ μm for most cases), the main difference between the two studies is the molecular features investigated. Kaltenegger and Traub (2009) only focus on the "main" spectral feature of each molecule and conclude that the near-IR may show methane absorption while the mid-IR shows ozone and methane absorption. As seen from Section 3.5 and the appendix, many more ozone and methane features have the opportunity to be detectable, especially when considering higher concentrations of those gases as compared to their present-day abundances in Earth's atmosphere. Therefore, while their examination of the main spectral feature for each gas is very valuable, they do not explain the full investigative parameter space for the detectability of these molecules similar to that included in the current work. My analysis, which investigates alternative spectral features for each gas, predicts the potential detection of nitrous oxide in addition to methane and ozone (further details can be found in Section 4.2). Despite the limitation due to focusing only on major spectral features, their study is still extremely valuable as it explores alternative avenues (e.g., detectability of spectral features in M star environments) not detailed in this work.

4.4 Caveats

In the following subsections, I discuss a few caveats to keep in mind when considering the conclusions of my results. The following discussion both provides perspective on general parameters affecting the conclusions and illuminates additional intricacies of the modeling.

4.4.1 Modeling only one Gaussian Distribution in Eq. (2.27)

I only model one Gaussian distribution (i.e. one β) in Eq. (2.27) for each atmospheric model. Therefore, since the values for β are selected randomly from a Gaussian distribution, some wavelength bins may receive a β value on the wings of the Gaussian profile. By running only one β trial, any abnormally large β values will misrepresent

(on a statistical scale) the perturbation of the binned transmissivity by the noise σ_{binned}. An example of such an occurance is described in Section 3.5.10. Much effort was taken not to base any detectivity calculations on wavelength bins where abnormally large β values were expected to occur; therefore, the influence from larger β values does not affect the conclusions of this study. Future studies should model thousands of β values for every wavelength of every atmospheric model. Those studies will then have more robust results and avoid the β caveat.

4.4.2 Water Profile

In my radiative transfer analysis, the combination of the 1% water profile with the varying biosignature gas abundances provides a couple interesting caveats. First, for the biosignature gas features that overlap significantly with the water profile, I have often discussed how the biosignature gas is discernible in the spectra for higher atmospheric abundances. However, the associated SNRs presented in the data tables are actually representative of the combination of the biosignature gas and the water absorption if the two molecular features happen to overlap at the measured wavelength. The actual SNR for the biosignature gas may be slightly less than that of the biosignature gas + water. This study does not attempt to disentangle the SNRs for the individual gases, but rather makes apparent in Chapter 3 the severity of the overlap and preferentially investigates features that are less impacted by the water absorption profile.

The second caveat is that my models only investigate the effect due to a 1% atmospheric water absorption contribution. As alluded to in previous sections, an increase or decrease in the atmospheric water abundance would lead to an increased or decreased impact of water on the total modeled spectra, respectively. Thus, for the biosignature gas features that I claimed were discernible at higher atmospheric abundances despite the fact that they overlap with water, they may actually become masked if the atmospheric water abundance is increased or much more apparent at lower biosignature gas abundances if the water abundance is decreased. Variation of the water abundance is beyond the scope of my study, but must be kept in mind if

one is trying to extrapolate the effect of water absorption from the results presented in my work.

4.4.3 Potential Spectral Feature Blending for Biosignature Gases

From the transmissivity spectra plotted for each HITRAN biosignature gas, it is apparent that many of the gases have broadband features in the long-wavelength IR ($6 - 10\ \mu$m). If one detects such a broad feature (without distinct absorption peaks) in observational data then it may prove quite difficult to determine which of the modeled HITRAN biosignature gases (or possibly alternative species that were not modeled) is responsible for such a broad signal. In fact, the signal may result from a combination of many gases. The exact abundances of each gas associated with the combination is anticipated to fill quite a large degeneracy space and thus be difficult to disentangle. Therefore, it may prove more beneficial to target narrower spectral features that can be easily separated from the spectral features of other gases. Furthermore, in any observation searching for biosignature gases, it will prove very useful for the study to search multiple wavelength bands for identification of the molecule in question. If absorption occurs at the proper locations within the absorption bands for the molecule in question, it may prove difficult to attribute the absorption to any other molecule besides the one being targeted. However, there would likely exist some degeneracy if one includes enough alternate molecules to individually cover the different absorptions from the multiple measured bands, though Occam's razor would still point to the original molecule being responsible for the absorption from all of the spectral bands.

4.5 Noise Reduction: The Interplay between Telescope Size and Observation Time

The battle for decreasing the noise budget involves efforts to increase the number of photons observed. The two best options for increasing the number of observed

photons are to either increase the telescope size and/or increase the observational time. The potential exchangability between telescope aperture size and observation time has warranted an investigation into this topic. The basic idea being currently contemplated is whether increasing the observation time for a smaller telescope will allow for an equal level of detection as compared to a larger telescope with a shorter observational time. The reasoning for this analysis is that smaller telescopes ($<$ 35m) are easier and more affordable to build as well as being within our near-future technological reach. Therefore, pointing them at targets for longer periods of time will likely prove much more financially realistic than trying to build an extremely large ($>$ 35m) telescope. For reference, the *JWST* costs an estimated 10 billion dollars to produce. Undeniably, a 50 m and 100 m telescope would cost significantly more than 10 billion dollars and thus is not possible given the current economic situation (especially in the United States) and current state-of-the-art technology.

The exact interchange between telescope size and observational duration is not one-to-one. The connection between the two parameters is noticed through Eq. (2.19) which calculates the total energy observed given a particular telescope aperture size, observational duration, etc. The effect from the telescope aperture is stronger due to its contribution being squared in comparison to the observation time. However, an increase in observational time still decreases the shot noise.

In order to further investigate the connection between telescope size and observation time, I use ozone as the case study. The following investigation utilizes a 35 m telescope to model an atmosphere consisting of 20% ozone and 1% water for three observation durations: (1) 100 hours, (2) 1000 hours, and (3) 10,000 hours. For reference, the models presented in Section 3.5 assumed 100 hours of observation time. Figure 4-2 shows the transmissivity spectra for these three models (100 hours, 1000 hours, and 10,000 hours). From this figure, it is seen that the increase to 1000 and 10,000 hours of observational time provides for the features to be much more discernible and raises their detectability. In fact, for the 4.75 O_3 μm feature, the SNR raises to 20.8 and 62.5, for the 1000 and 10,000 hour observations, respectively (for reference, the SNR for the 100 hour model is 5.6). These new SNRs far surpass my

10σ limit for detectability.

With such a large increase in discernability for the 35 m telescope, one might begin to ponder what could be done for a smaller telescope aperture. I reintroduce the 6 m telescope here. While I disregarded the 6 m telescope previously in this study, an increase in observation time may allow for the 6 m telescope to be successful in detecting biosignature gases. For the 6 m model, I utilize the same atmosphere as for the 35 m telescope investigation above. Figure 4-3 shows the transmissivity spectra for the 6 m telescope for 100 hours, 1000 hours, and 10,000 hours of observation time. Figure 4-3a clearly shows the non-detectability of spectral features for 100 hours of observation time[1]; however, the discernability appears much better in Figs. 4-3b and c. For these two observing times, the 4.75μm O_3 feature goes from indiscernible (for the 100 hour model) to having an SNR equal to 3.2σ and 10.1σ for the 1000 and 10,000 hour models, respectively.

Though these increases in observation time for the 6 m telescope allow for the feature to be more discernible than the 100 hour case, the 6 m telescope still falters due to the following detail. One may think that the 1000 hour and 10,000 hour observation times are not necessarily "that" long, especially if the golden egg laying at the end is the detection of the popular biosignature gas ozone. In fact, these observation times are approximately a mere 42 days and 14 months, respectively. Considering that the *Kepler Space Telescope* is observing the same target area for six years, even the 14 month requirement seems relatively short. The reason that these observation times will not be feasible is that the planet would need to be observed in transit for the entirety of the observation time. In order to meet the requirement of 1000 or 10,000 hours of observation time, a target would need to be observed for hundreds, if not, thousands of transits. For example, if the transit duration for a particular exoplanet is 5 hours, then the planet would need to be observed for 200 transits to meet the 1000 hour observational limit and 2000 transits to meet the 10,000 hour observational limit. Since we only have certain windows of opportunity

[1]I have not marked the ozone absorptions in Fig. 4-3a because the spectral profile is too noisy for features to be discernible.

to observe transits due to the physics of the exoplanet system and the day/night cycle of the observing telescope, observing hundreds of transits for the same object would likely require an amount of time longer than the lifecycle of the telescope itself! For these reasons, it was and is proper to disqualify the 6 m telescope from being able to provide useful biosignature gas detectability for atmospheres similar to that modeled in my study.

A middle ground must be reached between telescope size and observation duration in order for the realization and implementation of the most economically viable solution for remote sensing of exoplanet atmospheres. Appealing to the two constructs is a double-edged sword because though the construction costs for large-scale telescopes increases dramatically with increasing aperture size, the cost of operating the telescope can be quite large as well. Furthermore, unless a particular projected study can guarantee a revolutionary discovery, the study is unlikely to be provided sufficient telescope time to make biosignature detections (for individual case studies) utilizing smaller telescopes like the *JWST*, even if the observational demands presented here could be met for a particular exoplanet. However, if a future telescope/study can meet all of the aforementioned parameters with observations that simultaneously study the atmospheres of a statistically worthwhile number of exoplanets, then the large cost associated with the study may be justifiable, especially if the results characterize thousands of exoplanet atmospheres.

4.6 Observing in the Millimeter Region

As many of the presented molecules have features beyond the IR (as indicated by Fig. 2-4), one may begin to ponder the potential detectability of these alternate regions. Though I previously eliminated these regions in my study due to the resulting low-signal transmissivity data, I now investigate one of the regions further to illuminate the potential technological requirements for observing in these long wavelength regions. As alluded to in Section 4.5, the noise level must be reduced if one is to observe at longer wavelengths. The two presented ways that will produce a stronger

signal are increasing the telescope size and/or increasing the observation time. In order to investigate the requirements to observe in long wavelength regions, I have chosen to examine the longest wavelength region I model, the millimeter, as this region would be the toughest to observe given the low number of incident photons impinging the atmosphere.

As introduced in Section 3.3, a 1000 m telescope with a 100 hour observation time is not enough to resolve features in the millimeter region. In order to determine what technological feats must be accomplished to observe in the millimeter region, I have modeled three telescope sizes (1 km, 10 km, and 50 km) and two observation times (1000 and 10,000 hours) for an atmosphere that contains 20% oxygen and 1% water. The reasoning for choosing oxygen for this case study (as opposed to my typical choice of ozone) is due to oxygen having a distinct feature in the millimeter wavelength region while ozone produces a relatively flat spectrum without any distinguishing features.

Figure 4-4 shows the millimeter transmissivity spectra for telescope sizes of 1 km, 10 km, and 50 km and observational durations of 1000 and 10,000 hours. It becomes quickly apparent that non-realistic telescope sizes are required in order to observe enough photons such that the millimeter spectral features become discernible from the noise. Figure 4-4 demonstrates that a telescope size greater than 1 km is required in order for the oxygen feature to be discernible from the noise. Even for the 10 km telescope, the detectability for the 5 μm O_2 feature is only 4.5σ and 14.5σ for the 1000 hr and 10,000 hr models, respectively. For the 50 km telescope, the detectability greatly improves to 21.4σ and 77.9σ for the 1000 hr and 10,000 hr models, respectively.

Pondering the construction of the 100 m space telescope modeled in Chapter 3 is mind-boggling with the state of the current technology; therefore, the idea of kilometer-sized space telescopes is so far beyond our current technological means that I cannot even begin to predict the number of decades of technological advancement required. Whenever technology reaches severe impasses like that presented here, the door for innovative ideas swings wide open. In order to study long wavelength spectral regions, we must think about the problem in a different way. Since it is much easier to build smaller telescopes, we must determine if we can combine mul-

tiple smaller telescopes to achieve the same observational detectability as one large telescope. The idea of interferometry is not new; however, current studies using interferometry are much more focused on attaining spatial resolution. Although, with current technology, we are unable to spatially resolve an exoplanet. The inability to spatially resolve exoplanets begs to question whether a telescope structure consisting of multiple *JWST*s orbiting directly next to each other would allow for the same observational potential as that of a larger telescope with the same collecting area. If this interferometric technique is possible, then nine *JWST*s aligned in a 3 x 3 matrix would provide for an observing area equal to approximately 300 m^2 of combined dish size. The nine *JWST* setup would provide approximately the same collecting area as a 20 m telescope.[2] Whether a telescope array could be used in this manner is currently uncertain. In order for such a technique to be successful, scientists would need to understand the systematics of each individual telescope in great detail in order to remove these effects and thereby properly combine data from the entire array. Creativity in this manner may be required if we want to better classify exoplanets on an individual scale, and, therefore, I encourage others to help undertake these studies.

4.7 "Non-Standard" Biosignature Gases

4.7.1 Threshold Atmospheric Mixing Ratios required for the detection of Non-Standard Biosignature Gases

The Pacific Northwest National Laboratory (PNNL) database (Sharpe et al. 2004) and the National Institute of Standards and Technology (NIST) Quantitative Infrared database (Chu et al. 1999) contain molecular absorption cross section data for many biosignature gases not included in the HITRAN database; however, since the PNNL/NIST molecular data is only representative of one temperature (296 K) and one pressure (1 atm), difficulty arises in using the data in a way similar to that

[2]Mass production of any product has always reduced the overall cost per unit. Therfore, while one *JWST* costs over 10 billion dollars to produce, the production of replicas would be significantly cheaper per unit and potentially affordable.

detailed in Chapters 2 and 3 because it is currently unknown how to properly map the PNNL/NIST absorption cross sections to different temperatures and pressures. Alternatively, I can estimate the threshold atmospheric mixing ratio(s) required for the detection of PNNL/NIST molecule(s) in the same atmosphere as that modeled for the HITRAN biosignature gases by utilizing an estimation technique involving several pieces of data: (1) the SNR of the reference HITRAN feature, (2) the threshold atmospheric mixing ratio for the reference HITRAN feature for particular model parameters (a 35 m telescope, 100 hours of observation, and a target distance of 35.45 parsecs), (3) the molecular absorption cross section of the reference HITRAN molecule at the wavelength of interest, and (4) the molecular absorption cross section of the PNNL/NIST gas at the wavelength of interest. I applied the PNNL/NIST biosignature gas threshold mixing ratio estimation technique described below to sixteen PNNL/NIST biosignature gases: acetaldehyde, acetone, benzene, carbon disulfide, dimethyl disulfide, dimethyl sulfide, dimethyl sulfoxide, ethanol, ethyl mercaptan (also called methanethiol or ethyl sulfide), fluoroacetone, isoprene, methyl ethyl ketone, methyl mercaptan (also called methyl sulfide), methyl vinyl ketone, thioglycol (also called 2-thioethanol), and toluene. These sixteen biosignature gases were chosen from Seager et al. (2012).

I now describe the theory behind the PNNL/NIST biosignature gas threshold mixing ratio estimation method. The multiplication between a molecular absorption cross section and the atmospheric number density of the corresponding gas gives the absorption coefficient over which that species absorbs in the atmosphere. The detectability of a molecule's spectral features in a transmissivity spectrum is representative of the absorption coefficient of the modeled molecule. If different molecules have the same absorption coefficient, then they will absorb to the same degree in identical atmospheres (i.e. the incoming radiation does not have a preference on which molecule is absorbing). I utilize the connection of equivalent absorption coefficients between two molecules to build the following relation. If the PNNL/NIST biosignature gases listed above have an absorption feature at a wavelength near to a reference HITRAN feature, then I can calculate the atmospheric mixing ratio of the PNNL/NIST biosignature

gas that would represent the same level of detectability by utilizing the following equation:

$$(Threshold)\ Mixing\ Ratio_{PNNL/NIST} = \frac{(Threshold)\ Mixing\ Ratio_{HRG} \cdot \sigma_{HRG}}{\sigma_{PNNL/NIST}}, \tag{4.1}$$

where σ represents the absorption cross section, HRG designates the HITRAN Reference Gas, and PNNL/NIST represents the PNNL/NIST gas being investigated. By plugging in the threshold mixing ratio of the reference HITRAN biosignature gas and the molecular absorption cross sections (at the wavelength of interest) for the reference HITRAN biosignature gas and the PNNL/NIST biosignature gas, I can calculate the threshold mixing ratio for the PNNL/NIST gas that would lead to the same level (i.e. SNR) of detectability.

In order to utilize Eq. (4.1), I searched the absorption cross section profiles of each PNNL/NIST biosignature gas listed above for a promising feature that provides the best opportunity to be discernible from the continuum while also not directly overlapping with any water vapor features. I chose the reference HITRAN biosignature gas for each of the PNNL/NIST gases based on which HITRAN gas had a feature at a similar wavelength as the chosen feature of the PNNL/NIST gas. The feature wavelengths, absorption cross sections, threshold mixing ratios, and SNR of the comparison feature for the reference HITRAN molecules can be found in Table 4.3. The SNRs in Table 4.3 are representative of the transmissivity model described in Chapter 2 for a 35 m telescope, 100 hours of observation, and a target distance of 35.45 parsecs; therefore, the calculated threshold mixing ratios for the PNNL/NIST biosignature gases are representative of the same model parameters. Using the data presented in Table 4.3 and the molecular absorption cross sections from the PNNL/NIST biosignature gases, I determined the threshold mixing ratios [using Eq. (4.1)] required for the PNNL/NIST biosignature gases to be detectable. The PNNL/NIST feature wavelengths, corresponding absorption cross sections, calculated threshold mixing ratios, and corresponding SNRs are listed in Table 4.4.

Based on the estimation technique, the most easily detectable molecules are ethyl

Table 4.3: Comparison HITRAN molecular data used for the calculation of the PNNL/NIST biosignature gas threshold mixing ratios. These data were calculated using the transmissivity radiative transfer model described in Chapter 2 for the following model parameters: a 35 m telescope, 100 hours of observation, and a target distance of 35.45 parsecs.

Molecule	Wavelength (μm)	Absorption Cross Section (cm^2/mol)	Threshold Volume Mixing Ratio	SNR of Threshold Mixing Ratios
CH_4	3.35	1.00 x 10^{-20}	1.00 x 10^{-4}	6
N_2O	4.55	4.93 x 10^{-19}	1.00 x 10^{-3}	5.7
O_3	5.75	2.00 x 10^{-21}	0.01	5.6

mercaptan, ethanol, isoprene, thioglycol, dimethyl sulfide, toluene, and benzene since they all require threshold mixing ratios less than 10 ppm for detection. The next most promising molecules for detection are dimethyl disulfide, dimethyl sulfoxide, fluoroacetone, methyl ethyl ketone, acetone, acetaldehyde, methyl mercaptan, and methyl vinyl ketone which require mixing ratios between $20 - 66$ ppm for detection. The estimations shown in Table 4.4 demonstrate that many of the PNNL/NIST non-standard biosignature gases can provide similar detectability as compared to the more popular biosignature gases (e.g., oxygen, ozone, etc.). Furthermore, the threshold mixing ratios of many of the HITRAN and PNNL/NIST biosignature gases demonstrate that an atmospheric gas will likely require a mixing ratio at least in the ppm range in order to be detectable with a 35 m telescope, 100 hours of observation, and a target distance of 35.45 parsecs. Given the potential for the detectability of the PNNL/NIST biosignature gases, I encourage more work to occur with the gases presented here, especially the development of HITRAN-like spectral data which can be properly mapped to varying temperatures and pressures.

4.7.2 Alternative Wavelengths for the Detection of the Non-Standard Biosignature Gases

One main emphasis in my work is the importance placed on studying multiple spectral features (when possible) for each biosignature gas as opposed to focusing solely on more popular wavelengths. Keeping a similar theme for the PNNL/NIST biosig-

Table 4.4: PNNL/NIST molecular data and threshold mixing ratio estimates for the detection of the PNNL/NIST biosignature gases in the same atmosphere as that modeled for the reference HITRAN gas for a 35 m telescope, 100 hours of observation, and a target distance of 35.45 parsecs

PNNL/NIST Molecule	PNNL/NIST Wavelength (μm)	PNNL/NIST Absorption cross section (cm^2/mol)	PNNL/NIST Threshold Volume Mixing Ratios	Comparison Molecule	SNR of threshold detection
Acetaldehyde	5.72	4.00×10^{-19}	5.00×10^{-5}	O_3	5.6
Acetone	5.75	4.90×10^{-19}	4.08×10^{-5}	O_3	5.6
Benzene	3.26	1.08×10^{-19}	9.26×10^{-6}	CH_4	6.0
Carbon Disulfide	4.6	5.00×10^{-20}	9.86×10^{-3}	N_2O	5.7
Dimethyl Disulfide	3.32	5.00×10^{-20}	2.00×10^{-5}	CH_4	6.0
Dimethyl Sulfide	3.35	1.10×10^{-19}	9.09×10^{-6}	CH_4	6.0
Dimethyl Sulfoxide	3.33	4.72×10^{-20}	2.12×10^{-5}	CH_4	6.0
Ethanol	3.42	1.30×10^{-19}	7.69×10^{-6}	CH_4	6.0
Ethyl Mercaptan	3.35	2.00×10^{-19}	5.00×10^{-6}	CH_4	6.0
Fluoroacetone	3.35	4.08×10^{-20}	2.45×10^{-5}	CH_4	6.0
Isoprene	3.35	1.26×10^{-19}	7.94×10^{-6}	CH_4	6.0
Methyl Ethyl Ketone	5.74	5.00×10^{-19}	4.00×10^{-5}	O_3	5.6
Methyl Mercaptan	3.33	2.00×10^{-20}	5.00×10^{-5}	CH_4	6.0
Methyl Vinyl Ketone	5.81	3.02×10^{-19}	6.62×10^{-5}	O_3	5.6
Thioglycol	3.4	1.15×10^{-19}	8.70×10^{-6}	CH_4	6.0
Toluene	3.4	1.10×10^{-19}	9.09×10^{-6}	CH_4	6.0

nature gases, I have compiled a list of potential wavelengths between 1 and 10 μm where absorption may be seen in transmissivity spectra of the PNNL/NIST biosignature gases (see Table 4.5). These wavelengths were selected through analyzing the molecular absorption cross sections of each PNNL/NIST molecule for wavelengths that have the potential to exhibit absorption features. Without a full transmissivity radiative transfer analysis, the wavelengths presented in Table 4.5 should be taken with caution because it is not fully known whether all of these features would be distinguisable in the end transmissivity spectrum due to several factors: (1) the variation in the strength of the features due to changing temperature and pressure is unknown, (2) the potential blending of features, (3) the severity of spectral masking by water vapor (or other molecules), (4) etc.

Table 4.5: Predicted PNNL/NIST Biosignature Gas Absorption Features between 1 − 10 μm

Biosignature Gas	Potential Features
Acetaldehyde	3.6, 5.72, 7.25, 9 μm
Acetone	3.4, 5.75, 7.3, 8.2, 9 μm
Benzene	3.26, 5, 5.5, 6.8, 9.6 μm
Carbon Disulfide	4.3, 4.6, 6.5 μm
Dimethyl Disulfide	3.32, 6.95, 7.5 μm
Dimethyl Sulfide	3.35, 6.95, 7.5, 9.6 μm
Dimethyl Sulfoxide	3.33, 7, 7.6, 9, 9.9 μm
Ethanol	3.42, 7.2, 8.1, 9.3 μm
Ethyl Mercaptan	3.35, 6.9, 7.9, 9.1, 10 μm
Fluoroacetone	3.35, 5.7, 6.9, 7.2, 8.1, 9.3 μm
Isoprene	3.35, 5.5, 6.2, 7, 9.3, 10 μm
Methyl Ethyl Ketone	3.3, 5.74, 6.9, 7.3, 8.5 μm
Methyl Mercaptan	3.33, 3.8, 6.8, 7.4, 9 μm
Methyl Vinyl Ketone	3.2, 5.81, 7.2, 8, 8.4 μm
Thioglycol	2.7, 3.4, 7.1, 7.6, 8.3, 9.2 μm
Toluene	3.4, 5.4, 6.1, 6.6, 9.2, 9.6 μm

4.8 Future Work

In the following sections, I describe future work opportunities to further the study of remote sensing of biosignature gases.

4.8.1 Additional Sources and Spectral Data

Future remote sensing studies would greatly benefit from the development of molecular transition data, for the PNNL/NIST biosignature gases, that are mapable to different temperatures and pressures. As shown in Section 4.7, there are many non-standard biosignature gases that may prove valuable in remote sensing observations. If spectral data for these gases becomes published, then they can be investigated for potential detectability in much greater detail. One key aspect for the success of this goal is linking the scientists who produce the spectral data with the scientists who complete the theoretical remote sensing studies. In this manner, we could streamline their molecular transition investigations to biosignature gases.

Another aspect that would benefit future work is the inclusion of additional molecular transitions for the HITRAN biosignature gases included in this study. Unfortunately, this goal is beyond the reach of many theoretical modelers as they are not

typically the ones producing their own transition data; however, increased collaboration, as indicated above, would help greatly in this regard. The creation of more comprehensive transition data (for all biosignature gases) will likely open up alternative targetings regions that were previously unknown for many molecules. Basically, the more flexability we have for each molecule, the more likely we are to detect that molecule even if other species mask some of its features.

A very important specific addition to future models in terms of additional spectral data for each molecule would be the inclusion of visible wavelength transition data. As the emission of a Sun-like star peaks in the visible region, the strength of the absorption from these visible transitions could prove to be a valuable means for detecting the molecules. Unfortunately, the only biosignature gas in the HITRAN database that has visible transition data is oxygen. Studies focused on producing visible data would be very valuable for remote sensing investigations as the theoretical modelers can only make predictions based on the quality and comprehensiveness of the transition data provided.

4.8.2 Atmospheric Evolution

Throughout the evolution of Earth, its atmosphere has evolved through different bulk compositions and thus has not always been oxygen-rich; therefore, it would not be surprising if observations detected Earth-like planets at different stages in this evolution.[3] While my study mainly considers the modern Earth atmosphere, future studies should investigate alternative periods in Earth's atmospheric evolution. In such cases (e.g., the early Earth atmosphere), other types of life-forms (e.g methanogens) may have created large abundances of alternative biosignature gases. My study has semi-probed this constuct with the models that included larger atmospheric abundances of the reduced gases, but has not changed other parameters, such as the stellar emission, that would be required to properly model early Earth conditions. With only the

[3]Note that the section of Earth's atmospheric evolution in terms of the rise of oxygen was a direct result of oxygen-producing life. Therefore, Earth-like planets in other systems are not necessarily anticipated to have the same exact evolution (in terms of the rise of oxygen) if they do not have life or another mechanism to prompt such an evolution.

knowledge of one Earth-like planet, we lack a full understanding of the processes that govern the composition of atmospheres on a statistical scale; therefore, any study investigating these potential options will prove valuable to the advancement of the field. One example of a study that began to probe the different epochs of Earth's atmospheric evolution is Kaltenegger et al. (2007).

4.8.3 Stellar Spectral Types and other Types of Planets

This study has considered an Earth-like planet around a Sun-like star; however, the parameter space for habitability is undoubtedly much larger. Combinations of different stellar types (e.g., K or M stars) and different sized planets (e.g., super-Earths) provide many opportunities for future research. As the exoplanet field is just beginning, not much previous research has been done in these areas, and thus, very interesting conclusions are likely to be the result of forthcoming research. For example, the anticipated larger atmospheres of super-Earth planets may allow for easier spectral detection due to the increased mass of the atmosphere. Alternatively, different stellar types (e.g., M stars) have their blackbody emission peak in the IR which may provide for easier detection of IR features in comparison to planets around stars whose blackbody emission peaks in the visible. As more exoplanets are discovered, an investigation of the exact interplay between the stellar spectral type and planetary size would be increasingly valuable to the field.

4.8.4 Atmospheric Temperature and Pressure Profiles

The exact atmospheric temperature and pressure profile for the modeled atmosphere may have an impact on the detectability of atmospheric gases. This aspect is specifically important as the temperature/pressure profile dictates the broadening of spectral lines. The exact effects of varying the atmospheric temperature/pressure profile on the detectability of biosignature gases are unknown. Studies investigating this region of parameter space may consider including: (1) an exaggerated Earth-like profile with the turning points between large-scale atmospheric layers (e.g., troposphere,

stratosphere, mesosphere, etc.) being pushed further warmer or colder than their current placement on Earth, (2) a temperature profile that is the reverse of Earth's profile (i.e. one that decreases where Earth's increases and vice versa), (3) an exaggeration of the temperature maxima and minima of case 2, (4) the inclusion of two or more stratospheres (i.e. temperature inversions), (5) atmospheres that are strictly isothermal, decreasing in temperature, or increasing in temperature with respect to altitude, (6) etc. While our current observational resolution is not good enough to disentangle different atmospheric layers on exoplanets, studies within this parameter space will lead to a better understanding of the impact that temperature and pressure has on the detectability of atmospheric gases. Though, it will be imperative for such studies to consult atmospheric dynamicists in order to ascertain that the alternative modeled temperature/pressure profiles are realistic.

4.8.5 Noise Budget

Observational noise was simulated in my study by modeling within 20% of the shot noise. By basing the noise budget solely off of shot noise, I was able to keep the results more general (i.e. not tie them to a particular telescope design) thus allowing for comparative investigations between general telescope sizes. Alternatively, real observations will always have some amount of systematic, or red, noise. This red noise will be dependent on the exact instrument chosen for the observations. Future studies could thus use the anticipated red noise from a given telescope (e.g., the *JWST* or a futuristic design) to predict a more representative noise level. The more accurately that the noise budget is modeled, the closer the models will relate to the future observations of particular telescopes. These models could then potentially determine the most beneficial studies to pursue with the new or future telescope.

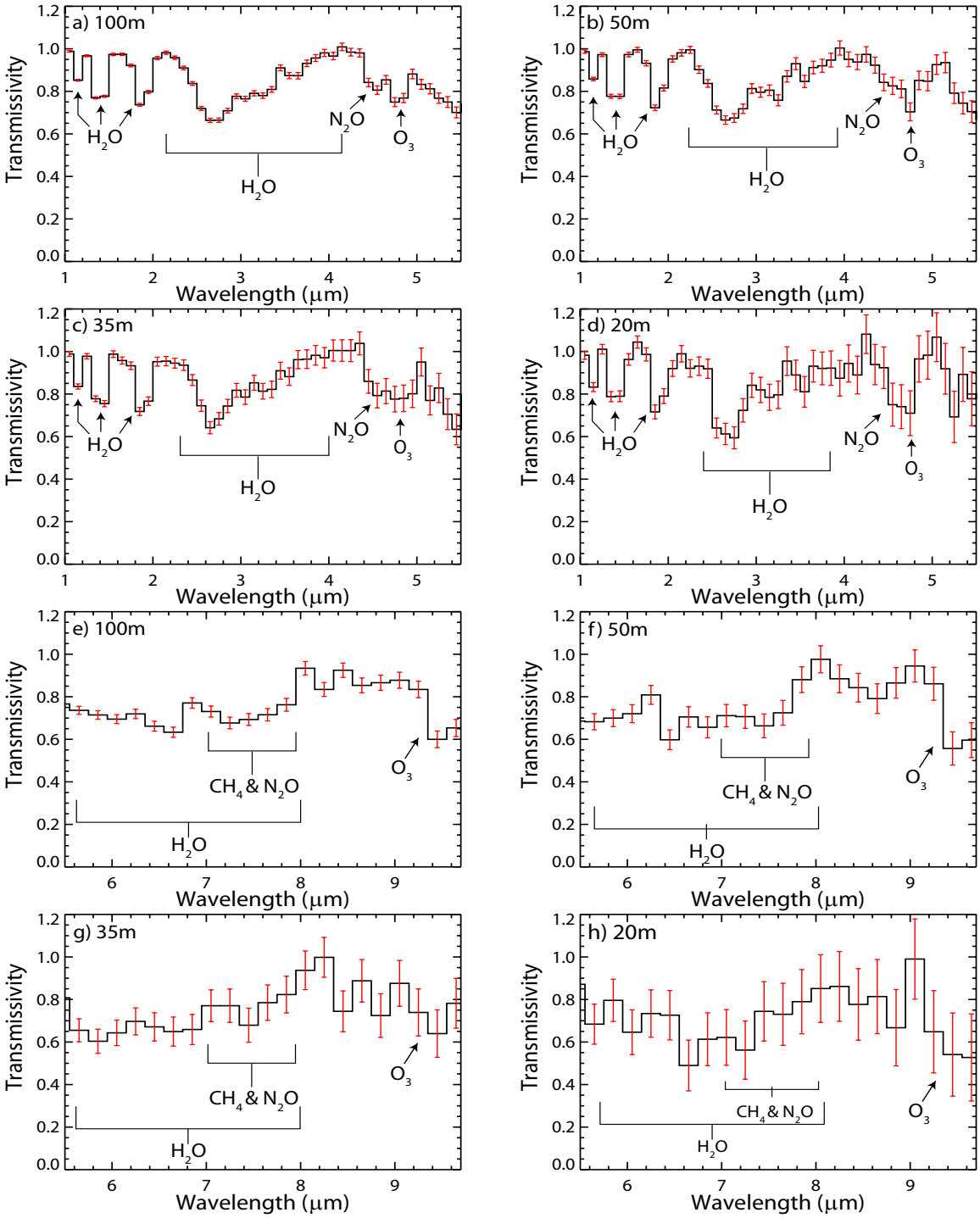

Figure 4-1: Transmissivity profiles (modeled within 20% of the shot noise) for varying telescope sizes for an Earth-like planet (orbiting a Sun-like star) located at 35.45 parsecs and observed for 100 hours. These transmissivity spectra are representative of an 86 km annulus surrounding a planet with a radius equal to Earth's radius. The abundances of the gases used in this model are provided in Table 4.2. The first four subfigures show the absorption between 1 and 5.5 μm while the last four subfigures show the features that occur between 5.5 and 9.5 μm. The bin size for plots a-d is 0.1 μm, and the bin size for plots e-h is 0.2 μm. As seen, only a few of the biosignature gases (namely, nitrous oxide, ozone, and methane) have large enough abundances for their features to be discernible from the water continuum.

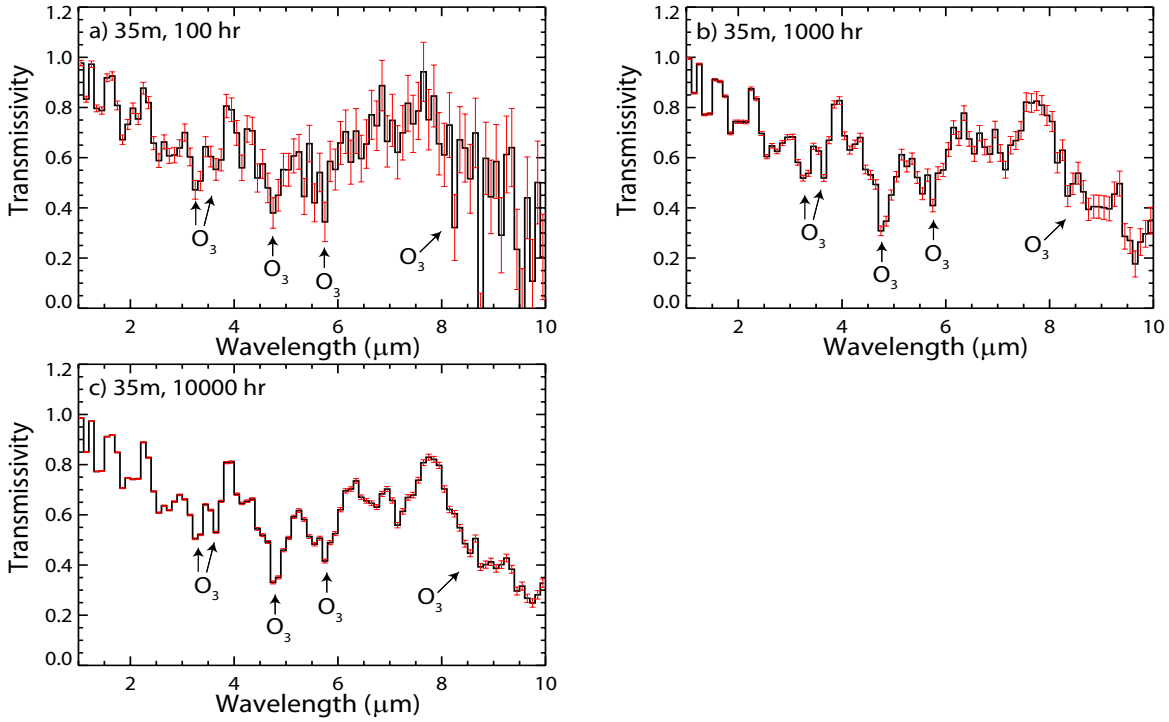

Figure 4-2: These transmissivity spectra (modeled within 20% of the shot noise) are representative of an 86 km annulus surrounding a planet with a radius equal to Earth's radius. They demonstrate the effect on the noise budget from increasing observation time for a 35 m telescope for an atmosphere consisting of 20% ozone and 1% water. The 35 m telescope size is chosen for this illustration because previous studies (e.g., Ehrenreich et al. 2006) have suggested that a $30 - 40$ meter telescope would be required to detect Earth-like planets. The bin size is 0.1 μm.

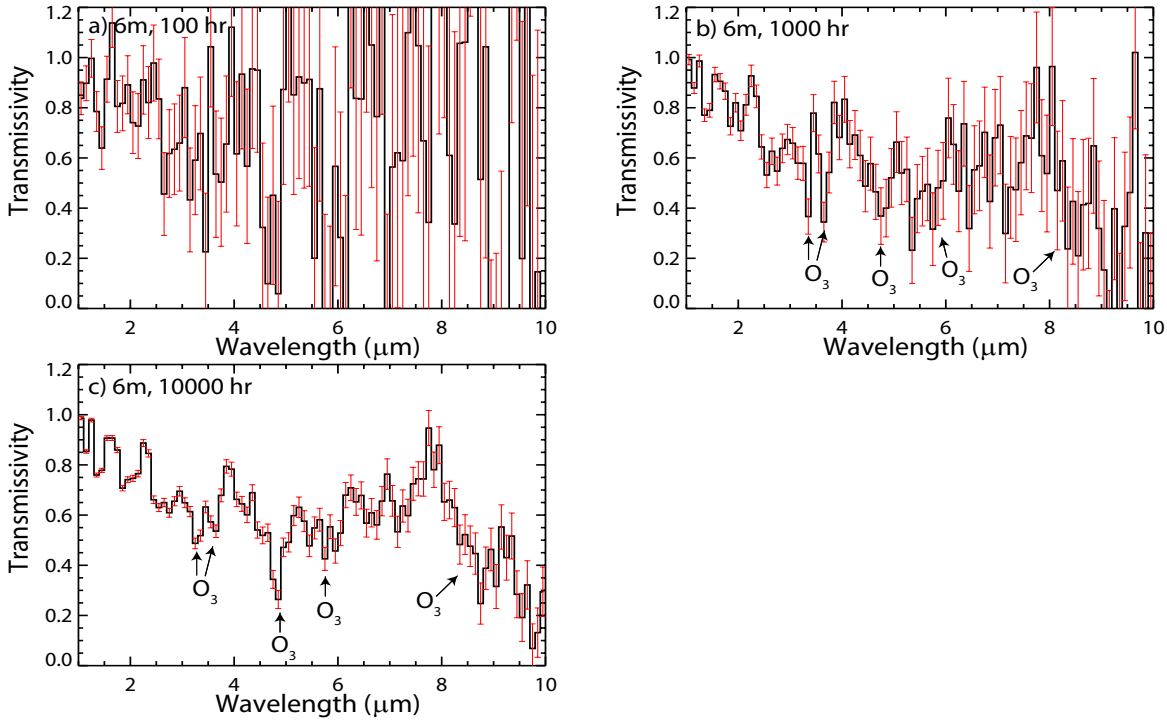

Figure 4-3: These transmissivity spectra (modeled within 20% of the shot noise) are representative of an 86 km annulus surrounding a planet with a radius equal to Earth's radius. They demonstrate the effect on the noise budget from increasing observation time for a 6 m telescope for an atmosphere consisting of 20% ozone and 1% water. The 6 m telescope is chosen to demonstrate the technological ability of a telescope of the same class as the *JWST*. The bin size is 0.1 μm.

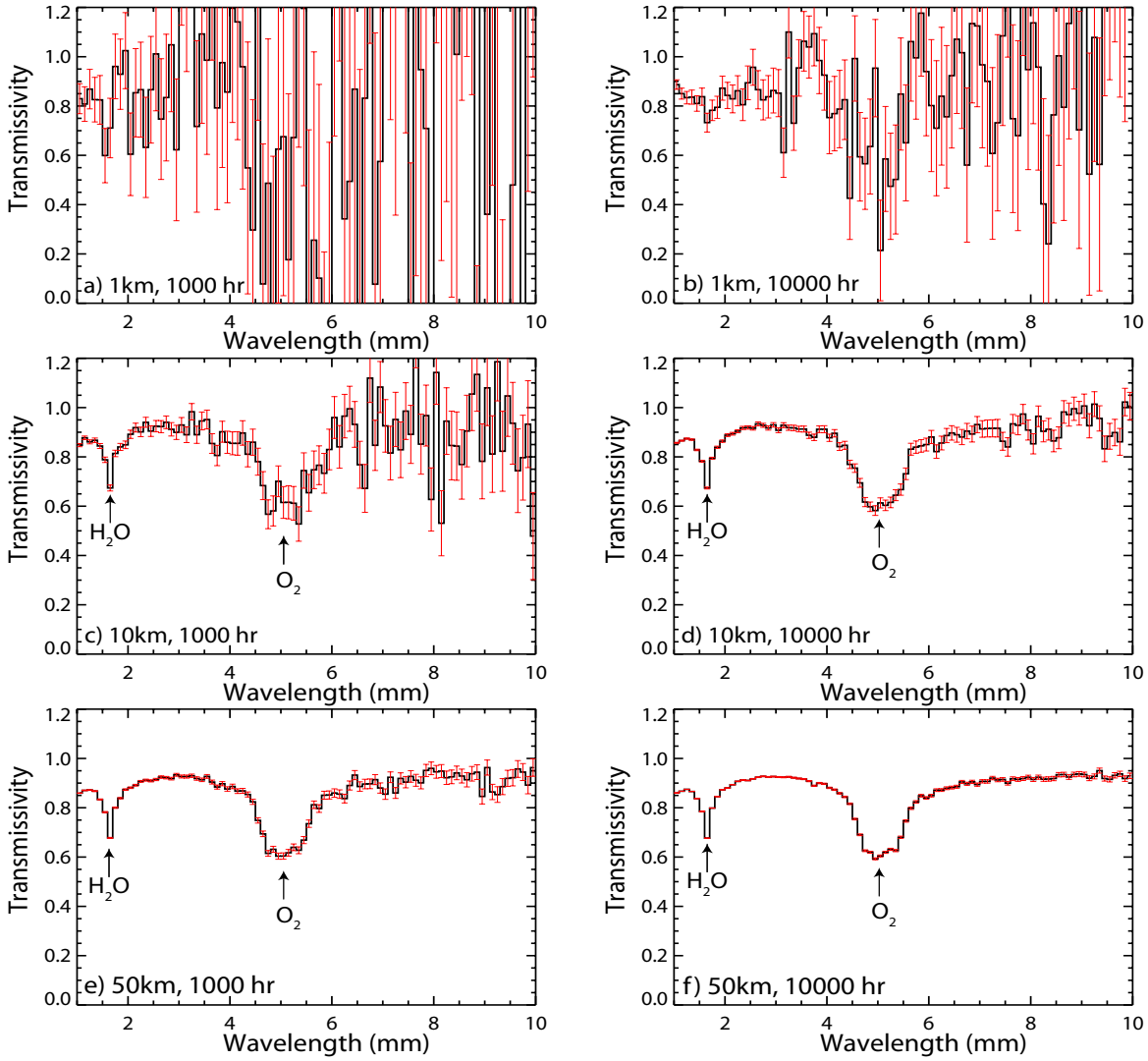

Figure 4-4: These figures depict transmissivity spectra (modeled within 20% of the shot noise) for an atmosphere consisting of 20% oxygen and 1% water for combinations of three telescope sizes (1 km, 10 km, and 50 km) and two observation times (1000 and 10,000 hours). These figures demonstrates the requirements for observing in the millimeter region of the spectrum. These transmissivity spectra are representative of an 86 km annulus surrounding a planet with a radius equal to Earth's radius. The bin size is 0.1 mm.

Chapter 5

Summary & Conclusion

5.1 Summary

I now enumerate the main findings of my study and briefly discuss them afterwards.

1. Globally averaged mixing ratios in the tens to hundreds of ppm will be necessary for the detection of most biosignature gases on Earth-sized planets orbiting Sun-like stars.

2. As many biosignature gases have absorption bands between $7 - 10$ μm, it will be difficult to disentangle the individual spectral profiles between $7 - 10$ μm; therefore, detections of multiple spectral features for each molecule will provide the best way to determine the contribution of each species to the overall transmissivity spectrum.

3. While a 20 m space telescope could detect some biosignature gases with larger atmospheric mixing ratios (e.g., 1000 ppm), a 35 m space telescope will provide a much better opportunity to probe mixing ratios in the range of tens to hundreds of ppm. If a space telescope of the 35 m class is not realistic for production within 100 years, then we must determine alternate methods to achieve the same level of detectability (e.g., the potential use of interferometry with smaller telescopes).

4. For Earth-size planets around Sun-like stars, the most promising IR region for detection of biosignature gases is $1 - 5$ μm.

5. For proper detection and estimation of biosignature gas mixing ratios in the atmospheres of exoplanets, significant confidence on the mixing ratio of water is required.

6. The spectral resolution chosen for transmissivity observations will need to optimize the parameter space between two extremes: (1) too high of a resolution such that any signal effectively disappears due to shot noise and (2) too low of a resolution such that different features are smeared together and, thus, indiscernible from one another.

5.1.1 Atmospheric Threshold Mixing Ratio Required for the Detection of an Atmospheric Species

The battle for detectability of many of the biosignature gases relies heavily on the atmospheric mixing ratio of the gas. Atmospheric gases with mixing ratios smaller than the ppm range will likely never be detectable with significant confidence ($> 5\sigma$) on Earth-sized planets (transiting Sun-like stars) observed for 100 hours with a 35 m telescope and the source located 35.45 parsecs from Earth. Though many biosignature gases on Earth have abundances lower than the ppm range (e.g., see Table 4.2), there is no reasoning to suspect that such gases cannot achieve higher mixing ratios on other planets; therefore, the ppm mixing ratio requirement described here does not exclude the potential detectability of any of the gases investigated in my study. In the end, an increase to the telescope size and/or the observation duration would help in the detection of trace gases in exoplanet atmospheres.

5.1.2 The Difficulty of Biosignature Gas Detection due to the Blending of Spectral Features

The ability of many biosignature gases to absorb between $7 - 10$ μm will cause much difficulty for molecular identification in this wavelength region. Therefore, it will be imperative to observe other molecular features/bands to determine what atmospheric gases are contributing to absorption within the $7 - 10$ μm region. In addition, if multiple molecular features for each molecule are investigated, then theoretical models will be able to use the relative absorption between the features to provide constraints on the mixing ratio of each atmospheric gas. These constraints will be able to be used to determine each species' contribution to absorption between $7 - 10$ μm.

5.1.3 Photon Collecting Area Requirement for Large-Scale Detection of Atmospheric Gases on Exoplanets

As many biosignature gases appear in low concentrations on Earth (e.g., see Table 4.2), it is imperative to be able to probe the lowest mixing ratios possible. Increasing the telescope size is prudent to increasing the level of detectability of lower atmospheric mixing ratios. Though a 20 m class telescope may detect gases with larger atmospheric mixing ratios and may be a necessary technological step after the *JWST*, a 35 m class telescope should be the minimum size considered for investigations concerning Earth-like planets orbiting Sun-like stars. If 35 m class telescopes are not technologically or economically feasible within the next 100 years, then we must determine if alternate methods can produce the same level of detectivity. For example, smaller telescopes aligned side-by-side could produce the same collecting area as one larger telescope, though future research is required to determine if the telescopes could be used in this manner. As mass production of any product typically reduces the price per unit, the array of smaller telescopes may cost much less than the production of a single, larger telescope with an equal collecting area. If the economic cost is reasonable and the technological difficulty is not too great, then the telescope array

alternative may prove to be the future direction for exoplanet atmospheric detection.

5.1.4 The IR Region with the Largest Signal

Due to the stellar blackbody spectral profile of a Sun-like star decreasing in intensity at longer wavelengths (i.e. less signal at longer wavelengths), the best section of the IR region to probe the atmospheres of Earth-sized planets transiting Sun-like stars is $1 - 5$ μm. Beyond 5 μm, one encounters difficulties due to a water band effective at masking other spectral features and the potential overlap of spectral bands between $7 - 10$ μm for many biosignature gases.

5.1.5 The Importance of Tight Constraints on Atmospheric Water Vapor Concentration

The potential spectral masking of biosignature gas features by water vapor bands complicates the detection of biosignature gases. Without tight constraints on the atmospheric water vapor concentration, it will be unknown if the absorption in overlapping spectral regions (of water vapor and biosignature gases) is due to an increased presence of water or from a larger concentration of the biosignature gas(es) in question. Since water has many absorption features, determining its existence and concentration is not anticipated to be significantly difficult, though high accuracy will be required. Once the water absorption is properly accounted for in transmissivity spectra, then we can properly estimate the concentration of biosignature gases in the transmissivity spectra.

5.1.6 The Necessity of Optimizing the Spectral Resolution

An optimization of the spectral resolution will provide for the best opportunity to disentangle overlapping spectral features. If the optimized spectral resolution does not de-blend certain features, then the shot noise should be further decreased such that a higher resolution can be attained. Two ways to decrease shot noise are increasing the size of the telescope and/or increasing the observation duration. If the telescope

is already constructed, then increasing observation time would be the most logical solution; however, for telescopes in the design phase, it is imperative to design the telescope with a spectral resolution that can resolve the desired features in question.

5.2 Conclusion

The field of exoplanet research has exploded since the first exoplanet discovery two decades ago. While the first round of detections included many non-Earth-like planets (e.g., hot Jupiters), the advance of technology is pushing rapidly towards the detection of an Earth-like planet. The successful detection of such a planet will undoubtedly revolutionize the field as well as humanity's understanding of the cosmos. The resulting era will forever be remembered as the point at which it all started, and with time, future observations will hopefully answer the question of whether we are alone in the universe.

For current observational exoplanet research, one large goal is to detect Earth-size planets. My study has illustrated what scientists should focus on after they have detected the first Earth-sized exoplanet: the atmosphere of the exoplanet, which will contain a plethora of information about the planet. These atmospheric studies will be what determines if the exoplanet is Earth-like or, simply, Earth-sized. With advancing technology, we should be able to deduce the constituents of the atmosphere and determine if the planet would be suitable to host Earth-like life.

The potential detection of particular biosignature gases − that would be beneficial in determining if an exoplanet is Earth-like and the exoplanet's potential for habitability − has been investigated in this study. For a true Earth-analog, I have determined that the only biosignature gases that are discernible from the continuum in transmissivity spectroscopy (for a planet located at a distance of 35.45 parsecs from Earth) are ozone, nitrous oxide, and methane. Though it will be difficult to disentangle their absorpton profiles in the IR, their combined absorption would be distinguishable from a 1% atmospheric water profile. Increased spectral resolution could disentangle these features, but the overall atmospheric abundance also plays

a key role in their discernability. Increases to the atmospheric abundances of more trace-like biosignature gases (CH_3Br, CH_3Cl, H_2S, etc.) would allow their features to become more discernible from the continuum in comparison to that of a true Earth-analog. The atmospheric abundances required for each HITRAN and PNNL/NIST biosignature gas to be detectable have been analyzed in Chapter 3 and Section 4.7, respectively. While a true Earth-analog may be difficult to detect, other systems (e.g., different stellar types and/or larger planets) may provide better environments for biosignature detections. These and other areas of future research research have been discussed in Chapter 4.

One of my overall goals for this study was to describe how to properly model transmissivity radiative transfer (see Chapter 2). The in-depth descriptions of remote sensing theory were purposely included due to them not appearing in many standard texts that I have encountered during my studies. Through these detailed descriptions, I hope to have provided an easier platform for others to learn. I conclude by thanking all of those who have read this work and hope that you have benefited from this manuscript.

Appendix A

Three Types of Modeled Spectra

One major goal for this work is to provide to other researchers a blue print and better learning platform for calculating transmissivity spectra through explaining both the derivations and hidden intricacies in much detail. In the main text of this work, I focused on modeling the transmissivity spectrum as opposed to discussing the transmission spectrum. In this appendix, I will derive the transmission spectrum and its connection to both the transmissivity spectrum and the effective height of absorption spectrum. I will also calculate the error on the transmission spectrum and demonstrate how to propagate that error to errors for the transmissivity spectrum and the effective height of absorption spectrum. I conclude Appendix A by demonstrating that the transmission spectrum and the effective height of absorption spectrum does not depend on the modeled atmospheric height, while also describing why the transmissivity spectrum does depend on the modeled atmospheric height. Much thanks and appreciation goes to my good friend and colleague Julien de Wit, as these detailed derivations are a result of our intensive collaboration.

A.1 Derivation of Three Types of Modeled Spectra

A.1.1 The Transmission Spectrum

In this first section, I will derive the transmission spectrum. The transmission spectrum is defined as the flux drop that occurs when a planet transits its host star. For this derivation, I assume the geometry given in Figure A-1. For Appendix A, R_{planet}

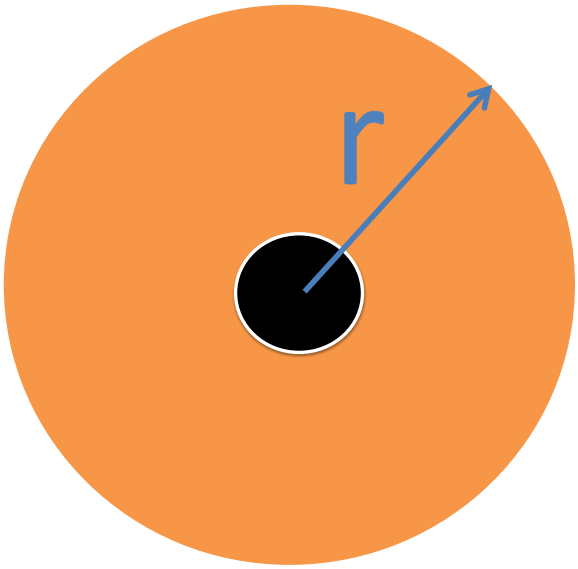

Figure A-1: Pictorial of an exoplanet transiting its host star. The solid surface of the planet is shown in black. The atmosphere of the planet is shown in white. The star is shown in orange. I do not consider any stellar limb darkening effects in these derivations.

equals the radius of the planet including the atmospheric component, $R_{surface}$ equals the distance from the planet center to the planet surface (no atmospheric component), and R_* equals the radius of the star.

As previously mentioned, the transmission spectrum is defined as the flux drop that occurs during a transit. The ratio of the flux drop is equivalent to the ratio of the intensity drop as well as the ratio of the drop of the number of photons observed.

In equation from, this equality becomes

$$\begin{aligned} Transmission(\lambda) &= -\frac{\Delta F}{F_{out}}(\lambda) = -\frac{\Delta I}{I_{out}}(\lambda) = -\frac{\Delta N}{N_{out}}(\lambda) \\ \Rightarrow Transmission(\lambda) &= \frac{F_{out}-F_{in}}{F_{out}}(\lambda) = \frac{I_{out}-I_{in}}{I_{out}}(\lambda) = \frac{N_{out}-N_{in}}{N_{out}}(\lambda), \end{aligned} \tag{A.1}$$

where F designates flux, I designates intensity, N designates the number of photons, the subscript "*out*" designates the total of the corresponding quantity out-of-transit, and the subscript "*in*" designates the total of the corresponding quantity in-transit. To derive the equation for the transmission spectrum, I will use the intensity drop version from above. In order to get I_{out} and I_{in}, I must integrate Eq. (2.10) over the geometry of Fig. A-1. Through integration,

$$Transmission(\lambda) = \frac{I_{out} - I_{in}}{I_{out}} = \frac{\int_0^\infty I_o 2\pi r dr - \int_0^\infty I_i 2\pi r dr}{\int_o^\infty I_o 2\pi r dr}, \tag{A.2}$$

where I_o and I_i are the intensities out-of-transit and in-transit, respectively, from one beam of radiation. The integration in Eq. A.2 basically sums up the contribution from every beam of radiation in order to calculate I_{out} and I_{in}. Note that, for out-of-transit calculations, I assume that the planet does not contribute to the observed intensity; thus I_o is the spatial average of the star's brightness. Also, if $r > R_*$, then $I_o = I_i = 0$; therefore,

$$Transmission(\lambda) = \frac{\int_0^{R_*} I_o 2\pi r dr - \int_0^{R_*} I_i 2\pi r dr}{\int_o^{R_*} I_o 2\pi r dr}. \tag{A.3}$$

Since I_o is independent of r, I can pull the I_o out of the corresponding integrals and then calculate the I_o integrals:

$$\begin{aligned} Transmission(\lambda) &= \frac{I_o \int_0^{R_*} 2\pi r dr - \int_0^{R_*} I_i 2\pi r dr}{I_o \int_o^{R_*} 2\pi r dr} = \frac{I_o \cdot \pi R_*^2 - \int_0^{R_*} I_i 2\pi r dr}{I_o \cdot \pi R_*^2} \\ &= \frac{\pi R_*^2 - \int_0^{R_*} \frac{I_i}{I_o} 2\pi r dr}{\pi R_*^2}. \end{aligned} \tag{A.4}$$

By referencing Eq. 2.10, we can see that $I_i = I_o e^{-\tau(r,\lambda)} \Rightarrow \frac{I_i}{I_o} = e^{-\tau(r,\lambda)}$; therefore,

$$Transmission(\lambda) = 1 - \frac{1}{\pi R_*^2} \int_0^{R_*} e^{-\tau(r,\lambda)} 2\pi r dr. \tag{A.5}$$

Due to radial dependency of the optical depth $\tau(r, \lambda)$, we need to split up the integral of Eq. (A.5) into three radial regions: $0 < r < R_{surface}$; $R_{surface} < r < R_{planet}$; and $R_{planet} < r < R_*$. Adopting this convention, Eq. (A.5) becomes

$$\begin{aligned} Transmission(\lambda) = 1 - \tfrac{1}{\pi R_*^2} [\textstyle\int_0^{R_{surface}} e^{-\tau(r,\lambda)} 2\pi r dr \\ + \int_{R_{surface}}^{R_{planet}} e^{-\tau(r,\lambda)} 2\pi r dr + \int_{R_{planet}}^{R_*} e^{-\tau(r,\lambda)} 2\pi r dr] \end{aligned} \tag{A.6}$$

The value of $\tau(r, \lambda)$ depends on the radial distance from the center of the planet, namely:

1. If $0 < r < R_{surface} \Rightarrow \tau = \infty$

2. If $R_{surface} < r < R_{planet} \Rightarrow \tau = \tau(r, \lambda)$

3. If $R_{planet} < R_* \Rightarrow \tau = 0$

I now plug in these values for $\tau(r, \lambda)$ into Eq. A.6 and calculate the end transmission spectrum equation.

$$\begin{aligned} Transmission(\lambda) = 1 - \tfrac{1}{\pi R_*^2} [\textstyle\int_0^{R_{surface}} e^{-\infty} 2\pi r dr + \int_{R_{surface}}^{R_{planet}} e^{-\tau(r,\lambda)} 2\pi r dr + \\ \int_{R_{planet}}^{R_*} e^{0} 2\pi r dr] \end{aligned}$$

$$Transmission(\lambda) = 1 - \frac{1}{\pi R_*^2} \left[0 + \int_{R_{surface}}^{R_{planet}} e^{-\tau(r,\lambda)} 2\pi r dr + \int_{R_{planet}}^{R_*} 2\pi r dr \right]$$

$$Transmission(\lambda) = 1 - \frac{1}{\pi R_*^2} \left[\int_{R_{surface}}^{R_{planet}} e^{-\tau(r,\lambda)} 2\pi r dr + \pi (R_*^2 - R_{planet}^2) \right]$$

$$Transmission(\lambda) = 1 - \frac{\pi R_*^2}{\pi R_*^2} + \frac{\pi R_{planet}^2}{\pi R_*^2} - \frac{1}{\pi R_*^2}\left[\int_{R_{surface}}^{R_{planet}} e^{-\tau(r,\lambda)} 2\pi r dr\right]$$

$$Transmission(\lambda) = \frac{R_{planet}^2}{R_*^2} - \frac{1}{\pi R_*^2}\left[\int_{R_{surface}}^{R_{planet}} e^{-\tau(r,\lambda)} 2\pi r dr\right] \tag{A.7}$$

At first glance, the derivation between Eqs. (A.5) and (A.7) appears to be specific to the geometry of Fig. A-1. However, as long as the cross section of the planet (as seen in transmission) is fully contained within the cross section of the host star, the derivation between Eq. (A.5) and Eq. (A.7) is valid because the flux drop from the transiting planet is the same regardless of the planet's location in the transit path.

A.1.2 The Transmissivity Spectrum

The transmissivity spectrum refers to the amount of light that is not absorbed by the modeled atmosphere. I will now use the transmission spectrum to calculate the transmissivity spectrum. The transmissivity spectrum equation below [Eq. (A.8)] was first presented as Eq. (2.11) in Chapter 2:

$$Transmissivity(\lambda) = \frac{1}{\pi(R_p^2 - R_s^2)} \int_{R_{surface}}^{R_{planet}} e^{-\tau(r,\lambda)} 2\pi r dr. \tag{A.8}$$

It is noticable that the integrals of Eqs. (A.7) and (A.8) are both describing the effective area of the atmosphere that lets light through. Since the two integrals are equivalent, I can solve Eq. (A.7) for its integral and then plug that expression into Eq. (A.8). Solving Eq. (A.7) for the integral gives

$$\int_{R_{surface}}^{R_{planet}} e^{-\tau(r,\lambda)} 2\pi r dr = \pi R_*^2 \left[\frac{R_{planet}^2}{R_*^2} - Transmission(\lambda)\right]. \tag{A.9}$$

Plugging the expression from Eq. (A.9) into Eq. (A.8), I receive

$$Transmissivity(\lambda) = \frac{R_*^2}{R_{planet}^2 - R_{surface}^2} * \left[\frac{R_{planet}^2}{R_*^2} - Transmission(\lambda)\right]. \tag{A.10}$$

Note two different extremes:

1. If the $Transmission(\lambda) = \frac{R^2_{planet}}{R^2_*} \rightarrow Transmissivity(\lambda) = 0$
2. If the $Transmission(\lambda) = \frac{R^2_{surface}}{R^2_*} \rightarrow Transmissivity(\lambda) = 1$

A.1.3 The Effective Height of Absorption Spectrum

In real observations, the radius of the planet is wavelength dependent due to absorption from the atmosphere. Basically, some wavelengths are opaque to a higher level in the atmosphere while others may be transparent all the way down to the surface of the planet. The effective height of absorption spectrum calculates the effective radius of the planet at each wavelength due to atmospheric absorption. I will now derive the effective height of absorption spectrum. The fraction of the host star's area that is blocked by the absorbing atmosphere is $f_p(\lambda)$ where

$$f_p(\lambda) = Transmission(\lambda) - \frac{R^2_{surface}}{R^2_*}. \tag{A.11}$$

The transmission spectrum in Eq. (A.11) represents the flux drop resulting from both the planet and its atmosphere. This flux drop is equivalent to R^2_{planet}/R^2_* which equals $[R_{surface}+h_{eff}(\lambda)]^2/R^2_*$, where $h_{eff}(\lambda)$ is the effective height of the atmosphere. Substituting in for the transmission spectrum in Eq. (A.11), we receive

$$f_p(\lambda) = \frac{[R_{surface} + h_{eff}(\lambda)]^2}{R^2_*} - \frac{R^2_{surface}}{R^2_*}, \tag{A.12}$$

which can be simplified to

$$f_p(\lambda) = \frac{2R_{surface}h_{eff}(\lambda) + h_{eff}(\lambda)^2}{R^2_*}. \tag{A.13}$$

For terrestrial planets, it is suitable to assume that $h_{eff}(\lambda) << R_{surface}$ and thus the $h_{eff}(\lambda)^2$ component can be dropped from Eq. (A.13) leading to

$$f_p(\lambda) = \frac{2R_{surface}h_{eff}(\lambda)}{R^2_*}. \tag{A.14}$$

Setting Eqs. (A.14) and (A.11) equal and solving for the effective atmospheric height, we receive

$$h_{eff}(\lambda) = \frac{Transmission(\lambda) - \frac{R_{surface}^2}{R_*^2}}{2\frac{R_{surface}}{R_*^2}}. \tag{A.15}$$

A.2 Synthetic Noise for the Three Spectra

A.2.1 Modeled Error for the Transmission Spectrum

To simulate a realization of a "noisy" transmission spectrum with a noise component that is within a certain percentage "X" of the photon noise, use the following equations:

$$Transmission_{noisy} = Transmission_{clean} \pm \sigma_{transmission}, \tag{A.16}$$

where

$$\sigma_{transmission} = (1 + X) \cdot \frac{\alpha}{SNR}. \tag{A.17}$$

X represents how closely one models the noise level to the photon (i.e. for $X = 0.2$, one is modeling within 20% of the photon noise), α is a Gaussian distribution with a standard deviation equal to 1, the SNR is the signal-to-noise ratio on the photon flux, and $Transmission_{clean}$ is the transmission spectrum calculated from Eq. (A.7). As X is chosen by the researcher, the only unknown quantity is the SNR of the photon flux. The SNR is calculated through

$$SNR = \frac{Signal}{Noise} = \frac{n_\lambda}{\sqrt{n_\lambda}} = \sqrt{n_\lambda}, \tag{A.18}$$

where n_λ equals the number of photons received at the detector (wavelength dependent) and is calculated by

$$n_\lambda = \frac{\lambda \cdot E_{total}(\lambda)}{hc}, \tag{A.19}$$

where $E_{total}(\lambda)$ equals the total energy (wavelength dependent) received at the detector [see Eq. (A.20) below], λ equals the wavelength of light being investigated,

h equals Planck's constant, and c equals the speed of light. $E_{total}(\lambda)$ is calculated through

$$E_{total}(\lambda) = B_\lambda(T) \cdot w_\lambda \cdot \pi R_*^2 \cdot \Delta t \cdot \frac{\pi r_{detector}^2}{d^2}, \tag{A.20}$$

where $B_\lambda(T)$ is Planck's law, w_λ is the width of each wavelength bin over which the detector observes, πR_*^2 is the surface area of the star responsible for the emitted radiation, Δt accounts for the time of the observation, and $\frac{\pi r_{detector}^2}{d^2}$ is the solid angle of the observation where $r_{detector}$ is the radius of the detector and d is the distance to the target. Given all of the pieces outlined above, I can now calculate $\sigma_{transmission}$.

A.2.2 Modeled Error for the Transmissivity Spectrum

In this section, I will use the error on the transmission spectrum and the relation between the transmission spectrum and the transmissivity spectrum to calculate the error on the transmissivity spectrum. The equation for the transmissivity spectrum is given above in Eq. (A.10) and repeated here:

$$Transmissivity(\lambda) = \frac{R_*^2}{R_{planet}^2 - R_{surface}^2}\left[\frac{R_{planet}^2}{R_*^2} - Transmission(\lambda)\right]. \tag{A.21}$$

Distributing the multiplicative factor of Eq. A.21, I receive

$$Transmissivity(\lambda) = \frac{R_{planet}^2}{R_{planet}^2 - R_{surface}^2} - \frac{R_*^2}{R_{planet}^2 - R_{surface}^2} \cdot Transmission(\lambda). \tag{A.22}$$

I now propagate the error from the transmission spectrum. There is no error on $\frac{R_{planet}^2}{R_{planet}^2 - R_{surface}^2}$ because R_{planet} and $R_{surface}$ are references and not physical parameters that affect the signal. Therefore, I only need the error resulting from the $\frac{R_*^2}{R_{planet}^2 - R_{surface}^2} \cdot Transmission(\lambda)$. Through error propagation:

$$\sigma_{transmissivity} = \frac{R_*^2}{R_{planet}^2 - R_{surface}^2} \cdot \sigma_{transmission}. \tag{A.23}$$

I will now take the opportunity to illuminate an additional subtlety of my model by substituting in for R_{planet} in Eq. (A.23). Using $R_{planet} = R_{surface} + H$, where H is the

atmospheric height, we receive

$$\sigma_{transmissivity} = \frac{R_*^2}{(R_{surface} + H)^2 - R_{surface}^2} \cdot \sigma_{transmission}, \tag{A.24}$$

which leads to

$$\sigma_{transmissivity} = \frac{R_*^2}{2HR_{surface} + H^2} \cdot \sigma_{transmission}. \tag{A.25}$$

For terrestrial planets $H << R_{surface}$; therefore, the H^2 in Eq. (A.24) can be dropped leading to

$$\sigma_{transmissivity} = \frac{R_*^2}{2HR_{surface}} \cdot \sigma_{transmission}. \tag{A.26}$$

Eq. (A.26) is equivalent to the transmissivity noise I modeled with Eq. (2.22). The main point to emphasize is that Eq. (2.22) is particularly suited for terrestrial planets where $H << R_{surface}$. For studies involving planets with extended atmospheres, one must use Eq. A.25 to calculate the noise on the transmissivity spectrum.

A.2.3 Modeled Error for the Effective Height of Absorption Spectrum

In this section, I will use the error on the transmission spectrum and the relation between the transmission spectrum and the effective height of absorption spectrum to calculate the error on the effective height of absorption spectrum. The equation for the effective height of absorption spectrum is given in Eq. (A.15) and repeated here:

$$h_{eff}(\lambda) = \frac{Transmission(\lambda) - \frac{R_{surface}^2}{R_*^2}}{2\frac{R_{surface}}{R_*^2}}. \tag{A.27}$$

A simplification of Eq. (A.27) yields

$$h_{eff}(\lambda) = \frac{R_*^2}{2R_{surface}} \cdot Transmission(\lambda) - \frac{R_{surface}}{2}. \tag{A.28}$$

There is no error on $\frac{R_{surface}}{2}$; therefore, the only error is on $\frac{R_*^2}{2R_{surface}} \cdot Transmission(\lambda)$. Therefore, through error propagation:

$$\sigma_{h_{eff}} = \frac{R_*^2}{2R_{surface}} \cdot \sigma_{transmission}. \tag{A.29}$$

A.3 Dependencies on Atmospheric Height

From the derived transmission spectrum above [Eq. (A.7)], it appears that the transmission spectrum depends on the atmospheric height H chosen for the model (due to the parameter R_{planet} appearing in the transmission equation, where $R_{planet} = R_{surface} + H$). However, physical observables (e.g. the transmission spectrum) are not dependent on the atmospheric reference used in the model. In this case, the transmission spectrum is not dependent on the atmospheric height used in the model in opposition to the transmissivity spectrum (not an observable) which is dependent on the reference atmospheric height. I demonstrate these relations below beginning with the transmission spectrum. For reference, I repeat the transmission spectrum [Eq. A.7] here:

$$Transmission(\lambda) = \frac{R_{planet}^2}{R_*^2} - \frac{1}{\pi R_*^2}\left[\int_{R_{surface}}^{R_{planet}} e^{-\tau(r,\lambda)} 2\pi r dr\right]. \tag{A.30}$$

I define a radius $R_{\tau=0}$ of the planet above which $\tau = 0$ for all wavelengths. I will now split the integral in Eq. (A.30) into two regions ($R_{surface} \rightarrow R_{\tau=0}$ and $R_{\tau=0} \rightarrow R_{planet}$) to show that the transmission spectrum does not depend on the modeled atmospheric height. The calculation follows below.

$$Transmission(\lambda) = \frac{R_{planet}^2}{R_*^2} - \frac{1}{\pi R_*^2}\left[\int_{R_{surface}}^{R_{\tau=0}} e^{-\tau(r,\lambda)} 2\pi r dr + \int_{R_{\tau=0}}^{R_{planet}} e^{-\tau(r,\lambda)} 2\pi r dr\right]$$

$$Transmission(\lambda) = \frac{R_{planet}^2}{R_*^2} - \frac{1}{\pi R_*^2}\left[\int_{R_{surface}}^{R_{\tau=0}} e^{-\tau(r,\lambda)} 2\pi r dr + \int_{R_{\tau=0}}^{R_{planet}} e^{0} 2\pi r dr\right]$$

$$Transmission(\lambda) = \frac{R_{planet}^2}{R_*^2} - \frac{1}{\pi R_*^2}\left[\int_{R_{surface}}^{R_{\tau=0}} e^{-\tau(r,\lambda)} 2\pi r dr + \pi(R_{planet}^2 - R_{\tau=0}^2)\right]$$

$$Transmission(\lambda) = \frac{R_{planet}^2}{R_*^2} - \frac{\pi(R_{planet}^2 - R_{\tau=0}^2)}{\pi R_*^2} - \frac{1}{\pi R_*^2}\left[\int_{R_{surface}}^{R_{\tau=0}} e^{-\tau(r,\lambda)} 2\pi r dr\right]$$

$$Transmission(\lambda) = \frac{R_{planet}^2}{R_*^2} - \frac{R_{planet}^2}{R_*^2} + \frac{R_{\tau=0}^2}{R_*^2} - \frac{1}{\pi R_*^2}\left[\int_{R_{surface}}^{R_{\tau=0}} e^{-\tau(r,\lambda)} 2\pi r dr\right]$$

$$Transmission(\lambda) = \frac{R_{\tau=0}^2}{R_*^2} - \frac{1}{\pi R_*^2}\left[\int_{R_{surface}}^{R_{\tau=0}} e^{-\tau(r,\lambda)} 2\pi r dr\right] \tag{A.31}$$

As seen in the second to last line of the derivation above, the original $\frac{R_{planet}^2}{R_*^2}$ cancels out with a $-\frac{R_{planet}^2}{R_*^2}$ resulting from the integral. Additionally, the last line of the derivation above [Eq. (A.31)] has no dependence on the atmospheric height chosen for the model; therefore, the derivation proves that the transmission spectrum does not depend on atmospheric height. Furthermore, if one compares Eq. (A.31) with Eq. (A.15), one can notice that the effective height of absorption spectrum also does not depend on atmospheric height.

Contrary to the transmission spectrum and the effective height of absorption spectrum, the transmissivity spectrum *does* depend on the atmospheric height chosen for the model because the transmissivity spectrum represents the amount of light that passes through a modeled annulus (of a chosen size) surrounding the planet. The effect of atmospheric absorption on the transmissivity spectrum depends on the relationship between the size of the annulus modeled, the size of the atmosphere, and the absorption strength of the atmosphere. Three case examples are shown in Figure A-2.

If the annulus chosen models a small portion of the atmosphere as shown in Fig. A-2a, then the relative amount of stellar light that makes it through the annulus is very small and thus deep spectral features will result in the transmissivity spectrum. If the atmosphere is opaque within the annulus of Fig. A-2a, then the transmissivity spectrum will be saturated (i.e. $transmissivity(\lambda) = 0$) and no information can be gained. For Fig. A-2b, it is assumed that the annulus is chosen such that the

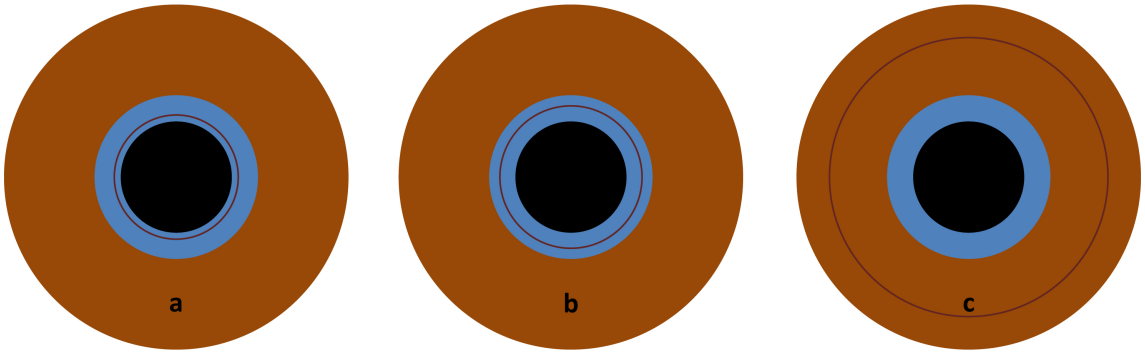

Figure A-2: The black represents the solid surface of the planet, the blue represents the planetary atmosphere, the dark orange represents the host star, and the distance between the surface of the planet and the maroon ring represents the modeled annulus for each individual subfigure geometry. This figure is not-to-scale as the planetary components are enhanced to show structure and the stellar size is decreased for similar reasoning.

atmosphere it models is not opaque inside the entirety of the annulus. In this modeled scenario, the spectral features become more distinguishable than in Fig. A-2a because a certain percentage of light at each wavelength arrives at the detector. Figure A-2c is the other end of the extreme from Fig. A-2a in that the atmospheric absorption is a very small percentage of removed light in reference to the amount of light that arrives at the detector. For Fig. A-2c, the transmissivity features would be very shallow in comparison to the features from Figs. A-2a and A-2b.

Transmissivity spectra are useful to model as long as the spectra are not saturated (i.e. as long as a large enough annulus is modeled). The key to using transmissivity spectra is not to focus on the absolute value of the transmissivity spectrum as these values would change depending on the annulus modeled (as described above), but rather to utilize the SNR or detectability of the transmissivity spectral features. The importance of drawing conclusions based on the SNR is because the SNR of transmissivity models is conserved regardless of the atmospheric height modeled. Therefore, as long as the spectral features are not saturated (i.e. transmissivity = 0), then the corresponding SNRs and detectability calculations are robust. The fact that the SNR is conserved in this manner is what makes my detectivity results not dependent on the atmospheric height I chose for my models.

Appendix B

Spectral Measurements for the Transmissivity, the Error on the Transmissivity, and the SNR for the Modeled HITRAN Biosignature Gases

In this appendix, I have included the relevant data for each HITRAN biosignature feature analyzed in Chapter 3. The reasoning for separating the tables into this appendix is due to their inherent size. Though the tables are quite large in some cases, the detailed data presented here are very important because they allow for future comparisons and an understanding of the conclusions reached in this study. Looking from the other side, if the tables were not included, one could not validate my data/conclusions with future models with the exception of the SNRs listed in Chapter 3, though even those are only listed in the text for a select set of models.

In order to make the inclusion of data the least confusing as possible, I separate each HITRAN biosignature gas into its own section. As I will describe here how the tables are arranged and as I have already discussed these results earlier in this thesis,

the pre-emptive text for each molecule will be quite limited. The tables are arranged in the same order as the HITRAN molecules are discussed in Chapter 3. The data for every feature is listed for each telescope size and atmospheric abundance before moving onto the next molecular feature. In the tables, the data is listed such that it describes the chosen telescope size for every abundance before moving onto the next telescope size. The order of the telescope sizes is 100 m, 50 m, 35 m, and 20 m.

The telescope sizes and biosignature atmospheric abundances for each particular model are listed in columns 1 and 2, respectively. The in-feature wavelength is listed in column 3 and denoted as λ_{in}. Note that, as some features span multiple wavelength bins, the exact wavelength chosen in this column sometimes changes slightly based on the model. The fourth column is the transmissivity value for the chosen wavelength (designated as T_{in}), while the fifth column is the error on that transmissivity value (designated at $\sigma_{T_{in}}$). The sixth column (λ_{out}) is the wavelength of the comparison baseline. Note that this value sometimes changes based on choosing the most appropriate continuum for each particular model. The seventh and eight columns designate the transmissivity value for the baseline (T_{out}) and the error on that baseline transmissivity ($\sigma_{T_{out}}$), respectively. The calculated SNR, which aids in determining the detectability of a feature, is listed in column 9. With the table introduction finished, I now list the data for each HITRAN biosignature gas model.

B.1 Oxygen

Table B.1: Oxygen Detectability in the Visible Wavelength Region

Telescope Size	Abundance	λ_{in}	T_{in}	$\sigma_{T_{in}}$	λ_{out}	T_{out}	$\sigma_{T_{out}}$	SNR
100 m	100%	765 nm	0.8577	0.0105	775 nm	0.9952	0.0105	9.3
100 m	50%	765 nm	0.8768	0.0105	775 nm	0.9855	0.0106	7.3
100 m	20%	765 nm	0.8922	0.0105	775 nm	0.9816	0.0106	6.0
100 m	1%	765 nm	Indiscernible					
50 m	100%	765 nm	0.8757	0.021	775 nm	0.9881	0.0211	3.8
50 m	50%	765 nm	0.8583	0.021	775 nm	0.9863	0.0211	4.3
50 m	20%	765 nm	0.9064	0.021	775 nm	1.0358	0.0211	4.3
50 m	1%	765 nm	Indiscernible					
35 m	100%	765 nm	0.8428	0.03	775 nm	1.0006	0.0302	3.7
35 m	50%	765 nm	0.8621	0.03	775 nm	0.9791	0.0302	2.7
35 m	20%	765 nm	0.8932	0.03	775 nm	1.0003	0.0302	2.5
35 m	1%	765 nm	Indiscernible					
20 m	100%	765 nm	0.8232	0.0525	775 nm	1.0399	0.0528	2.9
20 m	50%	765 nm	0.8077	0.0525	785 nm	0.98	0.053	2.3
20 m	20%	765 nm	Indiscernible					

B.2 Ozone

Table B.2: Ozone Detectability in the IR Wavelength Region

Telescope Size	O_3 Abundance	λ_{in}	T_{in}	$\sigma_{T_{in}}$	λ_{out}	T_{out}	$\sigma_{T_{out}}$	SNR
100 m	100%	3.25 μm	0.4571	0.0130	3.85 μm	0.7495	0.0163	14.0
100 m	50%	3.25 μm	0.4606	0.0130	3.95 μm	0.7839	0.0165	15.4
100 m	20%	3.35 μm	0.5198	0.0135	3.85 μm	0.8034	0.0163	13.4
100 m	1%	3.25 μm	0.6075	0.0130	3.85 μm	0.9087	0.0163	14.4
100 m	1000 ppm	3.25 μm	0.6843	0.0130	3.85 μm	0.9725	0.0163	13.8
100 m	100 ppm	Indiscernible						
50 m	100%	3.25 μm	0.4528	0.0261	3.85 μm	0.7594	0.0326	7.3
50 m	50%	3.25 μm	0.468	0.0261	3.95 μm	0.7508	0.0331	6.7
50 m	20%	3.25 μm	0.4679	0.0260	3.85 μm	0.7986	0.0326	7.9
50 m	1%	3.25 μm	0.5944	0.0261	3.95 μm	0.9745	0.0331	9.0
50 m	1000 ppm	3.25 μm	0.6891	0.0261	3.95 μm	0.9683	0.0330	6.6
50 m	100 ppm	Indiscernible						
35 m	100%	3.25 μm	0.4016	0.0372	3.85 μm	0.7923	0.0465	6.6
35 m	50%	3.25 μm	0.5365	0.0372	3.95 μm	0.8585	0.0472	5.4
35 m	20%	3.25 μm	0.4717	0.0372	3.85 μm	0.8059	0.0465	5.6
35 m	1%	3.25 μm	0.659	0.0372	3.85 μm	0.9377	0.0465	4.7
35 m	1000 ppm	3.25 μm	0.7297	0.0372	3.95 μm	1.0155	0.0472	4.8
35 m	100 ppm	Indiscernible						
20 m	100%	3.25 μm	0.4583	0.0652	3.85 μm	0.7549	0.0814	2.8
20 m	50%	3.25 μm	0.4802	0.0651	3.85 μm	0.8305	0.0814	3.4
20 m	20%	3.35 μm	0.4293	0.0675	3.95 μm	0.8356	0.0827	3.8
20 m	1%	3.35 μm	0.6209	0.0675	3.85 μm	0.9748	0.0814	3.3
20 m	1000 ppm	3.25 μm	0.5556	0.0651	3.75 μm	0.9673	0.0767	4.1
20 m	100 ppm	Indiscernible						
100 m	100%	3.65 μm	0.4517	0.0151	3.85 μm	0.7495	0.0163	13.4
100 m	50%	3.65 μm	0.5022	0.0151	3.95 μm	0.7839	0.0165	12.6
100 m	20%	3.65 μm	0.5306	0.0151	3.85 μm	0.8034	0.0163	12.3
100 m	1%	3.65 μm	0.6256	0.0151	3.85 μm	0.9087	0.0163	12.7
100 m	1000 ppm	3.65 μm	0.7492	0.0151	3.85 μm	0.9725	0.0163	10.0
100 m	100 ppm	3.65 μm	0.8519	0.0151	3.95 μm	0.9711	0.0165	5.3

Continued on next page

Table B.2 – *Continued from previous page*

Telescope Size	O_3 Abundance	λ_{in}	T_{in}	$\sigma_{T_{in}}$	λ_{out}	T_{out}	$\sigma_{T_{out}}$	SNR
100 m	10 ppm	Indiscernible						
50 m	100%	3.65 μm	0.4471	0.0302	3.85 μm	0.7594	0.0326	7.0
50 m	50%	3.65 μm	0.491	0.0302	3.95 μm	0.7508	0.0331	5.8
50 m	20%	3.65 μm	0.5294	0.0302	3.85 μm	0.7986	0.0326	6.1
50 m	1%	3.65 μm	0.6183	0.0302	3.95 μm	0.9745	0.0331	7.9
50 m	1000 ppm	3.65 μm	0.7689	0.0302	3.95 μm	0.9683	0.0330	4.5
50 m	100 ppm	3.65 μm	0.8506	0.0302	3.85 μm	1.0083	0.0325	3.6
50 m	10 ppm	Indiscernible						
35 m	100%	3.65 μm	0.4495	0.0432	3.85 μm	0.7923	0.0465	5.4
35 m	50%	3.65 μm	0.4868	0.0432	3.95 μm	0.8585	0.0472	5.8
35 m	20%	3.65 μm	0.5531	0.0432	3.85 μm	0.8059	0.0465	4.0
35 m	1%	3.65 μm	0.6451	0.0431	3.85 μm	0.9377	0.0465	4.6
35 m	1000 ppm	3.65 μm	0.8009	0.0432	3.95 μm	1.0155	0.0472	3.4
35 m	100 ppm	Indiscernible						
20 m	100%	3.65 μm	0.4917	0.0756	3.85 μm	0.7549	0.0814	2.4
20 m	50%	3.65 μm	0.4124	0.0756	3.85 μm	0.8305	0.0814	3.8
20 m	20%	3.65 μm	0.5019	0.0756	3.95 μm	0.8356	0.0827	3.0
20 m	1%	3.65 μm	0.6294	0.0756	3.85 μm	0.9748	0.0814	3.1
20 m	1000 ppm	3.65 μm	0.7157	0.0755	3.75 μm	0.9673	0.0767	2.3
20 m	100 ppm	Indiscernible						
100 m	100%	4.85 μm	0.2789	0.0221	3.85 μm	0.7495	0.0163	17.1
100 m	50%	4.75 μm	0.2963	0.0213	3.95 μm	0.7839	0.0165	18.1
100 m	20%	4.75 μm	0.2899	0.0213	3.85 μm	0.8034	0.0163	19.1
100 m	1%	4.75 μm	0.3965	0.0213	3.85 μm	0.9087	0.0163	19.1
100 m	1000 ppm	4.75 μm	0.5105	0.0213	3.85 μm	0.9725	0.0163	17.2
100 m	100 ppm	4.75 μm	0.6155	0.0213	3.95 μm	0.9711	0.0165	13.2
100 m	10 ppm	4.75μm	0.6946	0.0213	4.35 μm	0.9948	0.0191	10.5
100 m	1 ppm	Indiscernible						
50 m	100%	4.85 μm	0.2883	0.0442	3.85 μm	0.7594	0.0326	8.6
50 m	50%	4.75 μm	0.2871	0.0426	3.95 μm	0.7508	0.0331	8.6
50 m	20%	4.75 μm	0.3366	0.0426	3.85 μm	0.7986	0.0326	8.6
50 m	1%	4.75 μm	0.4776	0.0426	3.95 μm	0.9745	0.0331	9.2
50 m	1000 ppm	4.75 μm	0.5137	0.0426	3.95 μm	0.9683	0.0330	8.4

Continued on next page

Table B.2 – *Continued from previous page*

Telescope Size	O_3 Abundance	λ_{in}	T_{in}	$\sigma_{T_{in}}$	λ_{out}	T_{out}	$\sigma_{T_{out}}$	SNR
50 m	100 ppm	4.75 μm	0.5743	0.0426	3.85 μm	1.0083	0.0325	8.1
50 m	10 ppm	4.75 μm	0.7145	0.0426	4.55 μm	0.9738	0.0404	4.4
50 m	1 ppm	Indiscernible						
35 m	100%	4.75 μm	0.2754	0.0609	3.85 μm	0.7923	0.0465	6.7
35 m	50%	4.85 μm	0.2357	0.0631	3.95 μm	0.8585	0.0472	7.9
35 m	20%	4.75 μm	0.3797	0.0609	3.85 μm	0.8059	0.0465	5.6
35 m	1%	4.85 μm	0.4126	0.0631	3.85 μm	0.9377	0.0465	6.7
35 m	1000 ppm	4.75 μm	0.4388	0.0609	3.95 μm	1.0155	0.0472	7.5
35 m	100 ppm	4.75 μm	0.4539	0.0609	5.05 μm	0.9071	0.0654	5.1
35 m	10 ppm	4.75 μm	0.6598	0.0609	4.55 μm	0.957	0.0576	3.5
35 m	1 ppm	Indiscernible						
20 m	100%	4.75 μm	0.2477	0.1066	3.85 μm	0.7549	0.0814	3.8
20 m	50%	4.85 μm	0.2401	0.1104	3.85 μm	0.8305	0.0814	4.3
20 m	20%	4.75 μm	0.1929	0.1066	3.95 μm	0.8356	0.0827	4.8
20 m	1%	4.75 μm	0.3254	0.1065	3.85 μm	0.9748	0.0814	4.8
20 m	1000 ppm	4.75 μm	0.2647	0.1065	3.75 μm	0.9673	0.0767	5.4
20 m	100 ppm	Indiscernible						
100 m	100%	5.75 μm	0.3829	0.0275	3.85 μm	0.7495	0.0163	11.5
100 m	50%	5.75 μm	0.3946	0.0275	3.95 μm	0.7839	0.0165	12.1
100 m	20%	5.75 μm	0.4311	0.0275	3.85 μm	0.8034	0.0163	11.6
100 m	1%	5.75 μm	0.5472	0.0275	3.85 μm	0.9087	0.0163	11.3
100 m	1000 ppm	Indiscernible						
50 m	100%	5.75 μm	0.4109	0.0551	3.85 μm	0.7594	0.0326	5.4
50 m	50%	5.85 μm	0.3951	0.0563	3.95 μm	0.7508	0.0331	5.4
50 m	20%	5.75 μm	0.3567	0.0550	3.85 μm	0.7986	0.0326	6.9
50 m	1%	5.75 μm	0.4781	0.0550	3.95 μm	0.9745	0.0331	7.7
50 m	1000 ppm	Indiscernible						
35 m	100%	5.65 μm	0.3294	0.0768	3.85 μm	0.7923	0.0465	5.2
35 m	50%	5.65 μm	0.3446	0.0768	3.95 μm	0.8585	0.0472	5.7
35 m	20%	5.75 μm	0.3441	0.0786	3.85 μm	0.8059	0.0465	5.1
35 m	1%	5.85 μm	0.421	0.0804	3.85 μm	0.9377	0.0465	5.6
35 m	1000 ppm	Indiscernible						
20 m	100%	5.75 μm	0.3481	0.1376	3.85 μm	0.7549	0.0814	2.5

Continued on next page

Table B.2 – *Continued from previous page*

Telescope Size	O_3 Abundance	λ_{in}	T_{in}	$\sigma_{T_{in}}$	λ_{out}	T_{out}	$\sigma_{T_{out}}$	SNR
20 m	50%	5.75 μm	0.1045	0.1376	3.85 μm	0.8305	0.0814	4.5
20 m	20%	5.75 μm	0.2885	0.1376	3.95 μm	0.8356	0.0827	3.4
20 m	1%	5.85 μm	0.2561	0.1407	3.85 μm	0.9748	0.0814	4.4
20 m	1000 ppm	Indiscernible						
100 m	100%	9.55 μm	0.2336	0.0567	7.85 μm	0.8891	0.0433	9.2
100 m	50%	9.65 μm	0.2141	0.0571	7.85 μm	0.8626	0.0433	9.0
100 m	20%	9.65 μm	0.2125	0.0571	7.85 μm	0.8798	0.0433	9.3
100 m	1%	9.65 μm	0.3287	0.0571	7.95 μm	0.8728	0.0434	7.6
100 m	1000 ppm	9.65 μm	0.3978	0.0571	8.05 μm	0.8753	0.0442	6.6
100 m	100 ppm	9.75 μm	0.4862	0.0581	8.35 μm	0.926	0.0461	5.9
100 m	10 ppm	9.65 μm	0.5236	0.0570	9.15 μm	0.9253	0.0525	5.2
100 m	1 ppm	9.65 μm	0.7578	0.0570	8.65 μm	1.0119	0.0486	3.4
100 m	100 ppb	9.55 μm	0.8242	0.0567	9.25 μm	0.9976	0.0536	2.2
100 m	10 ppb	Indiscernible						
50 m	100%	9.55 μm	0.1053	0.1134	7.85 μm	0.916	0.0866	5.7
50 m	50%	9.45 μm	0.2101	0.1120	7.95 μm	0.8949	0.0868	4.8
50 m	20%	9.55 μm	0.3335	0.1134	7.95 μm	0.7605	0.0868	3.0
50 m	1%	9.55 μm	0.2867	0.1134	7.65 μm	0.9891	0.0825	5.0
50 m	1000 ppm	9.55 μm	0.4537	0.1135	7.65 μm	0.9193	0.0825	3.3
50 m	100 ppm	9.65 μm	0.4373	0.1142	9.35 μm	0.8019	0.1090	2.3
50 m	10 ppm	9.55 μm	0.5682	0.1135	9.15 μm	0.8964	0.1049	2.1
50 m	1 ppm	9.55 μm	0.4807	0.1135	8.95 μm	1.0184	0.1027	3.5
50 m	100 ppb	Indiscernible						
35 m	100%	9.65 μm	0.3195	0.1630	7.85 μm	0.8139	0.1236	2.4
35 m	50%	9.45 μm	0.3197	0.1600	7.85 μm	0.9706	0.1236	3.2
35 m	20%	9.65 μm	0.44	0.1630	7.85 μm	0.8458	0.1236	2.0
35 m	1%	9.65 μm	0.4142	0.1630	7.85 μm	1.0117	0.1236	2.9
35 m	1000 ppm	9.45 μm	0.4757	0.1599	8.25 μm	0.8077	0.1314	1.6
35 m	100 ppm	9.65 μm	0.5599	0.1630	8.64 μm	0.892	0.1388	1.6
35 m	10 ppm	Indiscernible						
20 m	100%	Indiscernible						

B.3 Methane

Table B.3: Methane Detectability in the IR Wavelength Region

Telescope Size	CH_4 Abundance	λ_{in}	T_{in}	$\sigma_{T_{in}}$	λ_{out}	T_{out}	$\sigma_{T_{out}}$	SNR
100 m	100%	2.35 μm	0.5093	0.0082	2.05 μm	0.8818	0.0074	33.7
100 m	50%	2.35 μm	0.5132	0.0086	2.05 μm	0.8855	0.0074	32.8
100 m	20%	2.35 μm	0.5585	0.0086	2.05 μm	0.9074	0.0074	30.8
100 m	1%	2.35 μm	0.6417	0.0086	2.05 μm	0.9437	0.0074	26.6
100 m	1000 ppm	2.35 μm	0.7068	0.0086	2.05 μm	0.9408	0.0074	20.6
100 m	100 ppm	2.35 μm	0.7881	0.0086	2.05 μm	0.9545	0.0074	14.7
100 m	10 ppm	Indiscernible						
50 m	100%	2.25 μm	0.4774	0.0164	2.05 μm	0.8648	0.0148	17.5
50 m	50%	2.25 μm	0.5261	0.0164	2.05 μm	0.8882	0.0148	16.4
50 m	20%	2.25 μm	0.5353	0.0164	2.05 μm	0.9127	0.0148	17.1
50 m	1%	2.35 μm	0.6118	0.0172	2.05 μm	0.9241	0.0148	13.8
50 m	1000 ppm	2.35 μm	0.6948	0.0172	2.05 μm	0.9287	0.0148	10.3
50 m	100 ppm	2.35 μm	0.7802	0.0173	2.05 μm	0.9663	0.0148	8.2
50 m	10 ppm	Indiscernible						
35 m	100%	2.35 μm	0.5069	0.0246	2.05 μm	0.8689	0.0211	11.2
35 m	50%	2.25 μm	0.4984	0.0234	2.05 μm	0.9293	0.0211	13.7
35 m	20%	2.25 μm	0.5275	0.0234	2.05 μm	0.9586	0.0211	13.7
35 m	1%	2.35 μm	0.6230	0.0246	2.05 μm	0.9642	0.0211	10.5
35 m	1000 ppm	2.35 μm	0.6953	0.0246	2.05 μm	0.9506	0.0211	7.9
35 m	100 ppm	2.35 μm	0.7686	0.0246	2.05 μm	0.9682	0.0211	6.2
35 m	10 ppm	Indiscernible						
20 m	100%	2.25 μm	0.5019	0.0409	2.05 μm	0.8729	0.0369	6.7
20 m	50%	2.25 μm	0.5459	0.0409	2.05 μm	0.8729	0.0369	5.9
20 m	20%	2.25 μm	0.5534	0.0409	2.05 μm	0.9033	0.0369	6.4
20 m	1%	2.35 μm	0.6058	0.0431	2.05 μm	0.9356	0.0369	5.8
20 m	1000 ppm	2.25 μm	0.7230	0.0410	2.05 μm	0.9543	0.0369	4.2
20 m	100 ppm	2.25 μm	0.7249	0.0410	2.05 μm	0.9271	0.0369	3.7
20 m	10 ppm	Indiscernible						
100 m	100%	3.35 μm	0.4639	0.0135	2.05 μm	0.8818	0.0074	27.1
100 m	50%	3.35 μm	0.4357	0.0135	2.05 μm	0.8855	0.0074	29.2
100 m	20%	3.35 μm	0.4787	0.0135	2.05 μm	0.9074	0.0074	27.8

Continued on next page

Table B.3 – *Continued from previous page*

Telescope Size	CH_4 Abundance	λ_{in}	T_{in}	$\sigma_{T_{in}}$	λ_{out}	T_{out}	$\sigma_{T_{out}}$	SNR
100 m	1%	3.35 μm	0.5812	0.0135	2.05 μm	0.9437	0.0074	23.5
100 m	1000 ppm	3.35 μm	0.6597	0.0135	2.05 μm	0.9408	0.0074	18.3
100 m	100 ppm	3.25 μm	0.7288	0.0130	2.05 μm	0.9545	0.0074	15.1
100 m	10 ppm	Indiscernible						
50 m	100%	3.35 μm	0.4273	0.0270	2.05 μm	0.8648	0.0148	14.2
50 m	50%	3.35 μm	0.4557	0.0270	2.05 μm	0.8882	0.0148	14.0
50 m	20%	3.35 μm	0.4643	0.0270	2.05 μm	0.9127	0.0148	14.6
50 m	1%	3.35 μm	0.5975	0.0270	2.05 μm	0.9241	0.0148	10.6
50 m	1000 ppm	3.35 μm	0.6605	0.0270	2.05 μm	0.9287	0.0148	8.7
50 m	100 ppm	3.25 μm	0.6938	0.0260	2.05 μm	0.9663	0.0148	9.1
50 m	10 ppm	Indiscernible						
35 m	100%	3.35 μm	0.4297	0.0386	2.05 μm	0.8689	0.0211	10.0
35 m	50%	3.35 μm	0.3983	0.0386	2.05 μm	0.9293	0.0211	12.1
35 m	20%	3.45 μm	0.4183	0.0400	2.05 μm	0.9586	0.0211	11.9
35 m	1%	3.35 μm	0.6092	0.0386	2.05 μm	0.9642	0.0211	8.1
35 m	1000 ppm	3.45 μm	0.6023	0.0401	2.05 μm	0.9506	0.0211	7.7
35 m	100 ppm	3.25 μm	0.7112	0.0372	2.05 μm	0.9682	0.0211	6.0
35 m	10 ppm	Indiscernible						
20 m	100%	3.35 μm	0.4645	0.0676	2.05 μm	0.8729	0.0369	5.3
20 m	50%	3.35 μm	0.4479	0.0675	2.05 μm	0.8729	0.0369	5.5
20 m	20%	3.45 μm	0.3988	0.0701	2.05 μm	0.9033	0.0369	6.4
20 m	1%	3.45 μm	0.5510	0.0701	2.05 μm	0.9356	0.0369	4.9
20 m	1000 ppm	3.25 μm	0.5654	0.0651	2.05 μm	0.9543	0.0369	5.2
20 m	100 ppm	3.25 μm	0.7216	0.0651	2.05 μm	0.9271	0.0369	2.7
20 m	10 ppm	Indiscernible						
100 m	100%	7.85 μm	0.4710	0.0304	5.05 μm	0.8500	0.0163	11.0
100 m	50%	7.85 μm	0.4521	0.0304	4.85 μm	0.8509	0.0157	11.7
100 m	20%	7.65 μm	0.4572	0.0294	4.85 μm	0.8583	0.0157	12.0
100 m	1%	7.85 μm	0.6066	0.0304	4.65 μm	0.9063	0.0147	8.9
100 m	1000 ppm	7.85 μm	0.6792	0.0304	4.85 μm	0.8717	0.0157	5.6
100 m	100 ppm	7.85 μm	0.6924	0.0304	4.45 μm	0.9651	0.0138	8.2
100 m	10 ppm	Indiscernible						
50 m	100%	7.85 μm	0.5464	0.0604	4.85 μm	0.8411	0.0307	4.3

Continued on next page

Table B.3 – *Continued from previous page*

Telescope Size	CH_4 Abundance	λ_{in}	T_{in}	$\sigma_{T_{in}}$	λ_{out}	T_{out}	$\sigma_{T_{out}}$	SNR
50 m	50%	7.85 μm	0.5078	0.0607	4.85 μm	0.8256	0.0313	4.7
50 m	20%	7.85 μm	0.3982	0.0607	5.05 μm	0.8481	0.0325	6.5
50 m	1%	7.85 μm	0.6835	0.0604	4.25 μm	0.8837	0.0260	3.0
50 m	1000 ppm	7.85 μm	0.7533	0.0608	4.45 μm	0.9889	0.0275	3.5
50 m	100 ppm	7.85 μm	0.7601	0.0607	4.45 μm	0.9841	0.0275	3.4
50 m	10 ppm	Indiscernible						
35 m	100%	7.85 μm	0.5652	0.0868	5.05 μm	0.8464	0.0465	2.9
35 m	50%	7.85 μm	0.4682	0.0868	5.25 μm	0.8622	0.0496	3.9
35 m	20%	7.85 μm	0.4464	0.0868	5.05 μm	0.8292	0.0465	3.9
35 m	1%	7.85 μm	0.6509	0.0868	5.25 μm	0.7906	0.0496	1.4
35 m	1000 ppm	8.45 μm	0.6741	0.0963	4.45 μm	0.9449	0.0393	2.6
35 m	100 ppm	7.85 μm	0.8116	0.0868	4.25 μm	0.9863	0.0366	1.9
35 m	10 ppm	Indiscernible						
20 m	100%	7.85 μm	0.4259	0.1518	5.05 μm	0.7942	0.0813	2.1
20 m	50%	7.45 μm	0.4162	0.1410	5.25 μm	0.7733	0.0868	2.2
20 m	20%	8.05 μm	0.4596	0.1559	5.45 μm	0.7432	0.0915	1.6
20 m	1%	8.25 μm	0.5612	0.1633	4.85 μm	0.8376	0.0783	1.5
20 m	1000 ppm	Indiscernible						

B.4 Nitrous Oxide

Table B.4: Nitrous Oxide Detectability in the IR Wavelength Region

Telescope Size	N_2O Abundance	λ_{in}	T_{in}	$\sigma_{T_{in}}$	λ_{out}	T_{out}	$\sigma_{T_{out}}$	SNR
100 m	100%	4.05 μm	0.4765	0.0172	3.35 μm	0.8553	0.0135	17.3
100 m	50%	4.05 μm	0.4975	0.0172	3.35 μm	0.8445	0.0135	15.9
100 m	20%	4.05 μm	0.5425	0.0172	3.75 μm	0.8634	0.0154	13.9
100 m	1%	4.05 μm	0.5989	0.0172	3.75 μm	0.9092	0.0154	13.4
100 m	1000 ppm	4.05 μm	0.6778	0.0172	3.75 μm	0.9058	0.0153	9.9
100 m	100 ppm	4.05 μm	0.7580	0.0172	3.75 μm	0.9268	0.0154	7.3
100 m	10 ppm	4.05 μm	0.8640	0.0172	4.15 μm	0.9618	0.0178	4.0
100 m	1 ppm	Indiscernible						
50 m	100%	4.05 μm	0.4493	0.0344	3.35 μm	0.8641	0.0270	9.5
50 m	50%	4.05 μm	0.5286	0.0344	3.75 μm	0.8539	0.0307	7.1
50 m	20%	4.05 μm	0.5142	0.0344	3.75 μm	0.8288	0.0307	6.8
50 m	1%	4.05 μm	0.5938	0.0344	3.75 μm	0.9028	0.0307	6.7
50 m	1000 ppm	3.95 μm	0.7234	0.0331	3.75 μm	0.9066	0.0307	4.1
50 m	100 ppm	4.05 μm	0.7633	0.0344	3.75 μm	0.9191	0.0307	3.4
50 m	10 ppm	4.05 μm	0.8221	0.0344	4.15 μm	0.9434	0.0356	2.5
50 m	1 ppm	Indiscernible						
35 m	100%	4.05 μm	0.3922	0.0492	3.35 μm	0.8414	0.0386	7.2
35 m	50%	4.05 μm	0.4588	0.0492	3.75 μm	0.8798	0.0439	6.4
35 m	20%	4.05 μm	0.5096	0.0492	3.75 μm	0.8646	0.0439	5.4
35 m	1%	4.05 μm	0.5522	0.0492	3.75 μm	0.9153	0.0439	5.5
35 m	1000 ppm	3.85 μm	0.6912	0.0465	3.75 μm	0.9551	0.0439	4.1
35 m	100 ppm	4.05 μm	0.7749	0.0492	3.75 μm	0.9141	0.0438	2.1
35 m	10 ppm	4.05 μm	0.7836	0.0492	3.75 μm	0.9760	0.0439	2.9
35 m	1 ppm	Indiscernible						
20 m	100%	4.05 μm	0.4315	0.0860	3.35 μm	0.8587	0.0676	3.9
20 m	50%	4.05 μm	0.3839	0.0860	3.35 μm	0.8286	0.0676	4.1
20 m	20%	4.05 μm	0.4644	0.0860	3.75 μm	0.8591	0.0768	3.4
20 m	1%	4.05 μm	0.6694	0.0861	3.75 μm	0.8635	0.0768	1.7
20 m	1000 ppm	4.05 μm	0.6367	0.0861	3.45 μm	0.9815	0.0700	3.1
20 m	100 ppm	3.95 μm	0.7413	0.0826	3.75 μm	0.9052	0.0767	1.5
20 m	10 ppm	Indiscernible						

Continued on next page

Table B.4 – *Continued from previous page*

Telescope Size	N_2O Abundance	λ_{in}	T_{in}	$\sigma_{T_{in}}$	λ_{out}	T_{out}	$\sigma_{T_{out}}$	SNR
100 m	100%	4.55 μm	0.3991	0.0202	3.35 μm	0.8553	0.0135	18.8
100 m	50%	4.55 μm	0.3846	0.0202	3.35 μm	0.8445	0.0135	18.9
100 m	20%	4.55 μm	0.4224	0.0202	3.75 μm	0.8634	0.0154	17.4
100 m	1%	4.55 μm	0.4784	0.0202	3.75 μm	0.9092	0.0154	17.0
100 m	1000 ppm	4.55 μm	0.5417	0.0202	3.75 μm	0.9058	0.0153	14.4
100 m	100 ppm	4.55 μm	0.5574	0.0201	3.75 μm	0.9268	0.0154	14.6
100 m	10 ppm	4.55 μm	0.7023	0.0201	4.15 μm	0.9618	0.0178	9.7
100 m	1 ppm	4.55 μm	0.7321	0.0201	4.35 μm	0.9888	0.0191	9.3
100 m	100 ppb	4.55 μm	0.8325	0.0201	4.35 μm	0.9646	0.0191	4.8
100 m	10 ppb	Indiscernible						
50 m	100%	4.55 μm	0.3716	0.0403	3.35 μm	0.8641	0.0270	10.2
50 m	50%	4.55 μm	0.3814	0.0403	3.75 μm	0.8539	0.0307	9.3
50 m	20%	4.55 μm	0.4992	0.0403	3.75 μm	0.8288	0.0307	6.5
50 m	1%	4.55 μm	0.3797	0.0403	3.75 μm	0.9028	0.0307	10.3
50 m	1000 ppm	4.55 μm	0.5293	0.0403	3.75 μm	0.9066	0.0307	7.4
50 m	100 ppm	4.55 μm	0.6336	0.0403	3.75 μm	0.9191	0.0307	5.6
50 m	10 ppm	4.55 μm	0.6958	0.0403	4.15 μm	0.9434	0.0356	4.6
50 m	1 ppm	Indiscernible						
35 m	100%	4.55 μm	0.3672	0.0561	3.35 μm	0.8414	0.0386	7.0
35 m	50%	4.55 μm	0.3924	0.0576	3.75 μm	0.8798	0.0439	6.7
35 m	20%	4.45 μm	0.4390	0.0561	3.75 μm	0.8646	0.0439	6.0
35 m	1%	4.55 μm	0.4550	0.0576	3.75 μm	0.9153	0.0439	6.4
35 m	1000 ppm	4.45 μm	0.5487	0.0561	3.75 μm	0.9551	0.0439	5.7
35 m	100 ppm	4.55 μm	0.6393	0.0576	3.75 μm	0.9141	0.0438	3.8
35 m	10 ppm	4.55 μm	0.6547	0.0576	3.75 μm	0.9760	0.0439	4.4
35 m	1 ppm	Indiscernible						
20 m	100%	4.65 μm	0.2591	0.1035	3.35 μm	0.8587	0.0676	4.9
20 m	50%	4.65 μm	0.3007	0.1035	3.35 μm	0.8286	0.0676	4.3
20 m	20%	4.55 μm	0.4171	0.1008	3.75 μm	0.8591	0.0768	3.5
20 m	1%	4.55 μm	0.3988	0.1008	3.75 μm	0.8635	0.0768	3.7
20 m	1000 ppm	4.55 μm	0.3881	0.1008	3.45 μm	0.9815	0.0700	4.8
20 m	100 ppm	4.65 μm	0.6347	0.1036	3.75 μm	0.9052	0.0767	2.1
20 m	10 ppm	Indiscernible						

Continued on next page

Table B.4 – *Continued from previous page*

Telescope Size	N_2O Abundance	λ_{in}	T_{in}	$\sigma_{T_{in}}$	λ_{out}	T_{out}	$\sigma_{T_{out}}$	SNR
100 m	100%	7.85 μm	0.4157	0.0298	9.25 μm	0.8293	0.0387	8.5
100 m	50%	7.65 μm	0.3868	0.0297	9.05 μm	0.8728	0.0369	10.3
100 m	20%	7.65 μm	0.4482	0.0297	9.05 μm	0.8505	0.0369	8.5
100 m	1%	7.85 μm	0.4914	0.0299	4.85 μm	0.8997	0.0153	12.2
100 m	1000 ppm	7.65 μm	0.5946	0.0297	9.05 μm	0.9656	0.0369	7.8
100 m	100 ppm	7.85 μm	0.6143	0.0299	9.05 μm	0.9689	0.0369	7.5
100 m	10 ppm	7.65 μm	0.6686	0.0297	9.05 μm	0.9766	0.0369	6.5
100 m	1 ppm	Indiscernible						
50 m	100%	7.65 μm	0.4530	0.0593	9.25 μm	0.8111	0.0774	3.7
50 m	50%	7.85 μm	0.4291	0.0597	9.05 μm	0.8759	0.0738	4.7
50 m	20%	7.65 μm	0.4047	0.0594	9.05 μm	0.8536	0.0738	4.7
50 m	1%	7.65 μm	0.4902	0.0594	4.85 μm	0.8949	0.0307	6.1
50 m	1000 ppm	7.65 μm	0.5975	0.0594	8.25 μm	0.9015	0.0643	3.5
50 m	100 ppm	7.65 μm	0.6301	0.0594	9.05 μm	0.9695	0.0738	3.6
50 m	10 ppm	Indiscernible						
35 m	100%	7.65 μm	0.2938	0.0848	9.05 μm	0.8907	0.1054	4.4
35 m	50%	7.85 μm	0.3400	0.0853	9.05 μm	0.8644	0.1054	3.9
35 m	20%	7.85 μm	0.4150	0.0853	9.45 μm	0.9101	0.1124	3.5
35 m	1%	8.05 μm	0.4171	0.0900	7.25 μm	0.8865	0.0771	4.0
35 m	1000 ppm	8.05 μm	0.5415	0.0900	6.25 μm	0.8467	0.0629	2.8
35 m	100 ppm	7.85 μm	0.5302	0.0853	9.05 μm	0.9185	0.1054	2.9
35 m	10 ppm	Indiscernible						
20 m	100%	7.65 μm	0.3875	0.1484	6.45 μm	0.9119	0.1149	2.8
20 m	50%	7.65 μm	0.4292	0.1484	7.05 μm	0.9382	0.1286	2.6
20 m	20%	7.65 μm	0.1468	0.1484	6.85 μm	0.7912	0.1259	3.3
20 m	1%	8.05 μm	0.2644	0.1576	8.85 μm	0.9971	0.1802	3.1
20 m	1000 ppm	7.65 μm	0.3384	0.1484	7.85 μm	0.8112	0.1493	2.2
20 m	100 ppm	7.85 μm	0.3725	0.1493	7.25 μm	0.9185	0.1349	2.7
20 m	10 ppm	Indiscernible						
100 m	100%	8.65 μm	0.4634	0.0345	9.25 μm	0.8293	0.0387	7.1
100 m	50%	8.65 μm	0.4942	0.0345	9.05 μm	0.8728	0.0369	7.5
100 m	20%	8.65 μm	0.5016	0.0345	9.05 μm	0.8505	0.0369	6.9
100 m	1%	8.65 μm	0.6110	0.0345	4.85 μm	0.8997	0.0153	7.6

Continued on next page

Table B.4 – *Continued from previous page*

Telescope Size	N_2O Abundance	λ_{in}	T_{in}	$\sigma_{T_{in}}$	λ_{out}	T_{out}	$\sigma_{T_{out}}$	SNR
100 m	1000 ppm	8.65 μm	0.6722	0.0345	9.05 μm	0.9656	0.0369	5.8
100 m	100 ppm	8.45 μm	0.7315	0.0338	9.05 μm	0.9689	0.0369	4.7
100 m	10 ppm	8.45 μm	0.8255	0.0338	9.05 μm	0.9766	0.0369	3.0
100 m	1 ppm	Indiscernible						
50 m	100%	8.45 μm	0.4713	0.0676	9.25 μm	0.8111	0.0774	3.3
50 m	50%	8.65 μm	0.3713	0.0690	9.05 μm	0.8759	0.0738	5.0
50 m	20%	8.45 μm	0.4088	0.0676	9.05 μm	0.8536	0.0738	4.4
50 m	1%	8.65 μm	0.5323	0.0690	4.85 μm	0.8949	0.0307	4.8
50 m	1000 ppm	8.45 μm	0.6659	0.0676	8.25 μm	0.9015	0.0643	2.5
50 m	100 ppm	8.45 μm	0.6187	0.0676	9.05 μm	0.9695	0.0738	3.5
50 m	10 ppm	8.65 μm	0.7693	0.0690	8.85 μm	0.9813	0.0720	2.1
50 m	1 ppm	Indiscernible						
35 m	100%	8.65 μm	0.3502	0.0986	9.05 μm	0.8907	0.1054	3.7
35 m	50%	8.65 μm	0.5458	0.0986	9.05 μm	0.8644	0.1054	2.2
35 m	20%	8.85 μm	0.4919	0.1029	9.45 μm	0.9101	0.1124	2.7
35 m	1%	8.85 μm	0.5584	0.1029	7.25 μm	0.8865	0.0771	2.6
35 m	1000 ppm	8.85 μm	0.6166	0.1030	6.25 μm	0.8467	0.0629	1.9
35 m	100 ppm	8.45 μm	0.7465	0.0966	9.05 μm	0.9185	0.1054	1.2
35 m	10 ppm	Indiscernible						
20 m	100%	8.45 μm	0.4429	0.1691	6.45 μm	0.9119	0.1149	2.3
20 m	50%	8.65 μm	0.3970	0.1726	7.05 μm	0.9382	0.1286	2.5
20 m	20%	8.45 μm	0.6616	0.1690	9.05 μm	0.8558	0.1845	0.8
20 m	1%	8.45 μm	0.4581	0.1689	8.85 μm	0.9971	0.1802	2.2
20 m	1000 ppm	8.45 μm	0.5254	0.1690	7.85 μm	0.8112	0.1493	1.3
20 m	100 ppm	8.45 μm	0.5379	0.1690	7.25 μm	0.9185	0.1349	1.8
20 m	10 ppm	Indiscernible						

B.5 Methyl Bromide

Table B.5: Methyl Bromide Detectability in the IR Wavelength Region

Telescope Size	CH_3Br Abundance	λ_{in}	T_{in}	$\sigma_{T_{in}}$	λ_{out}	T_{out}	$\sigma_{T_{out}}$	SNR
100 m	100%	7.625 μm	0.3405	0.0261	4.375 μm	0.9886	0.0121	22.5
100 m	50%	7.625 μm	0.3084	0.0261	4.375 μm	0.9802	0.0121	23.4
100 m	20%	7.625 μm	0.3404	0.0261	4.375 μm	0.9860	0.0121	22.4
100 m	1%	7.625 μm	0.4028	0.0261	4.125 μm	0.9993	0.0112	21.0
100 m	1000 ppm	7.625 μm	0.5297	0.0261	4.125 μm	0.9956	0.0112	16.4
100 m	100 ppm	7.625 μm	0.6037	0.0261	4.375 μm	0.9665	0.0121	12.6
100 m	10 ppm	Indiscernible						
50 m	100%	7.875 μm	0.3587	0.0535	4.125 μm	1.0085	0.0225	11.2
50 m	50%	7.625 μm	0.3311	0.0522	4.125 μm	0.9900	0.0225	11.6
50 m	20%	7.625 μm	0.3864	0.0522	4.125 μm	1.0080	0.0225	10.9
50 m	1%	7.625 μm	0.4700	0.0522	4.375 μm	0.9714	0.0242	8.7
50 m	1000 ppm	7.625 μm	0.4134	0.0522	4.125 μm	0.9862	0.0225	10.1
50 m	100 ppm	7.625 μm	0.5186	0.0522	4.125 μm	0.9845	0.0225	8.2
50 m	10 ppm	Indiscernible						
35 m	100%	7.625 μm	0.2271	0.0746	3.875 μm	0.9865	0.0294	9.5
35 m	50%	7.625 μm	0.2847	0.0746	3.875 μm	0.9690	0.0294	8.5
35 m	20%	7.625 μm	0.2020	0.0746	4.125 μm	1.0067	0.0321	9.9
35 m	1%	7.625 μm	0.4255	0.0746	4.625 μm	0.9718	0.0371	6.6
35 m	1000 ppm	7.625 μm	0.4871	0.0746	4.375 μm	0.9770	0.0346	6.0
35 m	100 ppm	7.625 μm	0.6123	0.0746	4.375 μm	0.9922	0.0346	4.6
35 m	10 ppm	Indiscernible						
20 m	100%	7.375 μm	0.4153	0.1230	4.375 μm	0.9729	0.0606	4.1
20 m	50%	7.625 μm	0.3767	0.1306	4.125 μm	0.9842	0.0562	4.3
20 m	20%	7.875 μm	0.3577	0.1339	4.875 μm	0.9988	0.0697	4.2
20 m	1%	7.625 μm	0.5205	0.1306	4.375 μm	1.0039	0.0606	3.4
20 m	1000 ppm	6.875 μm	0.3461	0.1123	3.875 μm	0.9854	0.0514	5.2
20 m	100 ppm	Indiscernible						
100 m	100%	10.625 μm	0.3279	0.0413	4.375 μm	0.9886	0.0121	15.4
100 m	50%	10.375 μm	0.3183	0.0403	4.375 μm	0.9802	0.0121	15.7
100 m	20%	10.375 μm	0.3479	0.0403	4.375 μm	0.9860	0.0121	15.2
100 m	1%	10.375 μm	0.4222	0.0403	4.125 μm	0.9993	0.0112	13.8

Continued on next page

Table B.5 – *Continued from previous page*

Telescope Size	CH_3Br Abundance	λ_{in}	T_{in}	$\sigma_{T_{in}}$	λ_{out}	T_{out}	$\sigma_{T_{out}}$	SNR
100 m	1000 ppm	10.125 μm	0.4922	0.0393	4.125 μm	0.9956	0.0112	12.3
100 m	100 ppm	10.625 μm	0.6299	0.0413	4.375 μm	0.9665	0.0121	7.8
100 m	10 ppm	10.125 μm	0.6731	0.0393	4.375 μm	1.0046	0.0242	7.2
100 m	1 ppm	10.375 μm	0.8509	0.0403	4.125 μm	0.9990	0.0112	3.5
100 m	100 ppb	Indiscernible						
50 m	100%	10.625 μm	0.3793	0.0826	4.125 μm	1.0085	0.0225	7.3
50 m	50%	10.375 μm	0.3043	0.0806	4.125 μm	0.9900	0.0225	8.2
50 m	20%	10.875 μm	0.2998	0.0852	4.125 μm	1.0080	0.0225	8.0
50 m	1%	10.875 μm	0.4735	0.0853	4.375 μm	0.9714	0.0242	5.6
50 m	1000 ppm	10.625 μm	0.4336	0.0826	4.125 μm	0.9862	0.0225	6.5
50 m	100 ppm	10.375 μm	0.6493	0.0807	4.125 μm	0.9845	0.0225	4.0
50 m	10 ppm	10.375 μm	0.7199	0.0807	4.375 μm	1.0046	0.0242	3.4
50 m	1 ppm	Indiscernible						
35 m	100%	10.875 μm	0.3789	0.1218	3.875 μm	0.9865	0.0294	4.8
35 m	50%	10.875 μm	0.1401	0.1218	3.875 μm	0.9690	0.0294	6.6
35 m	20%	10.625 μm	0.3840	0.1180	4.125 μm	1.0067	0.0321	5.1
35 m	1%	10.625 μm	0.4081	0.1181	4.625 μm	0.9718	0.0371	4.6
35 m	1000 ppm	10.625 μm	0.5165	0.1181	4.375 μm	0.9770	0.0346	3.7
35 m	100 ppm	10.375 μm	0.5716	0.1152	4.375 μm	0.9922	0.0346	3.5
35 m	10 ppm	Indiscernible						
20 m	100%	10.625 μm	0.2962	0.2066	4.375 μm	0.9729	0.0606	3.1
20 m	50%	10.875 μm	0.1824	0.2131	4.125 μm	0.9842	0.0562	3.6
20 m	20%	10.875 μm	0.3040	0.2131	4.875 μm	0.9988	0.0697	3.1
20 m	1%	10.375 μm	0.4442	0.2015	4.375 μm	1.0039	0.0606	2.7
20 m	1000 ppm	10.875 μm	0.3598	0.2132	3.875 μm	0.9854	0.0514	2.9
20 m	100 ppm	Indiscernible						

B.6 Methyl Chloride

Table B.6: Methyl Chloride Detectability in the IR Wavelength Region

Telescope Size	CH_3Cl Abundance	λ_{in}	T_{in}	$\sigma_{T_{in}}$	λ_{out}	T_{out}	$\sigma_{T_{out}}$	SNR
100 m	100%	3.25 μm	0.3887	0.0130	3.65 μm	0.9367	0.0151	27.5
100 m	50%	3.25 μm	0.3772	0.0130	3.75 μm	0.9417	0.0153	28.1
100 m	20%	3.25 μm	0.3963	0.0130	3.75 μm	0.9196	0.0153	26.1
100 m	1%	3.25 μm	0.4783	0.0130	3.65 μm	0.9375	0.0151	23.0
100 m	1000 ppm	3.25 μm	0.5472	0.0130	3.75 μm	0.9345	0.0153	19.3
100 m	100 ppm	3.25 μm	0.6378	0.0130	3.85 μm	0.9336	0.0163	14.2
100 m	10 ppm	3.25 μm	0.6975	0.0130	3.85 μm	0.9622	0.0163	12.7
100 m	1 ppm	Indiscernible						
50 m	100%	3.25 μm	0.3439	0.0260	3.65 μm	0.9168	0.0302	14.4
50 m	50%	3.25 μm	0.3625	0.0260	3.75 μm	0.9243	0.0307	14.0
50 m	20%	3.25 μm	0.3994	0.0260	3.65 μm	0.9491	0.0302	13.8
50 m	1%	3.25 μm	0.4420	0.0260	3.55 μm	0.9044	0.0289	11.9
50 m	1000 ppm	3.25 μm	0.5498	0.0260	3.75 μm	0.9429	0.0307	9.8
50 m	100 ppm	3.25 μm	0.6542	0.0260	3.85 μm	0.9420	0.0326	6.9
50 m	10 ppm	Indiscernible						
35 m	100%	3.25 μm	0.3449	0.0372	3.75 μm	0.8898	0.0438	9.5
35 m	50%	3.25 μm	0.3806	0.0372	3.65 μm	0.9813	0.0431	10.6
35 m	20%	3.35 μm	0.4329	0.0386	3.75 μm	0.9236	0.0438	8.4
35 m	1%	3.25 μm	0.4714	0.0372	3.45 μm	0.9317	0.0400	8.4
35 m	1000 ppm	3.25 μm	0.5154	0.0372	3.65 μm	0.9950	0.0431	8.4
35 m	100 ppm	3.25 μm	0.6056	0.0372	3.85 μm	0.9350	0.0465	5.5
35 m	10 ppm	Indiscernible						
20 m	100%	3.25 μm	0.3012	0.0651	3.55 μm	0.9404	0.0722	6.6
20 m	50%	3.25 μm	0.2216	0.0651	3.65 μm	0.9833	0.0755	7.6
20 m	20%	3.25 μm	0.4236	0.0651	3.55 μm	0.9658	0.0722	5.6
20 m	1%	3.25 μm	0.4806	0.0651	3.55 μm	0.9768	0.0722	5.1
20 m	1000 ppm	3.25 μm	0.6982	0.0651	3.65 μm	1.0135	0.0755	3.2
20 m	100 ppm	3.25 μm	0.6236	0.0651	3.75 μm	1.0220	0.0767	4.0
20 m	10 ppm	Indiscernible						
100 m	100%	4.05 μm	0.3805	0.0172	5.35 μm	0.7961	0.0251	13.7
100 m	50%	4.05 μm	0.3965	0.0172	5.35 μm	0.7846	0.0251	12.8

Continued on next page

Table B.6 – *Continued from previous page*

Telescope Size	CH_3Cl Abundance	λ_{in}	T_{in}	$\sigma_{T_{in}}$	λ_{out}	T_{out}	$\sigma_{T_{out}}$	SNR
100 m	20%	4.15 μm	0.4142	0.0179	5.35 μm	0.7850	0.0251	12.0
100 m	1%	4.05 μm	0.5421	0.0172	4.45 μm	0.9034	0.0196	13.9
100 m	1000 ppm	4.05 μm	0.6404	0.0172	4.45 μm	0.9245	0.0196	10.9
100 m	100 ppm	4.05 μm	0.7803	0.0172	3.85 μm	0.9336	0.0163	6.5
100 m	10 ppm	Indiscernible						
50 m	100%	4.05 μm	0.3140	0.0345	5.35 μm	0.8257	0.0502	8.4
50 m	50%	4.05 μm	0.3500	0.0344	5.45 μm	0.8109	0.0511	7.5
50 m	20%	3.95 μm	0.4388	0.0331	5.15 μm	0.8608	0.0476	7.3
50 m	1%	4.25 μm	0.5342	0.0369	4.55 μm	0.8944	0.0403	6.6
50 m	1000 ppm	4.25 μm	0.6219	0.0369	3.75 μm	0.9429	0.0307	6.7
50 m	100 ppm	4.05 μm	0.7821	0.0344	3.85 μm	0.9420	0.0326	3.4
50 m	10 ppm	Indiscernible						
35 m	100%	4.25 μm	0.3038	0.0527	5.35 μm	0.8097	0.0717	5.7
35 m	50%	4.15 μm	0.3816	0.0511	5.35 μm	0.8169	0.0717	4.9
35 m	20%	4.15 μm	0.4417	0.0511	5.15 μm	0.8750	0.0680	5.1
35 m	1%	4.05 μm	0.4683	0.0492	4.55 μm	0.8947	0.0576	5.6
35 m	1000 ppm	4.05 μm	0.6160	0.0492	4.45 μm	0.9597	0.0560	4.6
35 m	100 ppm	4.05 μm	0.6629	0.0492	3.85 μm	0.9350	0.0465	4.0
35 m	10 ppm	Indiscernible						
20 m	100%	4.15 μm	0.3039	0.0894	5.15 μm	0.9173	0.1190	4.1
20 m	50%	4.15 μm	0.4266	0.0894	5.25 μm	1.0110	0.1215	3.9
20 m	20%	4.05 μm	0.3027	0.0861	5.05 μm	0.8803	0.1144	4.0
20 m	1%	4.25 μm	0.4353	0.0923	4.45 μm	0.9392	0.0981	3.7
20 m	1000 ppm	4.35 μm	0.6215	0.0953	4.45 μm	0.8809	0.0981	1.9
20 m	100 ppm	4.05 μm	0.7147	0.0861	4.35 μm	1.0073	0.0953	2.3
20 m	10 ppm	Indiscernible						
100 m	100%	4.85 μm	0.4622	0.0221	5.35 μm	0.7961	0.0251	10.0
100 m	50%	4.85 μm	0.5097	0.0221	5.35 μm	0.7846	0.0251	8.2
100 m	20%	4.85 μm	0.5168	0.0221	5.35 μm	0.7850	0.0251	8.0
100 m	1%	4.85 μm	0.6578	0.0221	5.15 μm	0.8261	0.0238	5.2
100 m	1000 ppm	4.85 μm	0.7163	0.0221	4.95 μm	0.8905	0.0227	5.5
100 m	100 ppm	4.85 μm	0.7474	0.0221	4.95 μm	0.8714	0.0227	3.9
100 m	10 ppm	Indiscernible						

Continued on next page

Table B.6 – *Continued from previous page*

Telescope Size	CH_3Cl Abundance	λ_{in}	T_{in}	$\sigma_{T_{in}}$	λ_{out}	T_{out}	$\sigma_{T_{out}}$	SNR
50 m	100%	4.85 μm	0.4146	0.0441	5.35 μm	0.8257	0.0502	6.2
50 m	50%	4.85 μm	0.4823	0.0441	5.45 μm	0.8109	0.0511	4.9
50 m	20%	4.85 μm	0.4253	0.0441	5.15 μm	0.8608	0.0476	6.7
50 m	1%	4.85 μm	0.6723	0.0441	5.25 μm	0.8510	0.0486	2.7
50 m	1000 ppm	4.85 μm	0.7550	0.0441	4.95 μm	0.9142	0.0454	2.5
50 m	100 ppm	4.85 μm	0.7305	0.0441	4.95 μm	0.8705	0.0454	2.2
50 m	10 ppm	Indiscernible						
35 m	100%	4.85 μm	0.3609	0.0630	5.35 μm	0.8097	0.0717	4.7
35 m	50%	4.85 μm	0.4996	0.0630	5.35 μm	0.8169	0.0717	3.3
35 m	20%	4.85 μm	0.4482	0.0630	5.15 μm	0.8750	0.0680	4.6
35 m	1%	4.85 μm	0.5795	0.0631	4.55 μm	0.8947	0.0576	3.7
35 m	1000 ppm	4.85 μm	0.7724	0.0630	4.95 μm	0.9532	0.0649	2.0
35 m	100 ppm	Indiscernible						
20 m	100%	4.95 μm	0.4173	0.1136	5.15 μm	0.9173	0.1190	3.0
20 m	50%	4.95 μm	0.4832	0.1136	5.25 μm	1.0110	0.1215	3.2
20 m	20%	4.75 μm	0.5146	0.1066	5.05 μm	0.8803	0.1144	2.3
20 m	1%	4.95 μm	0.6784	0.1136	4.45 μm	0.9392	0.0981	1.7
20 m	1000 ppm	4.85 μm	0.5915	0.1102	4.95 μm	0.8585	0.1136	1.7
20 m	100 ppm	Indiscernible						
100 m	100%	7.25 μm	0.2729	0.0269	5.25 μm	0.7884	0.0174	16.1
100 m	50%	7.25 μm	0.3343	0.0269	5.25 μm	0.8001	0.0174	14.5
100 m	20%	7.25 μm	0.3047	0.0269	5.25 μm	0.8036	0.0174	15.6
100 m	1%	7.25 μm	0.4339	0.0269	5.05 μm	0.8519	0.0163	13.3
100 m	1000 ppm	7.25 μm	0.5152	0.0269	4.65 μm	0.9548	0.0146	14.4
100 m	100 ppm	7.45 μm	0.6301	0.0282	4.45 μm	0.9632	0.0140	10.6
100 m	10 ppm	Indiscernible						
50 m	100%	7.45 μm	0.2274	0.0564	5.25 μm	0.7707	0.0349	8.2
50 m	50%	7.45 μm	0.3052	0.0564	5.25 μm	0.8197	0.0349	7.8
50 m	20%	7.25 μm	0.3348	0.0538	5.25 μm	0.8204	0.0349	7.6
50 m	1%	7.45 μm	0.3851	0.0564	4.65 μm	0.8860	0.0293	7.9
50 m	1000 ppm	7.25 μm	0.4578	0.0538	4.65 μm	0.9244	0.0293	7.6
50 m	100 ppm	7.45 μm	0.5790	0.0564	4.65 μm	0.9340	0.0293	5.6
50 m	10 ppm	Indiscernible						

Continued on next page

Table B.6 – *Continued from previous page*

Telescope Size	CH_3Cl Abundance	λ_{in}	T_{in}	$\sigma_{T_{in}}$	λ_{out}	T_{out}	$\sigma_{T_{out}}$	SNR
35 m	100%	7.45 μm	0.2541	0.0805	5.45 μm	0.7837	0.0526	5.5
35 m	50%	7.25 μm	0.2374	0.0768	5.05 μm	0.7775	0.0467	6.0
35 m	20%	7.25 μm	0.3012	0.0768	5.25 μm	0.7579	0.0498	5.0
35 m	1%	7.25 μm	0.4151	0.0798	5.25 μm	0.8128	0.0498	4.2
35 m	1000 ppm	7.45 μm	0.4271	0.0806	5.05 μm	0.8475	0.0466	4.5
35 m	100 ppm	7.45 μm	0.6444	0.0806	4.45 μm	0.9153	0.0400	3.0
35 m	10 ppm	Indiscernible						
20 m	100%	7.25 μm	0.1123	0.1344	5.25 μm	0.8289	0.0871	4.5
20 m	50%	7.25 μm	0.1653	0.1344	5.85 μm	0.7457	0.1009	3.5
20 m	20%	7.45 μm	0.3042	0.1410	5.05 μm	0.7732	0.0816	2.9
20 m	1%	7.25 μm	0.3271	0.1344	5.45 μm	0.9368	0.0921	3.7
20 m	1000 ppm	7.45 μm	0.4556	0.1409	4.45 μm	0.9565	0.0700	3.2
20 m	100 ppm	7.45 μm	0.5371	0.1410	4.45 μm	0.9962	0.0700	2.9
20 m	10 ppm	Indiscernible						

B.7 Hydrogen Sulfide

Table B.7: Hydrogen Sulfide Detectability in the IR Wavelength Region

Telescope Size	H_2S Abundance	λ_{in}	T_{in}	$\sigma_{T_{in}}$	λ_{out}	T_{out}	$\sigma_{T_{out}}$	SNR
100 m	100%	3.65 μm	0.5414	0.0151	4.65 μm	0.8757	0.0207	13.0
100 m	50%	3.65 μm	0.5896	0.0151	4.75 μm	0.9065	0.0213	12.1
100 m	20%	3.65 μm	0.6080	0.0151	4.75 μm	0.9316	0.0213	12.4
100 m	1%	3.65 μm	0.7118	0.0151	4.55 μm	0.9405	0.0202	9.1
100 m	1000 ppm	3.75 μm	0.7590	0.0153	3.45 μm	0.9236	0.0140	7.9
100 m	100 ppm	Indiscernible						
50 m	100%	3.65 μm	0.5568	0.0302	4.55 μm	0.9221	0.0403	7.3
50 m	50%	3.75 μm	0.5575	0.0307	4.75 μm	0.9744	0.0426	7.9
50 m	20%	3.65 μm	0.6093	0.0302	4.65 μm	0.9282	0.0414	6.2
50 m	1%	3.75 μm	0.6970	0.0307	4.55 μm	0.9325	0.0403	4.6
50 m	1000 ppm	3.65 μm	0.8205	0.0302	3.45 μm	0.9808	0.0280	3.9
50 m	100 ppm	Indiscernible						
35 m	100%	4.15 μm	0.5204	0.0510	4.85 μm	0.8978	0.0629	4.7
35 m	50%	3.85 μm	0.5693	0.0465	4.85 μm	0.9314	0.0630	4.6
35 m	20%	3.75 μm	0.5364	0.0438	4.55 μm	0.8926	0.0576	4.9
35 m	1%	3.75 μm	0.6719	0.0439	4.55 μm	0.9472	0.0576	3.8
35 m	1000 ppm	3.65 μm	0.8405	0.0431	4.55 μm	1.0031	0.0576	2.3
35 m	100 ppm	Indiscernible						
20 m	100%	3.85 μm	0.4892	0.0814	2.15 μm	0.9314	0.0387	4.9
20 m	50%	3.75 μm	0.5465	0.0767	4.75 μm	0.9276	0.1065	2.9
20 m	20%	3.75 μm	0.5522	0.0767	3.45 μm	0.9274	0.0701	3.6
20 m	1%	3.65 μm	0.6575	0.0754	3.34 μm	0.9690	0.0677	3.1
20 m	1000 ppm	Indiscernible						

B.8 Carbonyl Sulfide

Table B.8: Carbonyl Sulfide Detectability in the IR Wavelength Region

Telescope Size	OCS Abundance	λ_{in}	T_{in}	$\sigma_{T_{in}}$	λ_{out}	T_{out}	$\sigma_{T_{out}}$	SNR
100 m	100%	3.45 μm	0.4503	0.0140	4.05 μm	0.9822	0.0172	24.0
100 m	50%	3.45 μm	0.4402	0.0140	4.15 μm	0.9913	0.0178	24.3
100 m	20%	3.45 μm	0.4657	0.0140	4.15 μm	0.9825	0.0178	22.8
100 m	1%	3.45 μm	0.5369	0.0140	4.05 μm	0.9757	0.0172	19.8
100 m	1000 ppm	3.45 μm	0.6402	0.0140	4.05 μm	1.0048	0.0172	16.4
100 m	100 ppm	3.45 μm	0.7023	0.0140	4.25 μm	0.9806	0.0185	12.0
100 m	10 ppm	Indiscernible						
50 m	100%	3.45 μm	0.4728	0.0280	4.05 μm	0.9895	0.0344	11.6
50 m	50%	3.45 μm	0.4659	0.0280	4.05 μm	0.9647	0.0344	11.2
50 m	20%	3.45 μm	0.4542	0.0280	4.05 μm	1.0287	0.0344	13.0
50 m	1%	3.45 μm	0.5593	0.0280	4.05 μm	1.0223	0.0344	10.4
50 m	1000 ppm	3.45 μm	0.5806	0.0280	4.25 μm	0.9971	0.0369	9.0
50 m	100 ppm	3.45 μm	0.6971	0.0280	4.15 μm	1.0000	0.0355	6.7
50 m	10 ppm	Indiscernible						
35 m	100%	3.45 μm	0.4070	0.0400	3.75 μm	1.0057	0.0439	10.1
35 m	50%	3.45 μm	0.4210	0.0400	4.05 μm	0.9998	0.0492	9.1
35 m	20%	3.45 μm	0.4237	0.0400	4.25 μm	0.9724	0.0527	8.3
35 m	1%	3.45 μm	0.5158	0.0400	4.05 μm	0.9868	0.0492	7.4
35 m	1000 ppm	3.45 μm	0.6133	0.0400	4.05 μm	0.9793	0.0492	5.8
35 m	100 ppm	3.45 μm	0.6635	0.0400	3.75 μm	0.9845	0.0439	5.4
35 m	10 ppm	Indiscernible						
20 m	100%	3.45 μm	0.4360	0.0700	3.75 μm	0.9902	0.0767	5.3
20 m	50%	3.45 μm	0.5584	0.0700	4.05 μm	0.9723	0.0861	3.7
20 m	20%	3.45 μm	0.5734	0.0700	3.75 μm	0.9633	0.0768	3.8
20 m	1%	3.45 μm	0.5770	0.0700	3.75 μm	1.0223	0.0767	4.3
20 m	1000 ppm	3.45 μm	0.6077	0.0700	3.95 μm	1.0102	0.0827	3.7
20 m	100 ppm	3.45 μm	0.6474	0.0700	3.75 μm	0.9800	0.0767	3.2
20 m	10 ppm	Indiscernible						
100 m	100%	4.85 μm	0.3612	0.0220	5.15 μm	0.7730	0.0238	12.7
100 m	50%	4.85 μm	0.3428	0.0220	5.15 μm	0.7724	0.0238	13.3
100 m	20%	4.85 μm	0.3314	0.0220	5.15 μm	0.7842	0.0238	14.0

Continued on next page

Table B.8 – *Continued from previous page*

Telescope Size	OCS Abundance	λ_{in}	T_{in}	$\sigma_{T_{in}}$	λ_{out}	T_{out}	$\sigma_{T_{out}}$	SNR
100 m	1%	4.85 μm	0.3694	0.0220	5.15 μm	0.7901	0.0238	13.0
100 m	1000 ppm	4.85 μm	0.4858	0.0220	5.15 μm	0.7659	0.0238	8.6
100 m	100 ppm	4.85 μm	0.5127	0.0221	5.15 μm	0.8054	0.0238	9.0
100 m	10 ppm	4.85 μm	0.5747	0.0221	5.15 μm	0.8314	0.0238	7.9
100 m	1 ppm	4.85 μm	0.6477	0.0221	5.05 μm	0.8394	0.0228	6.0
100 m	100 ppb	4.85 μm	0.7255	0.0221	5.15 μm	0.8344	0.0238	3.4
100 m	10 ppb	4.85 μm	0.7492	0.0221	4.95 μm	0.8672	0.0227	3.7
100 m	1 ppb	Indiscernible						
50 m	100%	4.85 μm	0.2770	0.0441	5.15 μm	0.7720	0.0476	7.6
50 m	50%	4.95 μm	0.2836	0.0455	5.15 μm	0.7961	0.0476	7.8
50 m	20%	4.85 μm	0.3240	0.0441	5.15 μm	0.8204	0.0477	7.6
50 m	1%	4.95 μm	0.4500	0.0455	5.15 μm	0.7942	0.0477	5.2
50 m	1000 ppm	4.85 μm	0.4356	0.0441	5.15 μm	0.8131	0.0477	5.8
50 m	100 ppm	4.85 μm	0.5381	0.0441	5.15 μm	0.7802	0.0476	3.7
50 m	10 ppm	4.85 μm	0.5881	0.0441	5.15 μm	0.8197	0.0476	3.6
50 m	1 ppm	4.85 μm	0.6683	0.0441	4.95 μm	0.7975	0.0455	2.0
50 m	100 ppb	4.85 μm	0.6390	0.0441	5.05 μm	0.8745	0.0456	3.7
50 m	10 ppb	Indiscernible						
35 m	100%	4.85 μm	0.3452	0.0630	5.65 μm	0.7639	0.0769	4.2
35 m	50%	4.85 μm	0.3458	0.0630	5.15 μm	0.7496	0.0681	4.4
35 m	20%	4.85 μm	0.1956	0.0630	5.15 μm	0.8197	0.0681	6.7
35 m	1%	4.85 μm	0.3270	0.0630	5.15 μm	0.8360	0.0681	5.5
35 m	1000 ppm	4.95 μm	0.4102	0.0650	5.15 μm	0.7960	0.0681	4.1
35 m	100 ppm	4.85 μm	0.4699	0.0630	5.15 μm	0.9186	0.0680	4.8
35 m	10 ppm	4.85 μm	0.4378	0.0630	5.05 μm	0.8224	0.0652	4.2
35 m	1 ppm	4.85 μm	0.6146	0.0630	5.05 μm	0.8469	0.0652	2.6
35 m	100 ppb	4.85 μm	0.6982	0.0630	5.05 μm	0.8698	0.0652	1.9
35 m	10 ppb	Indiscernible						
20 m	100%	4.85 μm	0.1975	0.1102	5.55 μm	0.9952	0.1322	4.6
20 m	50%	4.95 μm	0.3128	0.1137	5.45 μm	0.8483	0.1276	3.1
20 m	20%	4.95 μm	0.3907	0.1137	5.15 μm	0.8842	0.1191	3.0
20 m	1%	4.85 μm	0.1641	0.1102	5.45 μm	0.8016	0.1275	3.8
20 m	1000 ppm	4.85 μm	0.2697	0.1102	5.15 μm	0.8113	0.1191	3.3

Continued on next page

Table B.8 – *Continued from previous page*

Telescope Size	OCS Abundance	λ_{in}	T_{in}	$\sigma_{T_{in}}$	λ_{out}	T_{out}	$\sigma_{T_{out}}$	SNR
20 m	100 ppm	4.85 μm	0.5512	0.1103	5.05 μm	0.9366	0.1140	2.4
20 m	10 ppm	Indiscernible						
100 m	100%	5.35 μm	0.4348	0.0252	5.65 μm	0.7321	0.0269	8.1
100 m	50%	5.35 μm	0.4331	0.0252	5.55 μm	0.7009	0.0264	7.3
100 m	20%	5.25 μm	0.4457	0.0244	5.65 μm	0.7427	0.0269	8.2
100 m	1%	5.25 μm	0.5283	0.0244	5.55 μm	0.7300	0.0264	5.6
100 m	1000 ppm	5.25 μm	0.5443	0.0244	5.15 μm	0.7659	0.0238	6.5
100 m	100 ppm	Indiscernible						
50 m	100%	5.35 μm	0.4099	0.0503	6.15 μm	0.7509	0.0606	4.3
50 m	50%	5.35 μm	0.4647	0.0503	6.15 μm	0.7186	0.0606	3.2
50 m	20%	5.35 μm	0.4539	0.0503	5.15 μm	0.8204	0.0477	5.3
50 m	1%	5.35 μm	0.5706	0.0503	5.45 μm	0.7295	0.0510	2.2
50 m	1000 ppm	5.25 μm	0.5699	0.0488	5.55 μm	0.7648	0.0529	2.7
50 m	100 ppm	Indiscernible						
35 m	100%	5.25 μm	0.4342	0.0697	5.65 μm	0.7639	0.0769	3.2
35 m	50%	5.25 μm	0.5085	0.0697	5.15 μm	0.7496	0.0681	2.5
35 m	20%	5.35 μm	0.4044	0.0719	5.45 μm	0.7222	0.0729	3.1
35 m	1%	5.25 μm	0.5107	0.0697	5.45 μm	0.7784	0.0729	2.7
35 m	1000 ppm	Indiscernible						
20 m	100%	5.25 μm	0.4810	0.1219	5.55 μm	0.9952	0.1322	2.9
20 m	50%	5.25 μm	0.5050	0.1219	5.45 μm	0.8483	0.1276	1.9
20 m	20%	5.35 μm	0.4435	0.1258	5.45 μm	0.8105	0.1275	2.0
20 m	1%	5.25 μm	0.3621	0.1219	5.45 μm	0.8016	0.1275	2.5
20 m	1000 ppm	Indiscernible						
100 m	100%	5.95 μm	0.4426	0.0285	5.65 μm	0.7321	0.0269	7.4
100 m	50%	5.85 μm	0.4660	0.0281	5.55 μm	0.7009	0.0264	6.1
100 m	20%	5.85 μm	0.4945	0.0281	5.65 μm	0.7427	0.0269	6.4
100 m	1%	5.95 μm	0.5355	0.0285	6.05 μm	0.7197	0.0299	4.5
100 m	1000 ppm	5.85 μm	0.6145	0.0281	5.65 μm	0.7653	0.0269	3.9
100 m	100 ppm	Indiscernible						
50 m	100%	5.85 μm	0.3987	0.0562	6.15 μm	0.7509	0.0606	4.3
50 m	50%	5.85 μm	0.4469	0.0562	6.15 μm	0.7186	0.0606	3.3
50 m	20%	5.95 μm	0.4908	0.0571	6.15 μm	0.7018	0.0606	2.5

Continued on next page

Table B.8 – *Continued from previous page*

Telescope Size	OCS Abundance	λ_{in}	T_{in}	$\sigma_{T_{in}}$	λ_{out}	T_{out}	$\sigma_{T_{out}}$	SNR
50 m	1%	5.95 μm	0.5374	0.0571	6.15 μm	0.7062	0.0606	2.0
50 m	1000 ppm	5.95 μm	0.5626	0.0571	6.05 μm	0.7064	0.0599	1.7
50 m	100 ppm	Indiscernible						
35 m	100%	5.95 μm	0.4385	0.0815	5.65 μm	0.7639	0.0769	2.9
35 m	50%	5.95 μm	0.2308	0.0815	5.15 μm	0.7496	0.0681	4.9
35 m	20%	5.95 μm	0.5246	0.0815	5.65 μm	0.7500	0.0769	2.0
35 m	1%	5.95 μm	0.5016	0.0815	6.05 μm	0.8142	0.0855	2.6
35 m	1000 ppm	Indiscernible						
20 m	100%	5.95 μm	0.4496	0.1426	5.55 μm	0.9952	0.1322	2.8
20 m	50%	6.05 μm	0.4961	0.1497	5.45 μm	0.8483	0.1276	1.8
20 m	20%	5.85 μm	0.2322	0.1405	5.75 μm	0.7026	0.1376	2.4
20 m	1%	5.85 μm	0.4912	0.1404	6.15 μm	0.8136	0.1516	1.6
20 m	1000 ppm	Indiscernible						

B.9 Phosphine

Table B.9: Phosphine Detectability in the IR Wavelength Region

Telescope Size	PH_3 Abundance	λ_{in}	T_{in}	$\sigma_{T_{in}}$	λ_{out}	T_{out}	$\sigma_{T_{out}}$	SNR
100 m	100%	2.85 μm	0.4744	0.0108	3.95 μm	0.9815	0.0165	25.7
100 m	50%	2.95 μm	0.4929	0.0115	3.85 μm	0.9764	0.0163	24.2
100 m	20%	2.95 μm	0.5227	0.0115	3.95 μm	0.9779	0.0165	22.6
100 m	1%	2.95 μm	0.5983	0.0115	3.85 μm	0.9733	0.0162	18.9
100 m	1000 ppm	Indiscernible						
50 m	100%	2.85 μm	0.4932	0.0217	3.85 μm	0.9747	0.0325	12.3
50 m	50%	2.95 μm	0.4364	0.0230	3.95 μm	0.9849	0.0331	13.6
50 m	20%	2.85 μm	0.5007	0.0217	3.75 μm	0.9623	0.0307	12.3
50 m	1%	2.85 μm	0.5823	0.0217	3.75 μm	0.9634	0.0307	10.1
50 m	1000 ppm	Indiscernible						
35 m	100%	2.85 μm	0.4732	0.0310	3.85 μm	0.9725	0.0464	8.9
35 m	50%	2.95 μm	0.4477	0.0328	3.85 μm	0.9678	0.0464	9.2
35 m	20%	2.95 μm	0.5385	0.0328	3.85 μm	0.9422	0.0464	7.1
35 m	1%	2.95 μm	0.6313	0.0328	3.75 μm	0.9509	0.0439	5.8
35 m	1000 ppm	Indiscernible						
20 m	100%	2.95 μm	0.4277	0.0575	3.95 μm	0.9889	0.0827	5.6
20 m	50%	2.95 μm	0.4494	0.0575	3.95 μm	0.9926	0.0827	5.4
20 m	20%	2.95 μm	0.4729	0.0575	3.75 μm	0.9983	0.0768	5.5
20 m	1%	Indiscernible						
100 m	100%	4.55 μm	0.4417	0.0202	5.25 μm	0.7988	0.0244	11.3
100 m	50%	4.55 μm	0.4447	0.0202	5.35 μm	0.8008	0.0251	11.1
100 m	20%	4.55 μm	0.4731	0.0210	5.15 μm	0.7620	0.0238	9.1
100 m	1%	4.45 μm	0.5366	0.0197	5.35 μm	0.7959	0.0252	8.1
100 m	1000 ppm	4.15 μm	0.5631	0.0178	5.15 μm	0.8155	0.0238	8.5
100 m	100 ppm	4.15 μm	0.6440	0.0178	4.75 μm	0.8242	0.0213	6.5
100 m	10 ppm	4.45 μm	0.7164	0.0197	4.65 μm	0.8630	0.0207	5.1
100 m	1 ppm	4.15 μm	0.8182	0.0178	4.75 μm	0.9037	0.0213	3.1
100 m	100 ppb	Indiscernible						
50 m	100%	4.45 μm	0.4686	0.0393	5.15 μm	0.7942	0.0476	5.3
50 m	50%	4.45 μm	0.4372	0.0393	5.35 μm	0.8793	0.0503	6.9
50 m	20%	4.45 μm	0.4731	0.0393	5.35 μm	0.7784	0.0503	4.8

Continued on next page

Table B.9 – *Continued from previous page*

Telescope Size	PH_3 Abundance	λ_{in}	T_{in}	$\sigma_{T_{in}}$	λ_{out}	T_{out}	$\sigma_{T_{out}}$	SNR
50 m	1%	4.55 μm	0.5161	0.0403	5.15 μm	0.8049	0.0476	4.6
50 m	1000 ppm	4.45 μm	0.5735	0.0393	4.85 μm	0.8055	0.0440	3.9
50 m	100 ppm	4.35 μm	0.6147	0.0381	4.75 μm	0.8250	0.0426	3.7
50 m	10 ppm	4.25 μm	0.7075	0.0370	4.75 μm	0.9386	0.0426	4.1
50 m	1 ppm	4.35 μm	0.7804	0.0381	4.75 μm	0.9469	0.0426	2.9
50 m	100 ppb	Indiscernible						
35 m	100%	4.55 μm	0.4273	0.0576	5.25 μm	0.8016	0.0696	4.1
35 m	50%	4.45 μm	0.3996	0.0562	5.45 μm	0.8249	0.0729	4.6
35 m	20%	4.55 μm	0.4679	0.0576	5.25 μm	0.8162	0.0696	3.9
35 m	1%	4.55 μm	0.4388	0.0576	5.25 μm	0.7731	0.0696	3.7
35 m	1000 ppm	4.45 μm	0.5685	0.0562	4.85 μm	0.8274	0.0629	3.1
35 m	100 ppm	4.15 μm	0.5879	0.0507	4.75 μm	0.8822	0.0609	3.7
35 m	10 ppm	4.15 μm	0.7728	0.0507	4.65 μm	0.9471	0.0590	2.2
35 m	1 ppm	4.15 μm	0.8040	0.0507	4.55 μm	0.9819	0.0576	2.3
35 m	100 ppb	Indiscernible						
20 m	100%	4.55 μm	0.2624	0.1008	5.45 μm	0.8262	0.1276	3.5
20 m	50%	4.55 μm	0.3693	0.1008	5.45 μm	0.7594	0.1276	2.4
20 m	20%	4.55 μm	0.4120	0.1008	5.45 μm	0.7903	0.1276	2.3
20 m	1%	4.55 μm	0.5491	0.1007	5.45 μm	0.7303	0.1275	1.1
20 m	1000 ppm	4.45 μm	0.5143	0.0983	4.75 μm	0.9373	0.1066	2.9
20 m	100 ppm	4.35 μm	0.5876	0.0953	4.75 μm	0.9729	0.1065	2.7
20 m	10 ppm	4.35 μm	0.5416	0.0953	4.55 μm	0.8703	0.1007	2.4
20 m	1 ppm	Indiscernible						

B.10 Sulfur Dioxide

Table B.10: Sulfur Dioxide Detectability in the IR Wavelength Region

Telescope Size	SO_2 Abundance	λ_{in}	T_{in}	$\sigma_{T_{in}}$	λ_{out}	T_{out}	$\sigma_{T_{out}}$	SNR
100 m	100%	3.65 μm	0.5333	0.0151	4.25 μm	0.9911	0.0185	19.2
100 m	50%	3.65 μm	0.5465	0.0151	4.15 μm	0.9711	0.0178	18.2
100 m	20%	3.65 μm	0.6179	0.0151	4.25 μm	1.0020	0.0185	16.1
100 m	1%	3.65 μm	0.7179	0.0151	4.15 μm	0.9819	0.0178	11.3
100 m	1000 ppm	3.65 μm	0.7705	0.0151	3.85 μm	0.9643	0.0163	8.7
100 m	100 ppm	Indiscernible						
50 m	100%	3.75 μm	0.5530	0.0307	4.25 μm	0.9697	0.0370	8.7
50 m	50%	3.65 μm	0.5018	0.0301	4.15 μm	0.9631	0.0355	9.9
50 m	20%	3.65 μm	0.5706	0.0301	3.85 μm	0.9816	0.0325	9.3
50 m	1%	3.65 μm	0.7098	0.0301	4.15 μm	0.9626	0.0355	5.4
50 m	1000 ppm	3.65 μm	0.7554	0.0301	4.15 μm	0.9793	0.0355	4.8
50 m	100 ppm	Indiscernible						
35 m	100%	3.75 μm	0.5172	0.0439	2.15 μm	0.9649	0.0221	9.1
35 m	50%	3.75 μm	0.5005	0.0439	4.45 μm	0.9972	0.0562	7.0
35 m	20%	3.65 μm	0.5099	0.0430	4.25 μm	0.9927	0.0528	7.1
35 m	1%	3.65 μm	0.6843	0.0430	3.45 μm	1.0045	0.0400	5.5
35 m	1000 ppm	3.65 μm	0.7780	0.0430	4.15 μm	0.9251	0.0508	2.2
35 m	100 ppm	Indiscernible						
20 m	100%	3.65 μm	0.5425	0.0753	3.45 μm	1.0091	0.0700	4.5
20 m	50%	3.75 μm	0.5640	0.0768	2.15 μm	0.9437	0.0387	4.4
20 m	20%	3.75 μm	0.5993	0.0768	4.15 μm	0.9873	0.0888	3.3
20 m	1%	3.65 μm	0.6938	0.0753	3.35 μm	0.9583	0.0676	2.6
20 m	1000 ppm	Indiscernible						
100 m	100%	4.05 μm	0.3329	0.0172	4.25 μm	0.9911	0.0185	26.1
100 m	50%	4.05 μm	0.3253	0.0172	4.15 μm	0.9711	0.0178	26.1
100 m	20%	4.05 μm	0.3981	0.0172	4.25 μm	1.0020	0.0185	23.9
100 m	1%	4.05 μm	0.4857	0.0172	4.15 μm	0.9819	0.0178	20.0
100 m	1000 ppm	4.05 μm	0.5989	0.0172	3.85 μm	0.9643	0.0163	15.4
100 m	100 ppm	4.05 μm	0.7115	0.0172	4.15 μm	0.9955	0.0178	11.5
100 m	10 ppm	4.05 μm	0.8331	0.0172	4.15 μm	0.9890	0.0178	6.3

Continued on next page

Table B.10 – *Continued from previous page*

Telescope Size	SO_2 Abundance	λ_{in}	T_{in}	$\sigma_{T_{in}}$	λ_{out}	T_{out}	$\sigma_{T_{out}}$	SNR
100 m	1 ppm	Indiscernible						
50 m	100%	4.05 μm	0.3907	0.0344	4.25 μm	0.9697	0.0370	11.5
50 m	50%	4.05 μm	0.3280	0.0344	4.15 μm	0.9631	0.0355	12.8
50 m	20%	4.05 μm	0.3934	0.0344	3.85 μm	0.9816	0.0325	12.4
50 m	1%	4.05 μm	0.5428	0.0344	4.15 μm	0.9626	0.0355	8.5
50 m	1000 ppm	4.05 μm	0.5795	0.0344	4.15 μm	0.9793	0.0355	8.1
50 m	100 ppm	4.05 μm	0.6582	0.0344	3.85 μm	1.0054	0.0325	7.3
50 m	10 ppm	4.05 μm	0.8188	0.0344	3.85 μm	1.0123	0.0325	4.1
50 m	1 ppm	Indiscernible						
35 m	100%	4.05 μm	0.3113	0.0492	2.15 μm	0.9649	0.0221	12.1
35 m	50%	4.05 μm	0.4110	0.0492	4.45 μm	0.9972	0.0562	7.8
35 m	20%	4.05 μm	0.2999	0.0492	4.25 μm	0.9927	0.0528	9.6
35 m	1%	4.05 μm	0.3720	0.0492	3.45 μm	1.0045	0.0400	10.0
35 m	1000 ppm	4.05 μm	0.5817	0.0492	4.15 μm	0.9251	0.0508	4.9
35 m	100 ppm	4.05 μm	0.6601	0.0492	4.15 μm	1.0030	0.0507	4.9
35 m	10 ppm	4.05 μm	0.8020	0.0492	3.85 μm	1.0015	0.0465	2.9
35 m	1 ppm	Indiscernible						
20 m	100%	4.05 μm	0.3880	0.0861	3.45 μm	1.0091	0.0700	5.6
20 m	50%	4.05 μm	0.4470	0.0861	2.15 μm	0.9437	0.0387	5.3
20 m	20%	4.05 μm	0.4990	0.0861	4.15 μm	0.9873	0.0888	3.9
20 m	1%	4.05 μm	0.4121	0.0861	3.35 μm	0.9583	0.0676	5.0
20 m	1000 ppm	4.05 μm	0.5663	0.0860	4.55 μm	0.9329	0.1008	2.8
20 m	100 ppm	4.05 μm	0.6690	0.0861	3.45 μm	0.9752	0.0700	2.8
20 m	10 ppm	Indiscernible						
100 m	100%	7.45 μm	0.2199	0.0280	7.05 μm	0.6714	0.0260	11.8
100 m	50%	7.45 μm	0.1969	0.0280	7.05 μm	0.6909	0.0260	12.9
100 m	20%	7.45 μm	0.2497	0.0280	7.05 μm	0.6778	0.0260	11.2
100 m	1%	7.45 μm	0.3052	0.0280	6.85 μm	0.6248	0.0252	8.5
100 m	1000 ppm	7.45 μm	0.3981	0.0280	7.05 μm	0.6852	0.0260	7.5
100 m	100 ppm	7.45 μm	0.5133	0.0280	7.05 μm	0.7011	0.0260	4.9
100 m	10 ppm	7.45 μm	0.5832	0.0280	7.05 μm	0.7529	0.0260	4.4
100 m	1 ppm	Indiscernible						
50 m	100%	7.45 μm	0.3215	0.0560	7.05 μm	0.6278	0.0521	4.0

Continued on next page

Table B.10 – *Continued from previous page*

Telescope Size	SO_2 Abundance	λ_{in}	T_{in}	$\sigma_{T_{in}}$	λ_{out}	T_{out}	$\sigma_{T_{out}}$	SNR
50 m	50%	7.45 μm	0.2305	0.0560	7.05 μm	0.6518	0.0521	5.5
50 m	20%	7.25 μm	0.2668	0.0533	7.85 μm	0.6879	0.0612	5.2
50 m	1%	7.45 μm	0.2217	0.0560	7.05 μm	0.7016	0.0521	6.3
50 m	1000 ppm	7.45 μm	0.3920	0.0560	6.85 μm	0.6064	0.0503	2.8
50 m	100 ppm	7.45 μm	0.3970	0.0560	6.65 μm	0.6359	0.0479	3.2
50 m	10 ppm	7.45 μm	0.5186	0.0560	7.65 μm	0.7764	0.0584	3.2
50 m	1 ppm	Indiscernible						
35 m	100%	7.45 μm	0.1991	0.0800	7.85 μm	0.7206	0.0874	4.4
35 m	50%	7.45 μm	0.1766	0.0800	7.05 μm	0.7154	0.0744	4.9
35 m	20%	7.45 μm	0.1620	0.0800	7.85 μm	0.6095	0.0875	3.8
35 m	1%	7.25 μm	0.3522	0.0762	7.05 μm	0.6589	0.0744	2.9
35 m	1000 ppm	7.45 μm	0.2736	0.0800	7.05 μm	0.7059	0.0744	4.0
35 m	100 ppm	Indiscernible						
20 m	100%	7.25 μm	0.2903	0.1334	7.85 μm	0.7560	0.1530	2.3
20 m	50%	7.25 μm	0.2254	0.1334	7.65 μm	0.5711	0.1464	1.7
20 m	20%	7.65 μm	0.2747	0.1463	8.05 μm	0.6751	0.1594	1.9
20 m	1%	7.25 μm	0.3120	0.1334	7.65 μm	0.7779	0.1462	2.4
20 m	1000 ppm	7.45 μm	0.4029	0.1400	7.05 μm	0.7578	0.1302	1.9
20 m	100 ppm	Indiscernible						
100 m	100%	8.85 μm	0.3094	0.0361	7.05 μm	0.6714	0.0260	8.1
100 m	50%	8.45 μm	0.2067	0.0340	7.85 μm	0.7296	0.0306	11.4
100 m	20%	8.85 μm	0.2904	0.0361	7.05 μm	0.6778	0.0260	8.7
100 m	1%	8.65 μm	0.3186	0.0349	6.85 μm	0.6248	0.0252	7.1
100 m	1000 ppm	8.65 μm	0.4145	0.0349	8.05 μm	0.7224	0.0319	6.5
100 m	100 ppm	8.65 μm	0.5511	0.0349	8.05 μm	0.8555	0.0319	6.4
100 m	10 ppm	8.65 μm	0.6669	0.0349	9.25 μm	0.8624	0.0381	3.8
100 m	1 ppm	Indiscernible						
50 m	100%	8.65 μm	0.2652	0.0698	7.05 μm	0.6278	0.0521	4.2
50 m	50%	8.65 μm	0.2727	0.0698	7.05 μm	0.6518	0.0521	4.4
50 m	20%	9.05 μm	0.2456	0.0741	7.85 μm	0.6879	0.0612	4.6
50 m	1%	8.45 μm	0.2827	0.0680	7.05 μm	0.7016	0.0521	4.9
50 m	1000 ppm	8.85 μm	0.4465	0.0721	9.45 μm	0.7714	0.0792	3.0
50 m	100 ppm	8.45 μm	0.4029	0.0680	8.25 μm	0.7450	0.0647	3.6

Continued on next page

Table B.10 – *Continued from previous page*

Telescope Size	SO_2 Abundance	λ_{in}	T_{in}	$\sigma_{T_{in}}$	λ_{out}	T_{out}	$\sigma_{T_{out}}$	SNR
50 m	10 ppm	8.45 μm	0.6180	0.0680	7.85 μm	0.7843	0.0612	1.8
50 m	1 ppm	Indiscernible						
35 m	100%	8.65 μm	0.2547	0.0998	7.85 μm	0.7206	0.0874	3.5
35 m	50%	8.85 μm	0.1027	0.1030	7.05 μm	0.7154	0.0744	4.8
35 m	20%	8.85 μm	0.2899	0.1031	7.85 μm	0.6095	0.0875	2.4
35 m	1%	9.05 μm	0.2092	0.1059	7.05 μm	0.6589	0.0744	3.5
35 m	1000 ppm	9.25 μm	0.5131	0.1088	9.65 μm	0.8306	0.1172	2.0
35 m	100 ppm	8.85 μm	0.4104	0.1031	8.05 μm	0.6963	0.0910	2.1
35 m	10 ppm	8.65 μm	0.5349	0.0998	8.45 μm	0.8313	0.0972	2.1
35 m	1 ppm	Indiscernible						
20 m	100%	9.05 μm	0.2052	0.1854	7.85 μm	0.7560	0.1530	2.3
20 m	50%	9.05 μm	0.1795	0.1854	7.85 μm	0.5931	0.1529	1.7
20 m	20%	9.05 μm	0.2385	0.1854	8.05 μm	0.6751	0.1594	1.8
20 m	1%	8.85 μm	0.2432	0.1804	7.65 μm	0.7779	0.1462	2.3
20 m	1000 ppm	9.05 μm	0.2212	0.1853	9.45 μm	0.7582	0.1980	2.0
20 m	100 ppm	Indiscernible						

Bibliography

Ballester, G. E., D. K. Sing, and F. Herbert, 2007: The signature of hot hydrogen in the atmosphere of the extrasolar planet HD 209458b. *Nature*, **445**, 511–514.

Borucki, W. J., et al., 2010: Kepler Planet-Detection Mission: Introduction and First Results. *Science*, **327**, 977–980.

Brasseur, G. P. and S. Solomon, 2005: *Aeromony of the Middle Atmosphere*. 3d ed., Springer, The Netherlands, 644 pp.

Carpenter, E. J., S. Lin, and D. G. Capone, 2000: Bacterial Activity in South Pole Snow. *Applied and Environmental Microbiology*, **66**, 4514–4517.

Charbonneau, D., T. M. Brown, R. W. Noyes, and R. L. Gilliland, 2002: Detection of an Extrasolar Planet Atmosphere. *ApJ*, **568**, 377–384.

Chu, P. M., F. R. Guenther, G. C. Rhoderick, and W. J. Lafferty, 1999: The NIST Quantitative Infrared Database. *Journal of Research of the National Institute of Standards and Technology*, **104**, 59–81.

Cochran, W. D., et al., 2011: Kepler-18b, c, and d: A System of Three Planets Confirmed by Transit Timing Variations, Light Curve Validation, Warm-Spitzer Photometry, and Radial Velocity Measurements. *ApJS*, **197**, 7.

Des Marais, D. J., 1998: Earth's Early Biosphere and its Environment. *Origins*, C. E. Woodward, J. M. Shull, and H. A. Thronson, Jr., Eds., Astronomical Society of the Pacific Conference Series, Vol. 148, 415.

Des Marais, D. J., et al., 2002: Remote Sensing of Planetary Properties and Biosignatures on Extrasolar Terrestrial Planets. *Astrobiology*, **2**, 153–181.

Domagal-Goldman, S. D., V. S. Meadows, M. W. Claire, and J. F. Kasting, 2011: Using Biogenic Sulfur Gases as Remotely Detectable Biosignatures on Anoxic Planets. *Astrobiology*, **11**, 419–441.

Ehrenreich, D., G. Tinetti, A. Lecavelier Des Etangs, A. Vidal-Madjar, and F. Selsis, 2006: The Transmission Spectrum of Earth-size Transiting Planets. *A&A*, **448**, 379–393.

Endl, M., et al., 2011: Kepler-15b: A Hot Jupiter Enriched in Heavy Elements and the First Kepler Mission Planet Confirmed with the Hobby-Eberly Telescope. *ApJS*, **197**, 13.

Han, C., J. Geng, Y. Hong, R. Zhang, X. Gu, X. Wang, S. Gao, and D. Glindemann, 2011: Free Atmospheric Phosphine Concentrations and Fluxes in Different Wetland Ecosystems, China. *Environmental Pollution*, **159**, 630–635.

Hu, R., S. Seager, and W. Bains, 2012: Photochemistry in Terrestrial Exoplanet Atmospheres II: H_2S and SO_2 Photochemistry in Anoxic Atmospheres. *submitted*.

Kaltenegger, L., M. Fridlund, and J. Kasting, 2002: Review on Habitability and Biomarkers. *Earth-like Planets and Moons*, B. H. Foing and B. Battrick, Eds., ESA Special Publication, Vol. 514, 277–282.

Kaltenegger, L. and D. Sasselov, 2010: Detecting Planetary Geochemical Cycles on Exoplanets: Atmospheric Signatures and the Case of SO_2. *ApJ*, **708**, 1162–1167.

Kaltenegger, L. and W. A. Traub, 2009: Transits of Earth-like Planets. *ApJ*, **698**, 519–527.

Kaltenegger, L., W. A. Traub, and K. W. Jucks, 2007: Spectral Evolution of an Earth-like Planet. *ApJ*, **658**, 598–616.

Kashefi, K. and D. Lovley, 2003: Extending the Upper Temperature Limit for Life. *Science*, **301**, 934.

Kasting, J. F., 2001: The Rise of Atmospheric Oxygen. *Science*, **293**, 819–820.

Léger, A., M. Ollivier, K. Altwegg, and N. J. Woolf, 1999: Is the Presence of H_2O and O_3 in an Exoplanet a Reliable Signature of a Biological Activity? *A&A*, **341**, 304–311.

Liou, K. N., 2002: *An Introduction to Atmospheric Radiation*. 2d ed., Academic Press, San Diego, Ca, 583 pp.

Lovelock, J. E., 1965: A Physical Basis for Life Detection Experiments. *Nature*, **207**, 568–570.

Madhusudhan, N. and S. Seager, 2009: A Temperature and Abundance Retrieval Method for Exoplanet Atmospheres. *ApJ*, **707**, 24–39.

Mayor, M. and D. Queloz, 1995: A Jupiter-mass Companion to a Solar-type Star. *Nature*, **378**, 355–359.

Mojzsis, S. J., G. Arrhenius, K. D. McKeegan, T. M. Harrison, A. P. Nutman, and C. R. L. Friend, 1996: Evidence for life on Earth before 3,800 million years ago. *Nature*, **384**, 55–59.

NOAA, NASA, & USAF, 1976: *U.S. Standard Atmosphere, 1976*. U.S. Government Printing Office, Washington, D.C., 227 pp.

Pilcher, C. B., 2003: Biosignatures of Early Earths. *Astrobiology*, **3**, 471–486.

Rauer, H., et al., 2011: Potential Biosignatures in Super-Earth Atmospheres. I. Spectral Appearance of Super-Earths around M Dwarfs. *A&A*, **529**, A8.

Redfield, S., M. Endl, W. D. Cochran, and L. Koesterke, 2008: Sodium Absorption from the Exoplanetary Atmosphere of HD 189733b Detected in the Optical Transmission Spectrum. *APJL*, **673**, L87–L90.

Rothman, L. S., et al., 1998: The HITRAN Molecular Spectroscopic Database and HAWKS (HITRAN Atmospheric Workstation): 1996 Edition. *JQSRT*, **60**, 665–710.

Rothman, L. S., et al., 2009: The *HITRAN* 2008 Molecular Spectroscopic Database. *JQSRT*, **110**, 533–572.

Rothschild, L. J. and R. L. Mancinelli, 2001: Life in extreme environments. *Nature*, **409**, 1092–1101.

Schidlowski, M., 1988: A 3,800-million-year isotopic record of life from carbon in sedimentary rocks. *Nature*, **333**, 313–318.

Schindler, T. L. and J. F. Kasting, 2000: Synthetic Spectra of Simulated Terrestrial Atmospheres Containing Possible Biomarker Gases. *Icarus*, **145**, 262–271.

Schneider, J., 1994: On the Search for O_2 in Extrasolar Planets. *Ap&SS*, **212**, 321–325.

Schopf, J. W., 1999: *Cradle of Life: The Discovery of Earth's Earliest Fossils*. Princeton University Press, Princeton, NJ, 367 pp.

Schopf, J. W. and M. R. Walter, 1983: *Archean Microfossils: New Evidence of Anceint Microbes*. In *Earth's Earliest Biosphere: Its Origin and Evolution*, edited by J.W. Schopf, Priceton University Press, Princeton, NJ, 214-239 pp.

Seager, S., 2010: *Exoplanet Atmospheres: Physical Processes*. 1st ed., Priceton University Press, Princeton, NJ, 243 pp.

Seager, S. and D. Deming, 2010: Exoplanet Atmospheres. *ARA&A*, **48**, 631–672.

Seager, S., M. Schrenk, and W. Bains, 2012: An Astrophysical View of Earth-Based Metabolic Biosignature Gases. *Astrobiology*, **12**, 61–82.

Segura, A., J. F. Kasting, V. Meadows, M. Cohen, J. Scalo, D. Crisp, R. A. H. Butler, and G. Tinetti, 2005: Biosignatures from Earth-Like Planets Around M Dwarfs. *Astrobiology*, **5**, 706–725.

Segura, A., K. Krelove, J. F. Kasting, D. Sommerlatt, V. Meadows, D. Crisp, M. Cohen, and E. Mlawer, 2003: Ozone Concentrations and Ultraviolet Fluxes on Earth-Like Planets Around Other Stars. *Astrobiology*, **3**, 689–708.

Seinfeld, J. H. and S. N. Pandis, 2006: *Atmospheric Chemistry and Physics - From Air Pollution to Climate Change*. 2d ed., John Wiley and Sons, New Jersey, 1225 pp.

Sharpe, S. W., T. J. Johnson, R. L. Sams, P. M. Chu, G. C. Rhoderick, and P. A. Johnson, 2004: Gas-Phase Databases for Quantitative Infrared Spectroscopy. *Applied Spectroscopy*, **58**, 1452–1461.

Swain, M. R., G. Vasisht, and G. Tinetti, 2008: The presence of methane in the atmosphere of an extrasolar planet. *Nature*, **452**, 329–331.

Vidal-Madjar, A., et al., 2004: Detection of Oxygen and Carbon in the Hydrodynamically Escaping Atmosphere of the Extrasolar Planet HD 209458b. *APJL*, **604**, L69–L72.

Webb, J. K. and I. Wormleaton, 2001: Could We Detect O_2 in the Atmosphere of a Transiting Extra-solar Earth-like Planet? *Publ. Astron. Soc. Aust.*, **18**, 252–258.